Topotactic synthesis and characterization of new Kitaev iridates

Dissertation

zur Erlangung des akademischen Grades

Dr. rer. nat.

eingereicht an der

Mathematisch-Naturwissenschaftlich-Technischen Fakultät

der Universität Augsburg

von

Aleksandr O. Zubtsovskii

Augsburg, April 2022

Erstgutachter: Prof. Dr. Alexander Tsirlin
Felix-Bloch-Institut für Festkörperphysik,
Universität Leipzig
Zweitgutachter: Priv.-Doz. Dr. Norbert Büttgen
Lehrstuhl Experimentalphysik V, Universität Augsburg

Tag der mündlichen Prüfung: 23.06.2022

Acknowledgements

I would like to begin by acknowledging the great support and help from my supervisor Prof. Dr. Alexander Tsirlin. His patience, attention to detail and positive attitude gave me strength throughout the entire period of work on my dissertation. I would like to thank him for making this project feasible with his support as well as for organizing many fruitful collaborations and experiments. I would also like to acknowledge the head of our chair Prof. Dr. Philipp Gegenwart for the opportunity to complete this project in a fairly short time. I especially want to thank my previous supervisor Dr. Valeriy Yu. Verchenko for the idea of postgraduate study abroad at the University of Augsburg. I just wouldn't be here without him.

I would like to thank all my collaborators, without whom the project would not have been completed. Their help and support in conducting experiments, primary data analysis and useful discussion have increased my understanding and knowledge in the field of solid state physics, especially in the field of magnetism. In this context, I would like to specially thanks Dr. Anton Jesche for his introduction to the measurement of magnetic properties, Dr. Maria A. Kirsanova and Prof. Dr. Artem M. Abakumov for their help with electron microscopy. I would also like to thank Dr. Chennan Wang, Dr. Mayukh Majumder and Dr. Mark Telling for the help in conducting muon experiments and, in general, for introducing me to such an amazing research method as μSR. I would also like to thank Dr. Gaston Garbarino, Dr. Konstantin Glazyrin, Dr. Ece Uykur and Dr. Bin Shen for their help with the pressure experiments. Without their help and support, there would be no corresponding chapter of my dissertation.

I am very much thankful to my friends and colleagues of the Experimentalphysik VI. I will always remember our joyful Christmas parties, joint conferences and trips to Hirschegg (these long and quiet walks in the mountains). I would like to convey my best wishes and good luck to some of the doctoral students present in our group, Vera Bader, Franziska Grußler, Franziska Breitner, Maximilian Uhl, Noah Winterhalter-Stocker. I thank my office mate Ina-Marie Pietsch for all the nice discussions we had during the writing of our dissertations.

At the end I would like to thank those few persons without whom I simply would not have finished my work. I am grateful to my parents for their emotional support who are so far away from here, to my mother-in-law for her trips to us, thanks to which there was more free time to complete the work, and to my wife and son, who endured my departures for work, waited and believed in me. I am immensely happy that I have you. Without you, I would have no goals in life.

Contents

Chapter 1

Introduction

Quantum phenomena hold a strong promise for new innovative technologies. Experimental realization of these phenomena in solid-state materials is particularly important for eventual practical applications. A special place among the class of inorganic materials is taken by transition metal oxides (TMO) providing a rich variety of physical phenomena. The interplay between Coulomb correlations, bandwidth and spin-orbit coupling (SOC) gives rise to some extraordinary electronic and magnetic properties such as high-temperature superconductivity, charge density waves, magnetic skyrmions and frustrated magnetism. The latter one found for the antiferromagnetic Mott insulators is of particular interest as it can lead to a new unusual state known as a quantum spin liquid (QSL) [1]. The allure of frustrated spin systems is that they may develop not a magnetically ordered ground state as in conventional magnets, but a paramagnetic-like state down to 0 K, where spins continually fluctuate.

Originally proposed for the triangular antiferromagnets [2] in which the source of magnetic moments was 3*d*-transition metals, the idea of magnetic frustration and experimental realization of QSL was transposed onto other frustrated lattices such as Kagomé or pyrochlore ones. However, the heavy 4*d*- and 5*d*-TMO with a strong effect of SOC have been out of sight of the fast-developing spin-liquid physics until the moment when A. Kitaev formulated the model, now commonly known as the *Kitaev model*, on the hexagonal (honeycomb) lattice with a QSL ground state and fractionalized Majorana-like excitations [3]. Further development of the Kitaev model by G. Jackeli and G. Khaliullin [4, 5] for real materials outlined the compound families that are most promising new QSL-candidates. Thus, the honeycomb layered iridates Na_2IrO_3 and α-Li_2IrO_3 were recognized as promising Kitaev spin-liquid materials [6].

Unfortunately, the comprehensive study of sodium and lithium iridates has shown that these compounds develop long-range magnetic order and deviate from scenario of Kitaev spin liquid. This problem identifies the need for isoelectronic iridates with the honeycomb geometry or with other tricoordinated lattices of Ir^{4+}. However, only a handful of such compounds is known from the literature. Beyond Na_2IrO_3 and α-Li_2IrO_3, they include two other polymorphs of Li_2IrO_3 only. Attempts of partial chemical substitutions, as in $(Li,Na)_2IrO_3$, were only partially successful, given the large miscibility range of the corresponding solid solution. All of this calls for new chemical strategies that may stabilize hitherto unknown metastable iridates with the

honeycomb or honeycomb-like geometry of Ir^{4+}. One important prerequisite of such compounds should be the absence of structural disorder, because randomness of exchange interactions can also suppress magnetic order, similar to the frustration, yet without creating the desired QSL ground state.

To this end, we implement the technique of topotactic chemical reactions that entail the ion exchange performed under mild heating and result in completely new chemical compounds that preserve the structural network of their precursor. To avoid structural disorder, we concentrate on β-Li_2IrO_3, which is widely available in both polycrystalline and single-crystalline form without any appreciable structural defects. The focus of this thesis is on three compounds prepared for the first time, their structural and magnetic characterization.

Chapter 2

Frustrated magnetism: theory and material realizations

2.1 Magnetism in solid state physics

All substances in the world are somehow related to magnetism. Their magnetic properties vary in many different ways, with manifestations ranging from ordinary diamagnetic or paramagnetic behavior to extraordinary phenomena such as magnetic skyrmions or quantum spin liquid. All these ordinary or complex properties arise due to specific magnetic interactions of electrons in a compound. It is also necessary to take into account the effect of chemical surrounding of magnetic atoms and crystal structure of a particular compound. External conditions, *e.g.* applied electric or magnetic fields, temperature or external pressure, could also contribute to the revealed properties.

One might say that the most common magnetic properties of materials are caused by atoms with magnetic moments and interactions between them. Therefore, it would be useful first to briefly describe the origin of magnetism, general classification of materials according their magnetic properties and main types of interactions between magnetic atoms. The theory part of this section was prepared based on classical textbooks on magnetism in condensed matter [7–9].

2.1.1 The origin of magnetism and its manifestation in real materials

In insulators, magnetic properties are associated with the presence of atoms or ions possessing a non-zero magnetic moment that depends on electronic configuration of these atoms or ions. In turn, two main parameters describe the magnetic moment of the atom: spin and orbital angular momentum. Their sum presents the total angular momentum $\mathbf{J}$ of an atom: $\mathbf{J} = \mathbf{S} + \mathbf{L}$. Thereby, a cooperative interaction between electron spins and orbital moments in a material (at the quantum mechanical level) creates the macroscopic property of a matter – magnetization M, the magnetic moment per unit volume.

For simplicity, one can assume linearity between magnetization M of a solid and magnetic field H: $M = \chi H$, where χ is magnetic susceptibility (dimensionless), but usually re-calculated in terms of the molar or mass magnetic susceptibility. For given relation, the definition of M means that χ represents the magnetic moment induced by a magnetic field H per unit volume. Temperature dependence of magnetic susceptibility and field dependence of magnetization allow the classification of solids in terms of their magnetic properties (Fig. 2.1). Traditionally, the following types of magnetism are distinguished: diamagnetism, paramagnetism, ferromagnetism and antiferromagnetism. The specifics for each type of contribution will be summarized below.

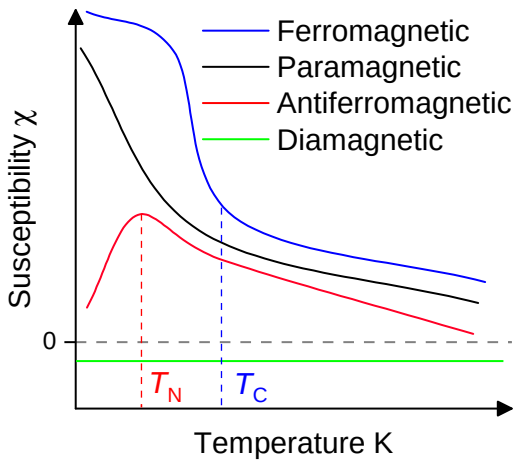

Figure 2.1: Schematic illustration of the magnetic susceptibility as a function of temperature $\chi(T)$ for different types of solids.

Diamagnetism. According to the classical definition, the substance is said to be diamagnetic, when it moves out of the applied field. In other words, for a diamagnetic substance, a magnetic field induces a magnetization, which opposes the applied magnetic field that caused it. The diamagnetic susceptibilities are negative, small, independent of temperature and field strength. The molar susceptibility of a diamagnetic material is usually of the order of $-(1 \div 100) \cdot 10^{-6}$ emu/mol. Diamagnetism is a property of all matter. One can explain this effect from classical mechanics as the action of a magnetic field on the orbital motion of an electron creates a back electromagnetic force, which opposes the magnetic field that causes it. However, the quantum mechanical approach is the only correct one and based on the first-order perturbation theory dealing with a shift in the ground state energy. The diamagnetic susceptibilities of atoms are additive values, and the diamagnetic contribution can be calculated with Pascal's constants, considering the diamagnetic component of atoms, ions, molecules and bonds for a particular case. As noted above, the diamagnetic contribution is very small and can be ignored in the vast majority of cases.

For instance, the compounds, studied in the current work feature core diamagnetic susceptibility of about -7.5×10^{-5} emu/mol, with the largest contribution coming from the Ir^{4+} ions (Pascal constant $= -2.9 \times 10^{-5}$ emu/mol [10]). These diamagnetic susceptibilities are much smaller than the paramagnetic ones and can be safely neglected in the analysis.

Paramagnetism. Paramagnetism is usually a property of substances containing unpaired electrons. In contrast to diamagnetism, paramagnetism corresponds to a positive susceptibility, so that an applied magnetic field induces a magnetization, which aligns parallel with the applied magnetic field that caused it. A paramagnetic susceptibility is generally independent of the field strength (in fact, this is not always exactly true) and temperature-dependent. In the high-temperature approximation, the magnetic susceptibility varies inversely with temperature, which is known as Curie's Law:

$$\chi = \frac{N_A \mu_{eff}^2}{3 k_B T} = \frac{C}{T}, \tag{2.1}$$

where C is the Curie constant, N_A and k_B are the Avogadro and Boltzmann constants, respectively. This expression becomes very useful in cases of determination of the effective magnetic moment for a particular substance. Here are several compounds that follow the Curie's Law: $KCr(SO_4)_2 \cdot 12\,H_2O$, $(NH_4)_2Mn(SO_4)_2 \cdot 6\,H_2O$ and $Gd_2(SO_4)_3 \cdot 8\,H_2O$. However, not so many compounds show strictly paramagnetic behavior of magnetic susceptibility because of the residual interactions between magnetic atoms or ions in a sold.

Ferromagnetism. A substance is called a ferromagnet, when it has a spontaneous magnetization in the absence of an applied field. A spontaneous magnetization occurs due to a certain orientation of the magnetic moments or due to lying in a single unique direction. According to the Weiss model of ferromagnetism, at low temperature, the moments can be aligned by the internal molecular field and the magnetic order is self-sustaining. As the temperature increases, thermal fluctuations prevail over the magnetic order and at the special temperature, the system has a transition from a ferromagnetic state to a paramagnetic state. The transition temperature is known as the Curie temperature T_c. The magnetic susceptibility of a ferromagnet above the critical temperature ($T > T_c$) obeys the Curie-Weiss law: $\chi = \frac{C}{T - \theta}$, where θ in this case equals the Curie temperature T_c. The behavior of magnetic susceptibility of a ferromagnet below T_c requires complex analysis and cannot be described by Weiss model.

Antiferromagnetism. An antiferromagnet can be represented as a system of two or more interpenetrating magnetic sublattices: magnetic moments on each sublattice have the same direction, but relative to the other sublattice magnetic moments point in the opposite direction. The nature of the interaction between magnetic moments is such that it is favorable for nearest neighbor magnetic moments to lie antiparallel to one another. The Weiss model is applicable for antiferromagnetism as for ferromagnetism, and the system has a transition from some ordered state to the paramagnetic one. The temperature of transition is known as the Néel temperature T_N. The magnetic susceptibility of an antiferromagnet in the paramagnetic regime ($T > T_N$)

obeys the Curie Weiss law as well: $\chi = \frac{C}{(T-\theta)}$, where θ in this case is the Weiss temperature and corresponds to be negative. However, experimentally determined Weiss temperatures do not match the Néel temperature. The number of types of antiferromagnetic order is quite large because there are many ways to arrange spins antiparallel to each other on the sublattices in a different manner.

2.1.2 Magnetic interactions

The existence of ordered magnetic states, *e.g.* ferromagnetism or antiferromagnetism, is impossible without the presence of magnetic interactions between the magnetic moments of a solid. Moreover, exchange interactions are the main reason of long-range magnetic order (LRMO) or more complex behavior. In principle, one can mention the magnetic dipolar interactions as an additional contribution. But because of the small value of the interaction energy (about 1 K), this effect can be neglected with magnetic order in most materials. Also such exchange interactions as **double exchange** (typical for the systems containing magnetic ions with mixed oxidation states) and **RKKY interactions** (indirect exchange interaction in metals) will not considered here due to thier absence in the studied materials. In this way, a short review of exchange interactions directly related to the Kitaev iridates is the topic of this section.

Direct exchange. Exchange interactions are electrostatic interactions and first, it's necessary to determine how to evaluate the interaction between magnetic moments. The starting point is the problem of a two-electron system. Applying the quantum mechanical approach for this problem, one gets two possible states: singlet state and triplet state. The difference between two states can be parameterized using $\mathbf{S_1} \cdot \mathbf{S_2}$. The Hamiltonian can be written in the form of an effective Hamiltonian:

$$\hat{\mathcal{H}} = \frac{1}{4}(E_S + 3E_T) - (E_S - E_T)\mathbf{S_1} \cdot \mathbf{S_2}$$

Defining the exchange constant as $J = (E_S - E_T)/2$, and shifting the beginning of energy level, the spin-dependent term in the effective Hamiltonian has the following form:

$$\hat{\mathcal{H}}^{spin} = -2J\mathbf{S_1} \cdot \mathbf{S_2}$$

For a many-body system, the spin Hamiltonian can be rewritten in the form of the Heisenberg model:

$$\hat{\mathcal{H}}^{spin} = -\sum_{ij} J_{ij}\mathbf{S}_i \cdot \mathbf{S}_j \tag{2.2}$$

where J_{ij} is the exchange constant between the i^{th} and j^{th} spins. When J is positive ($J > 0$), it refers to triplet state and ferromagnetic interactions.

When J is negative ($J < 0$), it refers to singlet state and antiferromagnetic interactions.

However, depending on the parameterization conditions, the final form of the spin Hamiltonian may differ. Thus, in the Kitaev model that will be presented later, the constant J describes the exchange interaction per bond between $\mathbf{S}_i$ and $\mathbf{S}_j$ spins, and the positive value ($J > 0$) means an antifferomagnetic type of the interaction. In this case, the spin Hamiltonian used for the Kitaev model can be rewritten as

$$\hat{\mathcal{H}}^{\text{spin}} = \sum_{ij} J_{ij} \mathbf{S}_i \cdot \mathbf{S}_j. \tag{2.3}$$

The nearest-neighbor Heisenberg model is the most common model of interacting spins. Direct exchange is an exchange interaction between electrons on neighboring magnetic atoms without any influence of intermediary. Practically, direct exchange never plays significant role in controlling magnetic properties due to the low probability of overlapping orbitals of neighboring atoms. Therefore, indirect exchange interactions must be taken into account.

Superexchange. Superexchange is a type of indirect exchange interactions between non-neighboring magnetic ions which separated by a non-magnetic ion. Superexchange arises from the kinetic energy advantage of antiferromagnetic coupling between electrons of magnetic and non-magnetic ions. The origin of superexchange is the second-order perturbation theory; the exchange constant J is proportional to $-t^2/U$, where t is the hopping integral and U is the energy cost of making an excited state. In addition, superexchange is strongly dependent upon the angel between magnetic and non-magnetic ions (the degree of orbital overlap), and in most cases is presented in antiferromagnetic systems.

Anisotropic exchange interaction. The spin-orbit coupling of one magnetic ion produces the excited state which then interacts with the ground state of another magnetic ion. This is known as the anisotropic exchange interaction or as the Dzyaloshinsky-Moriya interaction (DMI) and plays significant role by describing magnetic properties of more complex systems. This type of exchange can be described by additional term in the Hamiltonian:

$$\hat{\mathcal{H}}_{\text{DM}} = \mathbf{D} \cdot \mathbf{S_1} \times \mathbf{S_2} \tag{2.4}$$

The DMI usually arises in systems lacking inversion symmetry. The combination of low symmetry and spin-orbit coupling gives rise to the finite antisymmetric exchange interaction. Therefore, this term should also be include in the general description of the exchange interactions.

The general Hamiltonian describing the interactions between such local moments can be expressed as follows:

$$\mathcal{H} = \sum_{ij} J_{ij} \mathbf{S}_i \cdot \mathbf{S}_j + \mathbf{D}_{ij} \cdot (\mathbf{S}_i \times \mathbf{S}_j) + \mathbf{S}_i \cdot \mathbf{\Gamma}_{ij} \cdot \mathbf{S}_j \tag{2.5}$$

where J_{ij} is the isotropic Heisenberg coupling, $\mathbf{D}_{ij}$ term is responsible for the anisotropic Dzyaloshinskii–Moriya interaction, and $\mathbf{\Gamma}_{ij}$ is the symmetric pseudo-dipolar tensor. The main contribution to the anisotropic exchange interactions is associated with the effect of spin-orbit coupling, which is strong in the case of heavy transition metals, particularly, for the family of Ir-based compounds with Ir^{4+} magnetic ion.

2.2 Frustrated magnetism and spin liquid

Ferromagnetic and antiferromagnetic orders are the most common ways to arrange spins in magnetic systems showing long-range magnetic order. There are also ferrimagnetic and helical types of spin ordering that could also be described by the magnetic interactions mentioned above. However, there may be a situation when spins in some magnetic systems exhibit *frustration* due to competing exchange interactions and impossibility to simultaneously satisfy these intersections. The origin of why one systems show long-range magnetic order and others prone to frustrated magnetism lies in the nature of the involved magnetic moments.

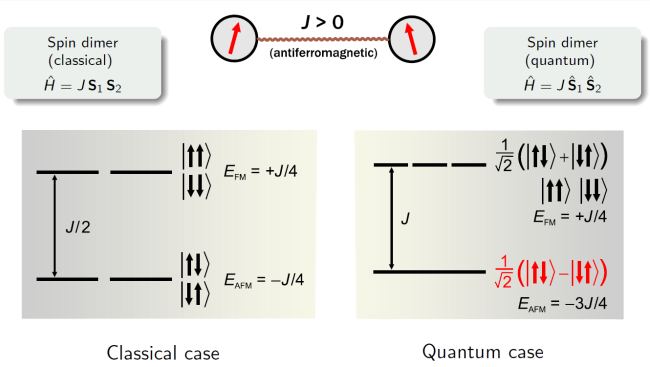

Figure 2.2: Comparison of classical and quantum approach on the example of a spin dimer [11].

Classical and quantum magnets. In classical magnets, a magnetic order is defined by the unique lowest energy spin configuration with an unambiguously ground state. Usually, the spins in such systems are large ($S > 1$) driven by ferromagnetic interactions. In the ordered state, elementary excitations are known as spin waves (magnons) with an integer spin number. Magnons can be represented as a consequence of spin precession in the ordered state.

In quantum magnets, the spins are small ($S = \frac{1}{2}$) dominated by antiferromagnetic interactions (Fig. 2.2). The strong interacting spins can be represented with a large number of spin configurations simultaneously with the

same energy without leading to a certain ordered state. Such frustrated magnets do not show any long-range magnetic order, and dynamic of spins survives down to zero temperature.

Indeed, the peculiar state known as *spin liquid* may emerge in the frustrated spin systems. This specific type of matter represents the ensemble of fluctuating spins which preserve spin dynamics down to low temperatures. Two types of spin liquids can be distinguished: classical spin liquid where frustration is achieved by mixing of different magnetic orders; and quantum spin liquid (QSL) where spins are quantum-mechanically entangled. Both states are of interest in the sense of frustrated magnetism. Nevertheless, a search of real-world materials showing a QSL behavior is a little bit more tricky and exciting process (as part of this work).

Now, it is worth highlighting the origins of a spin liquid state. There are two main concepts for frustrated systems where this phenomena could be observed: the first one is a geometrical frustration based on a competition between nearest-neighbors spins on triangular-like loops, and the second one is an exchange frustration controlled by competing magnetic anisotropies. Further, both geometrical and exchange frustration concepts are briefly described from the theory point of view.

2.2.1 Geometrical frustration

Triangular-like lattice. The main idea of geometrical frustration is an arrangement of spins on the lattice consisting of triangular sections. Figure 2.3 represents the most common types of lattices: triangular, Kagomé and pyrochlore. To better understand the principle of geometrical frustration, it is reasonable to consider the situation, when antiferromagnetically interacting Ising spins are located at the corners of a triangle (Fig. 2.3d). On the one hand, all spins have to be pointed up or down due to antiferomagnetic interactions between them. On the other hand, they cannot align antiparallel to each other (from the geometrical point of view). This triggers an uncertainty in the direction of one of the three spins and causes a degeneracy of the ground state. Transposing such approach to 2D and 3D lattices mentioned above, frustration or fluctuation of spins may occur and the transition to ordered state might be suppressed. However, the presence of triangular-like lattice of spins doesn't lead to a QSL state. Different types of long-range magnetic order could arise even on frustrated lattice: 120° or stripe orders on the triangular lattice, $\sqrt{3} \times \sqrt{3}$ order on the Kagomé lattice or "two-in-two-out" order on the pyrochlore lattice (so-called spin-ice rule).

The next essential ingredient is the size of a magnetic moment. The behavior of large spins (greater then $S = 1$) becomes more classical that means a tendency to undergo a magnetic transition to the ordered state or freezing of spins instead of fluctuating at low temperatures. Therefore, the systems containing spin-$\frac{1}{2}$ ions on a proper lattice have a better chance to reach a QSL state. Due to a quantum nature of such a small spin, another crucial property emerges – the long-range entanglement. Thus, all spins are controlled by quantum fluctuations. Particularly on a triangular lattice, the entangled

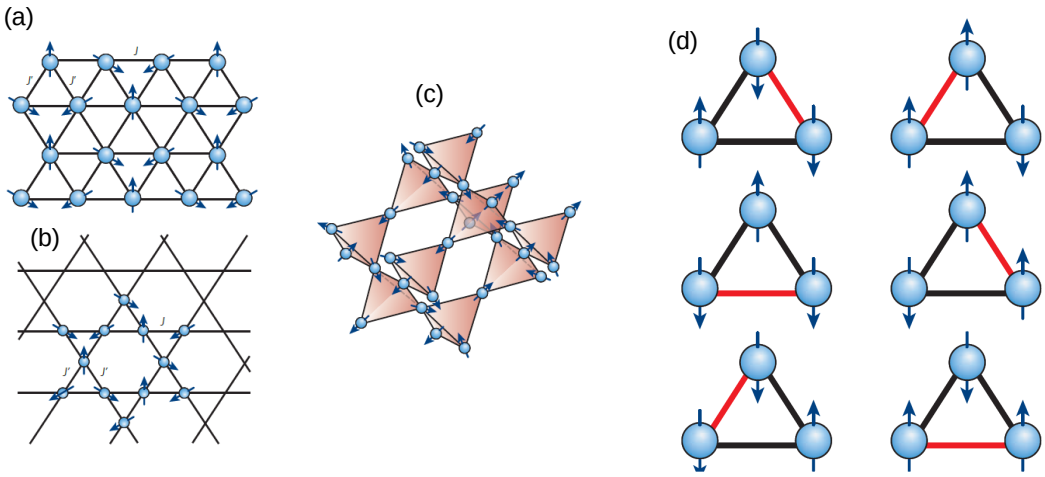

Figure 2.3: Common types of lattices demonstrating geometrical frustration: (a) triangular, (b) Kagomé and (c) pyrochlore. (d) Visualization of the geometrical frustration on a triangle of antiferromagnetically interacting Ising spins. The uncertainty in the spin direction triggers frustration [1].

spins may form a resonating-valence-bond (RVB) state which is connected to the QSL state and was firstly proposed by Anderson in 1973 [2].

Resonating valence bond theory. The valence bond is a pair of spins coupled antiferromagnetically that forms a spin-0 singlet state. If all spins in the system are split into valence bonds and the entanglement occurs only between spins in the individual pair, the valence bonds become static and localized. The absence of the resonance effect between valence bonds leads to a new type of a ground state known as a valence-bond solid (VBS) state. However, VBS state does not represent quantum spin liquid: it suggests some sort of symmetry breaking (due to a specific arrangement of valence bonds on the lattice) and shows only short-range entanglement in a particular singlet pair.

Another situation may be considered, when the valence bonds can undergo quantum mechanical fluctuations. In this case, the new ground state – resonating-valence-bond (RVB) state – emerges as a superposition of different VBS states. It is now no preferences in forming a particular spin pair and any configurations of valence bonds are allowed. Breaking a valence bond leads to an excitations that splits (fractionalizes) into two unpaired spins (spinons) that independently propagate trough the lattice (Fig. 2.4) introducing frustration. Such fractionalized excitations give a possibility of realization of QSL states in the material.

There is an extensive range of materials possessing frustrating magnetism on triangular-like lattices covering 2D and 3D crystal structures. The class of compounds with geometrical frustration includes metal–organic framework (MOF) magnets, coordination compounds, complex oxides, chalcogenides, chlorides, and etc. The source of magnetic moments in these materials can be $3d$, $4d$ or $5d$ transition metals as well as f-electron systems. Some of the

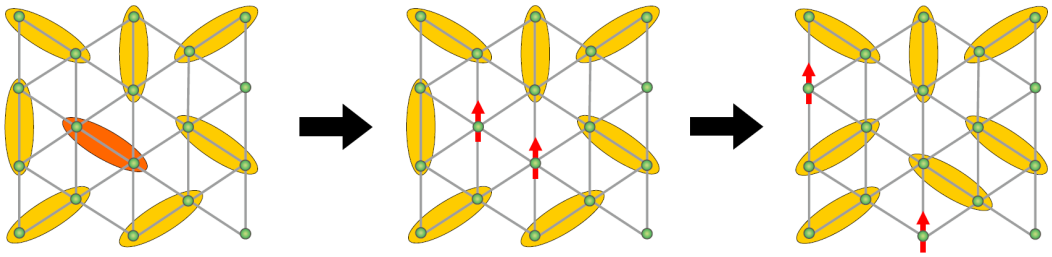

Figure 2.4: Formation of the spinon excitation in the nearest-neighbor RVB state of triangular antiferromagnets by breaking one of the valence bonds. Two unpaired spins (red arrows) can propagate independently and constitute spin-$\frac{1}{2}$ (spinon) excitations [12].

materials with frustrated magnetism or even as the QSL candidates deserve more attention and will be presented later in the corresponding section.

2.2.2 Exchange frustration.

Exchange frustration, in contrast to the geometrical one, occurs not because of the uncertainty in spins directions coupled antiferromagneticaly but due to the different anisotropic exchange interactions between neighboring spins and, therefore, impossibility to minimize the energy at the same time. For instance, one can consider a system of four Ising spins arranged as in Fig. 2.5a. Side spins have different, mutually orthogonal quantization axes. The central spin would couple with its neighboring spins and be parallel pairwise, but due to uncertainty in its own quantization axis, an exchange frustration arises. One of the best-known models of exchange frustration is the Kitaev model on the hexagonal (honeycomb) lattice.

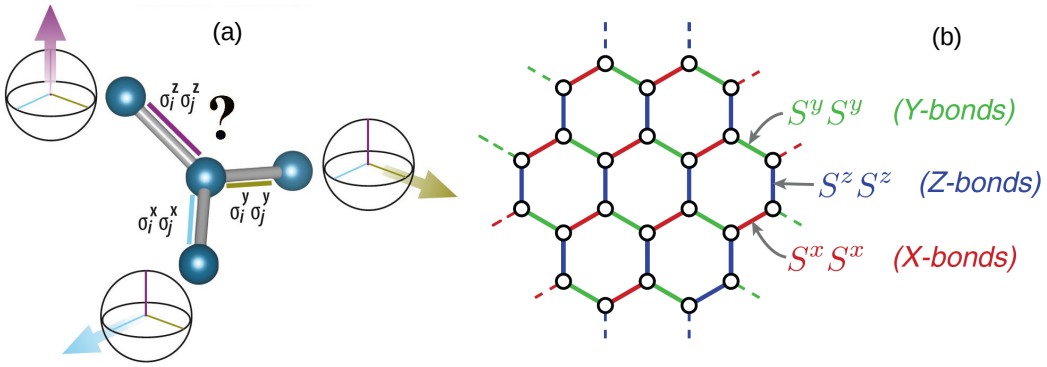

Figure 2.5: (a) Visualization of the exchange frustration [13]. (b) Representation of the Kitaev model on the honeycomb lattice [14] with the corresponding XYZ-bond notation.

The Kitaev honeycomb model. The Kitaev model proposed by Alexei Kitaev in 2006 [3] describes a system of spins with $S = 1/2$ located on the hexagonal (honeycomb) lattice (Fig. 2.5b). The main features of this model are (i) it has an exact solution, and (ii) it offers a possibility of the quantum spin liquid ground state. The model considers anisotropic spin-spin interactions along each bond including only nearest-neighbor interactions, and takes into account the orientation of these bonds. From the geometrical nature of the honeycomb lattice, there are three types of bonds which bear orthogonal Ising interactions:

$$\mathcal{H} = K \sum_{\langle ij \rangle} S_i^{\gamma} S_j^{\gamma},$$

where K is the Kitaev coupling constant as a measure of the Kitaev interaction that refers only to ferromagnetic contribution, and $\gamma = \{x, y, z\}$ representing the direction for each type of the bonds. According to a standard notation for the Kitaev model, these bonds are labelled as X-, Y- and Z-bonds, respectively. The elementary excitations in this case separate into Majorana fermions and fluxes.

The exact solution of the Kitaev model and possibility to be extended to any 3D structures provide a great platform for searching of the QSL state in real materials. However, the practical realization of the model requires certain conditions which have been formulated by Jackeli and Khaliullin for a narrow class of $4d$- and $5d$-electron Mott insulators. These conditions were later extended to some of the $3d$- and $4f$-compounds.

The Jackeli–Khaliullin mechanism. The mechanism proposed by Jackeli and Khaliullin in 2009 [4, 15] determines essential elements for realizing the Kitaev-type interactions in real materials. The first one is an existence of spin-orbit coupled ions with the effective angular momentum $j_{\text{eff}} = \frac{1}{2}$ under the strong effect of the crystal field. The second one is suppression of the Heisenberg interactions by the exchange processes between magnetic ions through the orbitals of shared ligands. The best manifestation of both conditions is $4d$ or $5d$ transition metals with d^5 electron configuration in an edge-sharing octahedral environment. The following will briefly describe the reasons why this type of ions satisfies the conditions mentioned above.

The first crucial point is **the origin** of the $j_{\text{eff}} = \frac{1}{2}$ magnetic moment. d-orbitals are split by the octahedral crystal field in such a way that for the d^5 configuration, there are two e_g levels and a triply degenerate t_{2g} state. Since the low-spin d^5 state is considered, all 5 d electrons occupy the t_{2g} levels, where there is one hole left. Further, the t_{2g} states are split by the spin-orbit coupling (SOC) into two new states with total effective angular momentum $j_{\text{eff}} = \frac{1}{2}$ and $j_{\text{eff}} = \frac{3}{2}$ (Fig. 2.6). This happens because the SOC becomes stronger from $3d$ to $5d$ transition metals.

The second point of the mechanism is proper **exchange processes** between magnetic moments. The main contribution to such interactions is a superexchange process via the mediate ligands. However, for the heavy $4d$ and $5d$ elements, an additional direct $d - d$ hopping must be considered for

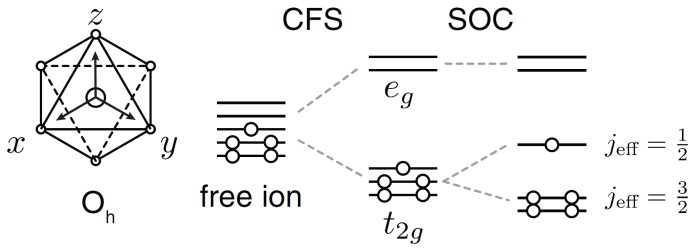

Figure 2.6: Visualization of the crystal field splitting (CFS) and spin-orbit coupling (SOC) effects on the local d-orbital states for the d^5 state in the octahedral environment [14].

the complete description of the exchange processes due to noticeably diffused d-orbitals. For the Z-bond, assuming C_{2h} symmetry, the $d-d$ hopping matrix may generally be written [16]:

	$d_{i,yz}$	$d_{i,xz}$	$d_{i,xy}$
$d_{j,yz}$	t_1	t_2	t_4
$d_{j,xz}$	t_2	t_1	t_4
$d_{j,xy}$	t_4	t_4	t_3

where each t_i represents a certain hopping integral corresponding to the particular exchange process: t_1 and t_3 arise primarily from direct metal-metal interactions (d-d hopping), t_2 is dominated by ligand-assisted exchange (indirect d-p-d hopping), and t_4 comes from the non-ideal octahedral environment of the central d element due to local distortions presented in real materials (mixed hopping process). Figure 2.7 illustrates schematic visualization of main exchange processes:

The resulting magnetic interactions represented in terms of these hopping integrals are:

$$J_{ij} = \frac{4\mathbb{A}}{9}(2t_1 + t_3)^2 - \frac{8\mathbb{B}}{9}\{9t_4^2 + 2(t_1 - t_3)^2\} \tag{2.6}$$

$$K_{ij} = \frac{8\mathbb{B}}{3}\{(t_1 - t_3)^2 + 3t_4^2 - 3t_2^2\} \tag{2.7}$$

$$\Gamma_{ij} = \frac{8\mathbb{B}}{3}\{2t_2(t_1 - t_3) + 3t_4^2\} \tag{2.8}$$

$$\Gamma'_{ij} = \frac{8\mathbb{B}}{3}\{t_4(3t_2 + t_3 - t_1)\} \tag{2.9}$$

for $\mathbb{A} \sim 1/U \gg \mathbb{B} \sim J_H/(3U^2)$, in terms of the local Coulomb repulsion U and Hund's coupling J_H. Combination of these contribution via the Eq. 2.5 gives rise to the following expression:

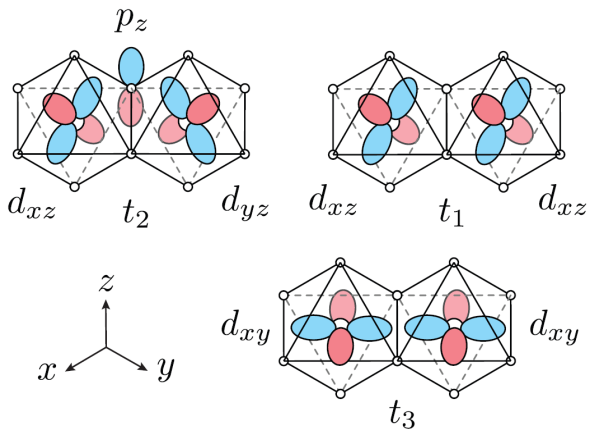

Figure 2.7: Exchange processes for the nearest neighbor hopping interactions in the case of the edge-sharing octahedra (Z-bond) [14]. The hopping integral t_2 represents the indirect d-p-d hopping, while t_1 and t_3 arise mainly from the direct d-d hopping.

$$\mathcal{H}_{ij} = \mathrm{J}_{ij}\mathbf{S}_i \cdot \mathbf{S}_j + K_{ij}S_i^{\gamma}S_j^{\gamma} + \Gamma_{ij}\left(S_i^{\alpha}S_j^{\beta} + S_i^{\beta}S_j^{\alpha}\right) + \Gamma'_{ij}\left(S_i^{\gamma}S_j^{\alpha} + S_i^{\gamma}S_j^{\beta} + S_i^{\alpha}S_j^{\gamma} + S_i^{\beta}S_j^{\gamma}\right) \quad (2.10)$$

where $\{\alpha,\beta,\gamma\} = \{y,z,x\},\{z,x,y\}$ and $\{x,y,z\}$ representing the X-, Y-, and Z-bonds, respectively. Vanishing of the the Dzyaloshinsky-Moriya term $\mathbf{D}\cdot\mathbf{S_1}\times\mathbf{S_2}$ from the Eq. 2.5 is associated by the local octahedral symmetry of the magnetic ions in the Kitaev model. The additional finite terms Γ'_{ij} arise from distortions of the octahedral environment, but they are small compared to J, K and Γ, and can be neglected.

Summarizing the above, the indirect d-p-d and direct d-d hopping processes play a crucial role in an arising of the Kiteav interaction on the one hand, and suppressing the Heisenberg J and off-diagonal Γ interactions on the other hand. An effective way to control hopping on the interactions is to monitor the metal-metal bond distance, or the metal-ligand-metal (M-L-M) bond angle Θ , which modulates the strength of t_1 and t_3 hopping, between pairs of metals in the edge-sharing octahedral environment (in the case of an ideal geometry, the angle $\Theta = 90°$). When $\Theta > 90°$, the distance between transition metals increases and t_1 and t_3 are partly suppressed, leading to dominant ferromagnetic Kitaev interactions ($K < 0$) with large t_2 as proposed in the original Jackeli–Khaliullin mechanism. On the other hand, when $\Theta < 90°$ (large t_1 and t_3) the indirect exchange is not dominant now leading to antiferromagnetic Kitaev term $K > 0$, and other exchange processes become much more pronounced (large $\Gamma > 0$ and $\mathrm{J} > 0$). Figure 2.8 shows a dependence of the different contributions in the exchange processes on metal-ligand-metal (M-L-M) bond angle Θ obtained by perturbation theory [17] and quantum chemistry calculations [18]. Both approaches suggest

the optimal angel $\Theta \sim 100^\circ$ when the Kitaev coupling constant $K < 0$ is dominant. Therefore, the application of the Jackeli–Khaliullin mechanism for real materials should be done with attention to local distortion in a crystal structure, especially to octahedral environment of transition metals.

Alternative mechanisms and extensions. The Jackeli–Khaliullin mechanism is one of the most known and well-studied approach in the context of bond-dependent anisotropic interactions. Offering a direct way to search QSL materials with Kitaev exchange iterations, this mechanism is not the only one, and systems with $4d$ or $5d$ transition metals with d^5 electron configuration are not the only suitable platforms with exchange frustration.

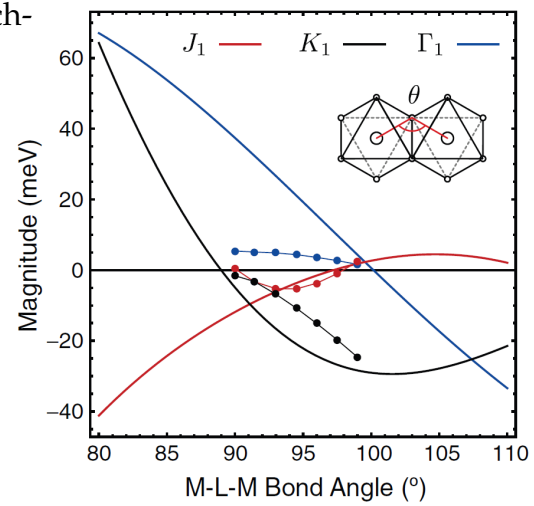

Figure 2.8: Dependence of the nearest neighbour magnetic interactions on the M-L-M bond angle Θ. [14].

As an alternative to heavy $4d$ and $5d$ transition metals, $3d$ and f-electron systems could also bear a sort of **the exchange frustration** (not to be confused with similar systems appealing to geometrical frustration [12]). From the theoretical and practical points of view [19, 20], Co^{2+} and Ni^{3+} with the high-spin d^7 electron configuration as well as Pr^{4+} with the f^1-electron configuration could be promising ions to Kitaev-type interactions on the honeycomb lattice: a series of A_2PrO_3 (where A is an alkali metal) studied by combining *ab initio* calculations and model analysis [21, 22], a vast family of Co^{2+} compounds (for instance, $BaCo_2(AsO_4)_2$ [23], $BaCo_2(PO_4)_2$ [24]) and $NaNi_2BiO_{6-\delta}$ [25] as a case of Ni^{3+}. Despite the presence of ordering (zigzag, helical, noncollinear and etc.) in the mentioned systems, $3d$- and $4f$-metal-based compounds could still be a suitable playground for searching of new frustrated magnets or at least bearing unusual magnetic properties.

2.2.3 Experimental signatures of a QSL

In general, spin liquids itself can be divided into two different classes: a gapped one denoted as Z_2 [26] and a gapless spin liquid denoted as U(1) [27]. Originally, it was proposed for triangular-like systems obeying RVB physics, but such classification is applicable for honeycomb lattice as well. The main differences between spin liquids are the "degree" of valence bonds entanglement and types of excitations. In the case of the Z_2 type, only short-range valence bond are presented, and two kinds of excitation are formed: high-energy spinons and low-energy visons. In a gapless U(1) spin liquid, the formation of valence bonds occur not only between neighboring atoms, but

also between distant ones leading to a mixture of highly entangled short- and long-range valence bonds. But how can one distinguish the spin liquids from the ordered magnets or from other disordered states?

Experimentally, QSL can be identified by following signatures:

1. The simplest indication of unusual magnetic behavior is a large frustration factor $f = |\theta_{CW}|/T_N$, where θ_{CW} is the Curie-Weiss temperature and T_N is the transition temperature. For typical (anti)ferromagnets, θ_{CW} is roughly comparable with the ordering temperature, and a significant deviation of f from 1 may indicate that magnetic order is impeded.

2. In the ideal case, thermodynamic measurements, *e.g.* magnetization and specific heat, reveal the absence of long-range magnetic order or spin freezing.

3. At low temperatures, spin dynamics can be directly probed by nuclear magnetic resonance (NMR) and muon spin relaxation (μSR) experiments. These techniques are very sensitive to local small static fields that allow to distinguish disordered magnetism from spin-liquid behavior.

4. In the magnetically ordered state, deviation of the magnetic specific heat C_m from the T^3 behavior is associated with magnons (spin waves). In the context of spin liquid types, specific-heat measurements give additional information. An exponential behavior of the magnetic specific heat C_m refers to the Z_2 spin liquid, while the linear or sublinear power-law behavior of C_m is expected to the U(1) type.

5. The nature of correlations and excitations in the material may be characterized by inelastic neutron-scattering (INS) measurements. A continuum of fractionalized excitations is expected for QSL. For an ordinary antiferromagnet, the INS spectra show distinguishable branches of magnons.

6. Finally, thermal transport can determine whether these excitations are localized or itinerant by the absence or presence of the finite residual term κ_0/T in the thermal conductivity. Particularly, measuring the thermal Hall conductivity, κ_{xy}^{2D}/T, for 2D systems may indicate the presence of itinerant Majorana fermions and Z_2 fluxes – the signs of the Kitaev QSL state.

This set of different techniques can be extended depending on the subject of the study. To comprehensively characterize a QSL material, the combination of different methods is needed. Moreover, the obtained results should be consistent or at least do not contradict. However, not all of them can be applied for the characterization of QSL candidates. Particularly, in the absence of single-crystalline samples, this list can be narrowed.

The compounds, studied in the current work, could so far be synthesized in polycrystalline form only. However, the following techniques are relevant

in this case. High-resolution x-ray and neutron diffraction measurements along with electron microscopy investigation can be used for the detailed study of the crystal structure, assess the degree of structural disorder and its possible effect on the magnetic properties. Magnetization and specific heat measurements reveal the presence or absence of the long-range magnetic order, indicate paramagnetic-like or spin-glassy behavior, and estimate the critical temperatures of these effects. Finally, μSR experiments as commonly used techniques can shed light on the local magnetism in the studied compounds.

2.3 Examples of real materials with frustrated magnetism

There are plenty of materials proposed as QSL-candidates, many of them were really close to the desirable QSL state. However, after a long comprehensive study, most of them failed to show all properties that are theoretically expected in a QSL. Nevertheless, it's still reasonable to mention several representatives and small classes of QSL-candidates. Here, it will be only a short representation of materials exhibiting magnetic frustration in the view of the types of frustrated lattices. More detailed analysis of the current state of affairs in the field of QSLs can be found in these review articles [1, 12, 28–32]. Additionally, the spin glass (SG) materials will be briefly discussed in this section because of the close relationship to the studied compounds. Even though spin glasses exhibit some sort of spin freezing without clear long-range magnetic order, the spin dynamics may be present in some of these compounds.

2.3.1 Two-dimensional QSL candidates

2D QSL candidates may be the largest class of compounds that tend to frustrated magnetism, including both geometrical and bond-dependent (exchange) frustration. Two-dimensional nature of the magnetic lattice considers mostly the spin interactions in the magnetic layers assuming that the interactions between layers are very weak. Such approach allows to apply simple models to describe the complex magnetic behavior in QSL candidates and search for new ones. This type of materials can be classified by the type of 2D lattice in the nodes of which magnetic ions are located: triangular, Kagomé and honeycomb.

Triangular lattice. There are a variety of compounds possessing this pattern in one form or another. They can be both single compounds and families with a certain type of ion. Notwithstanding the different electronic configurations or origins of the magnetism, all the listed compounds act as an effective spin-$\frac{1}{2}$ suggesting QSL ground state. The most interesting examples of individual materials are organic charge-transfer salts $\mathbf{EtMe_3Sb[Pd(dmit)_2]_2}$

[33, 34] and κ-**(BEDT-TTF)$_2$Cu$_2$(CN)$_3$** [35, 36], which can be both VBS and more QSL-like, and the transition metal dichalcogenide **1*T*-TaS$_2$** with itinerant excitations representing spin liquid state [37]. The next group of materials is a family of the Co^{2+}-based compounds including the perovskite **Ba$_8$CoNb$_6$O$_{24}$** [38, 39] and recently discovered **Na$_2$BaCo(PO$_4$)$_2$** [40–42] as a promising QSL candidate. The $4f$-electron antiferromagnets, in which the Yb^{3+} ion acts as an effective spin-$\frac{1}{2}$, demonstrate frustrated magnetism on the triangular lattice. The most interesting examples are well-studied **YbMgGaO$_4$** [43–45] as realization of a random-singlet state with fractional but not fractionalized excitations, and a relatively new family of Yb^{3+} delafossites with the general formula **AYbCh$_2$**, where A stands for an alkaline metal (from Na to Cs) and Ch is a chalcogen (O, S or Se) [32, 46, 47].

Kagomé lattice. Kagomé lattice is the next type of 2D magnetic pattern related to QSL materials. It can be easily converted from the triangular lattice by removing every second node from the adjacent row in such a way that only corner-sharing triangles are present. Kagomé lattice may be seen as a motif of interconnected Stars of David in the corners of which there are magnetic ions. In contrast to the materials with triangular lattice, the class of Kagomé antiferromagnets is abundant in Cu^{2+} compounds with the most famous representative – Herbertsmithite **ZnCu$_3$(OH)$_6$Cl$_2$** [48–50], as well as other light $3d$ and $4d$ metal-based materials – **LiZn$_2$Mo$_3$O$_8$** [51] and **Ca$_{10}$Cr$_7$O$_{28}$** [52, 53].

Honeycomb lattice. The last group of 2D QSL material candidates is compounds in which magnetic ions are located on the honeycomb lattice. The vast majority of materials prone to frustrated magnetism on the honeycomb lattice contain heavy $4d$ or $5d$ transition metals. One can find examples with another type of ions, for instance Co^{2+} or Pr^{4+}, which were mentioned earlier [22–24]. However, the most promising QSL candidates in this group were found for compounds with Ru^{3+} or Ir^{4+} ions representing Kitaev spin-liquid model and frustrated magnetism. Since the group of materials are directly related to this work, the detailed representation of these compounds as well as their derivatives will be discussed in the independent Section 2.4.

2.3.2 Three-dimensional magnets as QSL candidates

The last group of potential QSL materials behavior is 3D magnetic systems. Unlike the two-dimensional analogues rich in a variety of crystal structures and ways of arrangement of magnetic ions, 3D QSL candidates are mainly represented by several groups of compounds or single examples. For instance, a derivative of the 2D honeycomb lattice is the 3D hyperhoneycomb and stripy-honeycomb ones, the practical realization of which are Ir-based compounds β- and γ-Li_2IrO_3, respectively. Both phases are directly related to the main topic of this work as well and will be discussed in detail later.

Hyperkagomé lattice. The Kagomé lattice can be extended to the three-dimensional case where corner-sharing triangles of magnetic ions are arranged in the complex 3D motif. Several examples with such an arrangement of magnetic ions can be found in real materials. For instance, $\mathbf{Na_4Ir_3O_8}$ bears Ir^{4+} ions ($j_{\text{eff}} = \frac{1}{2}$) on the hyperkagomé lattice giving rise to the QSL physics and realization of the Kitaev frustrated magnetism [54–56]. Cu-based materials also demonstrate a great tendency to the frustrated magnetism on the different types of lattices. Among 3D materials, one can find an antiferromagnet $\mathbf{PbCuTe_2O_6}$ hosting Cu^{2+} ions ($S = 1/2$) on the hyperkagomé lattice [57, 58].

Pyrochlore lattice. Compared to 2D lattices, in which a triangular arrangement of spins act as a building block of geometrical frustration, it's not so easy to find a different analogue in 3D systems. However, if one constructs a regular tetrahedron with magnetic ions (Ising spins) in the corners, the uncertainty in spins orientation can be reached causing frustrated magnetism [1]. Such concept is realized in several systems: (i) compounds with the diamond lattice, *e.g.* $\mathbf{FeSc_2S_4}$ [59, 60], and (ii) pyrochlore lattice.

The latter one is closely related to the concept of the Spin ice (SI). Historically, the SI systems were among the first materials showing frustrated magnetism on the 3D structures [1, 61]. The term *spin ice* is usually applied to the pyrochlores, materials with a general formula $A_2B_2X_7$, where both A and B sites form pyrochlore sublattices, and only one position (A) are occupied by a magnetic ion. The frustration in this compounds can be described by so-called "ice rule" [62]: if two spins on a tetrahedron are pointing out, then the other two spins must point in (also called as "two-in-two-out" rule). The class of pyroclore materials are vast including dozens of oxide compounds [63]. The spin ices with rare-earth ions hold a special place among other pyroclores, for instance, $\mathbf{Ln_2Ti_2O_7}$ (Ln = Dy, Yb, Ho), $\mathbf{Ho_2Sn_2O_7}$ [64] and $\mathbf{Pr_2Hf_2O_7}$ [65] proposed as QSL candidates.

2.3.3 Spin glass

Magnetism in materials manifests itself in different ways. On the one hand, there is a clear transition from disordered paramagnetic state into some ordered (ferro-, antiferro- or any other) state that's called long-range magnetic order. On the other hand, it's also possible that a magnetic system will never be able to achieve an ordered state down to the lowest temperature, and spins will continue to fluctuate due to long-range entanglement. Such a case means the quantum spin-liquid state. But is there anything in between, any intermediate state? Indeed, the spin-glass state is not uncommon.

Neither magnetic order, nor spin liquid. According to Mydosh [66, 67], a spin glass (SG) arises from *"a novel, yet classical, phase transition at a given temperature T_f into a new state of matter: a frozen glass of spins"*. Above a transition temperature, spins in SG materials show typical paramagnetic behavior, below T_f they are frozen in some random orientation. This is the point of

glassy behavior: there is neither definite magnetic order, periodicity of the spin pattern, nor persistent spin dynamics like in QSL. Spins are freezing co-operatively, however, could present some sort of frustration.

There are at least three mechanisms leading to the SG state: (i) randomness of the spin positions – site mixing, disorder, random distribution of magnetic ions, (ii) competing or mixed magnetic interactions meaning bond randomness due to structural or chemical disorder between the magnetic ions, and (iii) frustration in a classical spin liquid that lacks quantum effects needed to maintain spin dynamics down to 0 K.

One can find in describing of QSL candidates such expressions as *an absence of spin freezing* or *spin-glass behavior* to distinguish between the dynamic or frozen state in QSL candidates. Several techniques allow to quickly determine [67] whether spins exhibit static behavior in a material or not:

- Bifurcation of the DC susceptibility curves measured in zero-field-cooled (ZFC) and field-cooled (FC) regimes. The bifurcation indicates the freezing temperature T_f;
- Shift of the cusp temperature T_f with frequency ω on the real χ' and imaginary χ'' parts of the AC susceptibility;
- Absence of the sharp λ-peak in the magnetic specific heat data characteristic of the long-range order. Instead, linear-T dependence of the C_m below T_f and broad maximum above the transition temperature;
- Study of the aging process, *i.e.* time dependence of the magnetization, by the isothermal remanent magnetization (IRM) or the thermoremanent magnetization (TRM).

The listed methods combined with three SG criteria may determine a magnetic material to be a 'canonical' spin glass. However, one should distinguish the true spin glasses showing a clear transition into the frozen state and mimicked spin-glassy behavior when a part of the spins may freeze but without a phase transition. Therefore, additional measurements such as neutron scattering or μSR techniques [66] as a local probe of intrinsic magnetism, are needed to explore the real ground state of the material.

Spin-glass materials. The randomness and various kinds of defects play an important role in the formation of spin-glass state. Therefore, it's reasonable looking for them among magnetically disordered systems. Diluted allows were the first examples in which the SG state was recognized, and the main share of theoretical and practical methods were developed to describe this new phenomenon. In the diluted alloys, a small amount (about a few percent) of 'good' magnetic metal, *e.g.* Mn, Fe or Eu, is dissolved in the host non-magnetic metal; moreover, the distribution of magnetic impurities is completely random and the freezing of all spins occurs as a cooperative process. The well-known and well-studied diluted alloys are $\mathbf{Cu}_{1-x}\mathbf{Mn}_x$ (CuMn) and $\mathbf{Au}_{1-x}\mathbf{Fe}_x$ (AuFe). These compounds, also called canonical spin glasses, are a reference point for other systems with spin-freezing behavior.

Comparison of particular quantities, such as the frequency shift of T_f or the dynamical exponent zv, with a 'canonical' case helps to distinguish the truly SG material from spin-glass-like systems. Another scenario may be considered as the formation of frozen spin clusters (not a gradual process) that develop when temperature decreases. This behavior is typical for inhomogeneous systems deviating from the canonical ones.

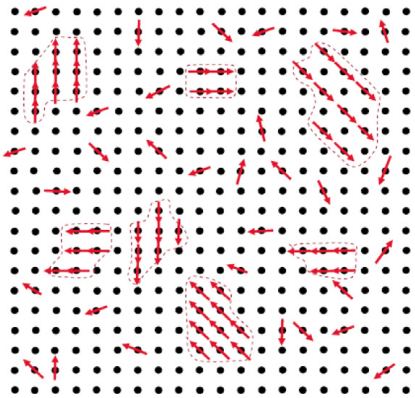

Figure 2.9: Representation of random-site spin-glass model in 2D with the inclusion of the ferromagnetic 'cluster glass' [67].

Since the 1970's when the classical spin glasses were explored and main principles of this novel state were established, spin-glass behavior has been detected for many other 2D or 3D systems. The SG phenomenon covers almost every class of compounds: diluted alloys, intermetallics, oxides, chalcogenides, heavy fermion metals and *etc*. The spin-glass transition can be triggered by a site mixing on the magnetic sublattice such in $\mathbf{Eu}_x\mathbf{Sr}_{1-x}\mathbf{S}$ or $\mathbf{K}_x\mathbf{Ru}_{4-y}\mathbf{Ni}_y\mathbf{O}_8$ [68]; competing magnetic interactions in $\mathbf{CuGa_2O_4}$ [69] or a complex framework of different magnetic moments in $\mathbf{Co_3Mn_3(O_2BO_3)_2}$ [70]. The spin-glassy behavior may also be detected in frustrated systems such as $\mathbf{La_2LiReO_6}$ and $\mathbf{Ba_2YReO_6}$ [71]. Although spin glasses do not cause much interest as QSL candidates, unexpected examples can still be found not only among disordered systems, but also among highly correlated or magnetically frustrated materials.

2.4 Kitaev materials as QSL candidates

In the previous section, a brief overview of state-of-the-art QSL candidates was given to demonstrate a variety of materials with unusual magnetic properties. They are not limited either by dimension or by the type of frustrated lattice. It was also announced that special attention will be paid to α-$RuCl_3$ and Ir-based compounds with honeycomb (2D) and hyperhoneycomb (3D) structure, and now their time has come.

2.4.1 α-$\mathbf{RuCl_3}$

Ruthenium trichloride is one of the most well-studied materials for the practical implementation of the Kitaev honeycomb model. The crystal structure of α-$RuCl_3$ is built only from $RuCl_6$ octahedra that are arranged in honeycomb layers in the *ab* plane (Fig. 2.10a). These layers lie on top of each other along the *c* direction with some offset, and are separated by a van der Waals gap. Weak but still noticeable spin-orbit coupling ($\lambda \sim 0.15$ eV [72]) affects

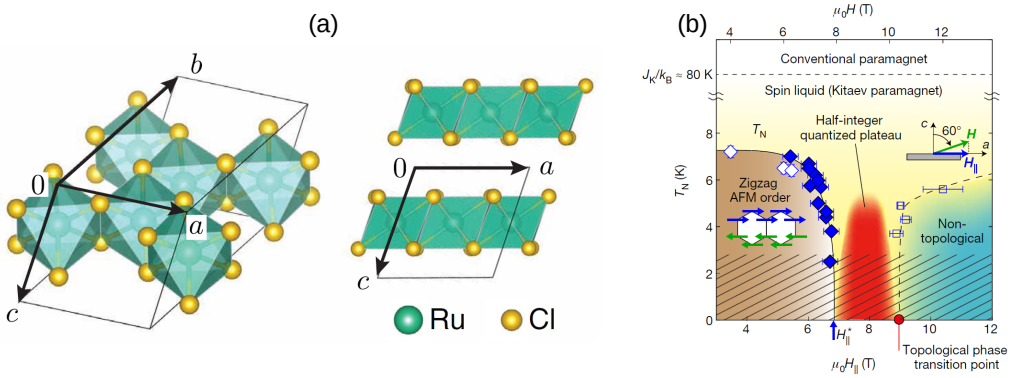

Figure 2.10: (a) Different views on the crystal structure of α-$RuCl_3$ [14]. (b) Field-temperature phase diagram of α-$RuCl_3$ [78].

the $4d^5$ electron structure of Ru^{3+} ion resulting in the $j_{\text{eff}} = \frac{1}{2}$ magnetic moment. In this case, spin-$\frac{1}{2}$ ruthenium ions form a perfect honeycomb lattice representing a promising realization of the Kiaev model. Unfortunately, thermodynamic measurements clearly indicate the zigzag magnetic order below $T_{\text{N}} = 7$ K [73] in zero field. However, the presence of magnetic order does not eliminate Kitaev physics in α-$RuCl_3$: a continuum of magnetic excitations (instead of well-define peaks) was found by using Raman spectroscopy measurements in a wide temperature (up to 100 K) and energy (up to 25 meV) range [74]. INS measurements [75–77], also confirm a broad continuum of fractionalized excitations consistent with the Raman experiments in the same temperature range. And looking above T_{N} is not the only way to avoid the ordered state.

Application of external magnetic field in the *ab* plane leads to a suppression of the magnetic order at $B_c \simeq 7.5$ T [77, 79] and triggers the appearance of a new phase related to spin-liquid behavior (also known as of a field-induced spin-liquid state [80] (Fig. 2.10b)). The new field-induced state was actively studied by different techniques revealing the similar picture of a broad continuum in the INS data [77], a half-integer plateau in the thermal Hall conductivity [78] (as a signature of Majorana fermions) and opening a spin gap detected by ^{35}Cl NMR [81]. The continuous studies of α-$RuCl_3$ in the context of the Kitaev QSL is still actively ongoing in order to shed light on the nature of the high-field phase, the borders of this phase, the physics of magnetic excitations at $B > B_c$ [82–84].

2.4.2 Family of honeycomb iridates

At the beginning, the main representatives of this family will be considered with a focus on the features of their synthesis and crystal structure, and the resulting magnetic properties. Looking ahead, it should be noted that all these compounds exhibit a long-range magnetic order and do not reach the QSL state. Earlier it was noted that one of the key points of the Kitaev model is the magnitude of the bond angle Θ (see p. 14) determining the nature of the interactions between magnetic ions (in this case, between Ir^{4+}). Adjusting the

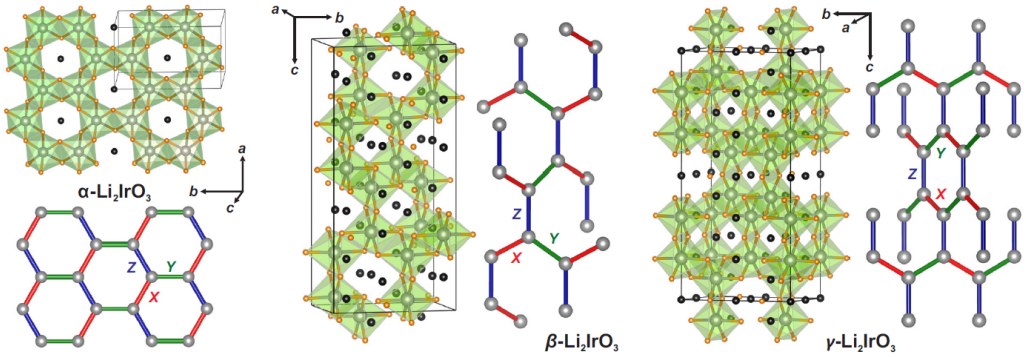

Figure 2.11: Crystal structures of three Li_2IrO_3 polymorphs with respect to the motif of Ir^{4+} ions: planar honeycomb (α), hyperhoneycomb (β), and stripy-honeycomb (γ) lattices [31]. Different colors show X-, Y-, and Z-bonds of the Kitaev model.

angle Θ by means of physical or chemical modifications allows to approach the proposed Kitaev QSL.

Therefore, the effect of external pressure applied to the Ir-based materials will be discussed further. On the other hand, chemical modification of the parent compounds can also act as a powerful tool to tune magnetic interactions on the honeycomb lattice. Examples of this approach will be demonstrated at the end of this section.

It is worth mentioning here again that the charm of the Kitaev model lies in its exact solution and QSL ground state. In turn, the Jackeli–Khaliullin mechanism provides specific instructions for finding materials suitable for the implementation of this model. Therefore, it's necessary to choose a proper ion with strong effect of SOC on the honeycomb lattice. Among heavy d transition-metal compounds, a family of Ir-based materials with a general formula A_2IrO_3 (A = Li, Na) perfectly fits the specified requirements. Ir^{4+} ion exhibits the $j_{\text{eff}} = \frac{1}{2}$ effective moment while polymorphism of iridates facilitates to cover both two- and three-dimensional cases of the iridium honeycomb network.

Layered sodium and lithium iridates. Both $\mathbf{Na_2IrO_3}$ and $\boldsymbol{\alpha}$**-**$\mathbf{Li_2IrO_3}$ compounds can be synthesized in polycrystalline and single-crystaline form. Polycrystalline samples are prepared by conventional solid-phase reaction between A_2CO_3 and IrO_2/Ir at high temperatures. The single crystals growth of Na_2IrO_3 occurs by further annealing the obtained polycrystals in air [85]. In the case of α-Li_2IrO_3, the crystals are grown by the vapor transport technique with using special arrangements [86]. Upon annealing in air, spatially separated Li and Ir metals first oxidize, then evaporate and transfer in the form of gaseous LiOH and IrO_3, and form single crystals on the deliberately placed spikes in the middle of the crucible.

Both Na_2IrO_3 [87] and α-Li_2IrO_3 [86] have a monoclinic structure with the space group $C2/m$. Edge-sharing IrO_6 octahedra form a planar honeycomb lattice AIr_2O_6, the voids of which are occupied by one part of the alkali metal

A (Fig. 2.11). Another part of A separate the honeycomb layers along the c direction. Because of layered nature of the crystal structure, 2D iridates suffer from planar defects [86, 88]: stacking faults and twinning, the latter is unique to α-Li_2IrO_3. These types of disorder certainly affect the magnetic properties of Na_2IrO_3 and α-Li_2IrO_3 leading them away from the Kitaev QSL.

At high temperatures, the magnetic susceptibilities of Na_2IrO_3 and α-Li_2IrO_3 follow the Curie–Weiss law, the extracted effective moments [85, 86, 89] are close to the ideal value of 1.73 μ_B for the pure Ir^{4+} with $j_{\text{eff}} = \frac{1}{2}$. However, the characteristic Curie–Weiss temperatures θ_{CW} are dramatically large and highly anisotropic that contradicts with the uniform nature of the Kitaev model. In the case of Na_2IrO_3, the Curie-Weiss temperatures with respect to the lattice direction were found as $\theta_{ab} \sim -180$ K and $\theta_c \sim -40$ K [89]. For α-Li_2IrO_3, the Curie–Weiss temperatures are $\theta_{ab} \sim 4$ K and $\theta_c \sim -58$ K [88]. Moreover, both layered iridates undergo the long-range magnetic order. Na_2IrO_3 demonstrates zigzag order [90] with the propagation vector $\mathbf{k} = (0, 1, \frac{1}{2})$ below the range 13–18 K [85] that is also confirmed by INS and μSR measurements [91]. α-Li_2IrO_3 shows a transition to an incommensurate magnetic order below $T_N \sim 15$ K [92] with the propagation vector $\mathbf{k} = (0.32(1), 0, 0)$ [92]. The magnetic structure can be represented as counter-rotating spiral order of spins on the honeycomb lattice. In addition, signs of unusual magnetic excitations at $T > T_N$ were reported for α-Li_2IrO_3 in INS [93] and Raman [94] spectroscopy measurements.

It seems that the presence of LRMO should definitively exclude spin-liquid behavior in the honeycomb iridates. On the one hand, that's true and the ground state is magnetically ordered. On the other hand, there is still 'a small space' for the frustration and Kitaev physics. The first point is a simple but useful criterion $f = \theta_{CW}/T_N$ [1] which lies in the range from 5 to 10 indicating a strong frustration effect. The second point is *ab initio* calculations resulting in the dominant Kitaev interactions in the spin Hamiltonian for both materials. However, additional interactions such as further Heisenberg terms or Dzyaloshinskii-Moriya interactions [17] must be taken into account because they are also involved into establishing the magnetically ordered state in Na_2IrO_3 and α-Li_2IrO_3.

Three-dimensional variations of lithium iridate. The polymorphism of Li_2IrO_3 allows one to realize Kitaev QSL in 3D. Probably, the right ion ratio between Li^+ and Ir^{4+} opens the way to new structure derivatives in contrast to the layered Na_2IrO_3. To distinguish the planar and three-dimensional modifications of lithium iridates, the following notations are used: hyper-honeycomb and stripy-honeycomb (or harmonic-honeycomb) lattices for β-$\mathbf{Li_2IrO_3}$ and γ-$\mathbf{Li_2IrO_3}$, respectively.

β- and γ-phases can be synthesized in a similar way as their layered analogues. β-Li_2IrO_3 is a high-temperature modification of the α-phase and forms above 1000-1100 °C [89] by simple annealing of the parent compound. Single crystals of β-polymorph are obtained by the same vapor transport technique [86] at higher temperatures than α-Li_2IrO_3. The γ-phase is grown from the mixture of LiOH flux and pre-annealed reactants at 700-800 °C [95].

It could be slightly confusing to imagine a planar honeycomb network in three dimensions, but it's still possible. In the case of β-Li_2IrO_3, the crystal structure can be represented as a distorted cubic closed-packed oxygen arrangement (the orthorhombic space group *Fddd*), in which Ir and Li atoms occupy all octahedral voids in a specific manner [96, 97]. Iridium atoms form zigzag chains propagating in the *ab* plane and alternating along the *c* direction (Fig. 2.11). In the local view, one Ir atom has three Ir neighbors, almost equally distant from each other, representing *X*- and *Y*-bonds within the chains and *Z*-bonds linking the chains in the notation of the Kitaev model. γ-Li_2IrO_3 crystallizes in the orthorhombic *Cccm* space group, the structure is built from stripes of honeycomb plaquettes (hence the name *stripy-honeycomb*) alternating along the *c* direction as zigzag chains in the β-phase. The *XYZ*-bond notation is also applicable in this case, however, two types of *Z*-bond are presented: one type is for the bond binding alternating stripes, another type is for the interchain connection within one honeycomb plaquette.

3D nature of the crystal structure affects the magnetism of β- and γ-polymorphs. The anisotropy in magnetic parameters becomes more pronounced than in α-Li_2IrO_3 or Na_2IrO_3. The Curie–Weiss temperatures θ_{CW} of β-phase differ not only in absolute values but also in the sign for all three directions ($\theta_a \sim -33$ K, $\theta_b \sim 44$ K and $\theta_c \sim 53$ K) [98], while the effective magnetic moment lies in a wide range [98, 99] for both iridates. As noted earlier, both β- and γ-Li_2IrO_3 undergo long-range magnetic order below $T_N = 37 - 38$ K (β) [96, 97], and 39.5 K (γ) [95], respectively. Surprisingly, magnetic structures of all Li_2IrO_3 modifications share a lot of commonalities; the ordered state in β- and γ-polymorphs is described as incommensurate order with counter-rotating spirals [96, 100] and the propagation vector $\mathbf{k} = (0.57(1), 0, 0)$.

Another distinctive mark of anisotropic magnetic behavior in 3D iridates is the strong field-dependence along the *b* axis [95, 98]. When the magnetic field is applied along this direction, the ordered state is suppressed above the field $H > 3$ T [98, 101, 102], however, this does not lead to the QSL state. For instance, the field-induced state of β-Li_2IrO_3 above $B_c = 2.7$ T [98] does not break any symmetry and can be classified as quantum paramagnet state in which part of the spins are polarized along the *b* direction. In addition, a weak magnetic anomaly at ~ 100 K was detected by magnetization, heat capacity, and μSR measurements [103]. The nature of this anomaly is not completely clear, however, one may speculate that there is some intermediate state in β-Li_2IrO_3 accompanied by spin-orbital interactions. *Ab initio* calculations suggest that the ferromagnetic Kitaev term *K* and the off-diagonal anisotropy Γ dominate β-Li_2IrO_3 [104–107], moreover, these terms are almost of the same order, $|K| \simeq |\Gamma|$ [106, 108].

2.4.3 Pressure induced dimerization

Failure to achieve the quantum spin liquid in Ir-based iridates triggered interest in finding other possible ways to reach this state. Deviations from the pure Kitaev model meaning not only comparable values of the Kitaev and

off-diagonal terms in the spin Hamiltonian but also presence of additional exchange interactions, make one think about alternative mechanisms for tuning magnetic properties. One of these approaches is the application of external pressure. Compression of the unit cell may affect the local geometry of Ir^{4+} ions and lead to a change in the crucial parameter Θ – the Ir–O–Ir bridging angle, which is decisive for the strength of exchange interactions (see p.14).

2D iridates under pressure. In comparison with Li_2IrO_3 polymorphs, **Na_2IrO_3** is robust against external pressure. Theoretical calculations predict structural and magnetic phase transitions well above 40 GPa from the ordered state to bond-ordered nonmagnetic one [109]. On the other hand, high-pressure experiments do not show any structural deviations from the original $C2/m$ space group via persistent $j_{\text{eff}} = \frac{1}{2}$ state up to 58 GPa [110, 111]. However, the controversial results may be found in [112] claiming the structural transitions at 3 and 10 GPa by infrared spectroscopy and resistivity measurements.

α-Li_2IrO_3, on the contrary, undergoes a structural phase transition at room temperature around $P_d \simeq 3.8$ GPa [113, 114] from the monoclinic $C2/m$ to the triclinic $P\bar{1}$ space group. The transition is accompanied by an abrupt decrease of the cell volume and shortening of $\frac{1}{3}$ of the Ir–Ir bonds. Such phenomenon is generally called *dimerization* meaning the transition into a new nonmagnetic dimerized phase (magnetic collapse) above the critical pressure P_d and formation of Ir–Ir dimers with short bond distances in the crystal structure. In α-Li_2IrO_3, the dimerization occurs on the iridium honeycomb lattice in the ab plane, predominantly along X or Y bonds. The structural and magnetic phase transition was also probed by optical [115] and Raman [94] studies on single crystals revealing dimerization at comparable critical pressure P_d.

Dimerization on the hyperhoneycomb lattice. **β-Li_2IrO_3** shows the most interesting behavior under pressure among other iridates.

Firstly, the structural phase transition into the fully dimerized phase occurs in the range of $P_d \sim 3.8 - 4.4$ GPa [116, 117] at room temperature accompanied by symmetry reduction from $Fddd$ to $C2/c$ (Fig. 2.12a). Anisotropic nature of the hyperhoneycomb lattice implies a non-equivalent Ir–Ir bond network, and a particular direction of the dimerization can be defined. The formation of Ir–Ir dimers occurs within the zigzag chains by a shortening of Y-bond in the notation of the Kitaev model.

Secondly, at low temperatures the dimerization in β-Li_2IrO_3 originates already at $p_c \simeq 1.4$ GPa [106, 118], well below P_d (Fig. 2.12b). Previous μSR experiments [106] detected a combination of frozen and dynamic spins above p_c suggesting the emergence of the pressure-induced spin-liquid state along with spin-glassy state that could be a consequence of coexistence of different phases (Fig. 2.12c). However, recent magnetization measurements under pressure have revealed that above p_c the breakdown of magnetic order occurs due to formation of the intermediate partially-dimerized ($P2_1/n$) phase in which one half of Ir^{4+} sites are nonmagnetic forming Ir–Ir dimers, and the other half of Ir^{4+} sites are magnetic contributing to magnetic response in

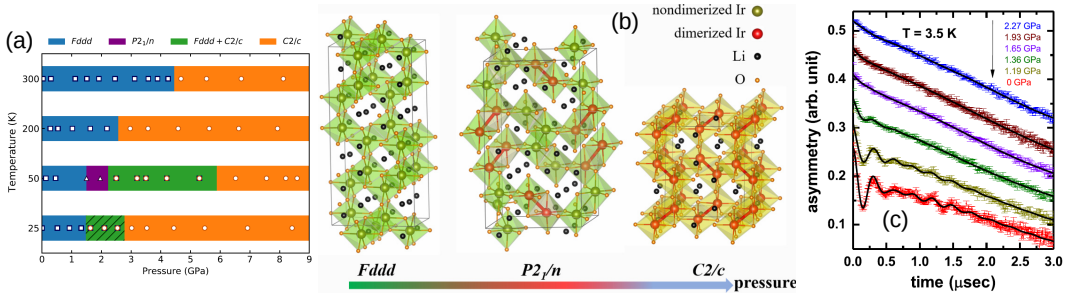

Figure 2.12: (a) Evolution of the β-Li_2IrO_3 crystal structures under pressure [117]. (b) Comparison of the nondimerized ($Fddd$), partially dimerized ($P2_1/n$), and fully dimerized ($C2/c$) phases of β-Li_2IrO_3 under pressure . Red Ir—Ir bonds denote the dimerized Ir^{4+} ions [118]. (c) Zero-field μSR time spectra at 3.5 K from [106]. Suppression of the oscillations with pressure indicates the reduction of fraction of the magnetically ordered phase.

susceptibility data and spin dynamics in the μSR experiments [106]. Thus, in β-Li_2IrO_3 the breakdown of magnetic order under pressure no longer leads to a pressure-induced transition into spin-liquid state, but a formation of partially-dimerized phase. The *ab initio* calculations [118] suggest a singlet ground state in this new intermediate phase with similar values of $K\Gamma J$ exchange constants as for the ambient-pressure values of β-Li_2IrO_3.

In summary, the application of external pressure on honeycomb and hyperhoneycomb iridates leads away from the desirable QSL state to the opposite result – dimerization and loss of magnetism. Compression of the unit cell reduces the angle Θ toward $\sim 90^\circ$ where the influence of the Kitaev interactions are weak. Therefore, as an alternative way to tune the magnetism in these systems, chemical substitution should be considered.

2.4.4 Ion-exchange reactions in inorganic materials

Before the chemical modifications of the parent A_2IrO_3 compounds are described, basic principles of the topotactic reactions should be presented. The definition *topotactic* reaction refers to a modification of existing solid state structure with maintaining of the basic motif of the parent compound. In this case, the precursors of the reaction are a parent (*host*) material and a reactant (*guest*) compound which could be atoms, ions, molecules or even clusters. In principle, they can be divided into several different types:

- **intercalation** with penetration of the guest particles into the host material without a formation of a byproduct;
- **deintercalation** by removing guest particles from the host material;
- **ion exchange** between two materials that involve an exchange of one or more ionic components [119].

While the intercalation/deintercalation reactions are commonly used in synthesis of channel, layer and framework compounds, battery materials,

nanoparticales, and zeolites [120], the ion exchange reactions can be suggested for synthesis of new functional materials, particularly, new QSL candidates.

Conditionally, the topotactic ion-exchange reaction can be represented by the general equation:

$$H\text{-}A + B\text{-}X \rightarrow H\text{-}B + A\text{-}X, \tag{2.11}$$

where HA stands for the host compound with the guest atom A, BX is a reactant with the doping element B, HB is a new substituted parent compound, and AX is a byproduct of the ionic exchange reaction. The topotactic ion-exchange can be performed by chemical or electrochemical synthesis methods using non-aqueous, aqueous, and melt techniques. The strength of this approach is that the reaction can be performed under mild conditions: low temperature of the synthesis, usage of binary salts as a dopant.

For the proper chemical substitution, one should also take into account two factors. The first one is geometrical or spatial factor. The size of exchanged ions/atoms should be at least comparable to each other, and interlayer space in 2D structures or size of the voids in 3D ones should be large enough to host the new doping element. In this case, the ionic exchange into the layered compounds could be more effective than into the close-packed 3D analogs. The second factor is chemical similarity of the substituted and doped atoms. To avoid unexpected results due to red-ox processes or chemical transformation, replaced ions should have the same oxidation state or exhibit similar chemical properties like isovalent substitution or group properties in the periodic table of elements. This part is less crucial for the topotactic ionic exchange as it depends on the aim of the chemical modification. However, the combination of these two factors greatly facilitates the search for new materials.

2.4.5 Chemical substitution into the layered A_2IrO_3

Chemical modification of the honeycomb iridates can be performed in two ways: partial or full substitution of alkali metal A in A_2IrO_3 or doping on the iridium site by non-magnetic ions. In all cases the substitution are oriented on changing the local environment of Ir^{4+} ions to tune the angle Θ and the value of Ir–Ir interactions keeping the honeycomb motif of IrO_6 octahedra unaffected. While substitution on A sites provides a great variety of new materials with intriguing properties, non-magnetic doping on the Ir^{4+} site on the honeycomb lattice destroys the complex magnetism. Thus, isoelectronic substitution via Ti^{4+} [121] or Rh^{4+} [122] doping leads to spin-glassy behavior at low temperatures. Since parent compounds already contain some sort of defects, unnecessary disorder on the magnetic honeycomb lattice must be avoided.

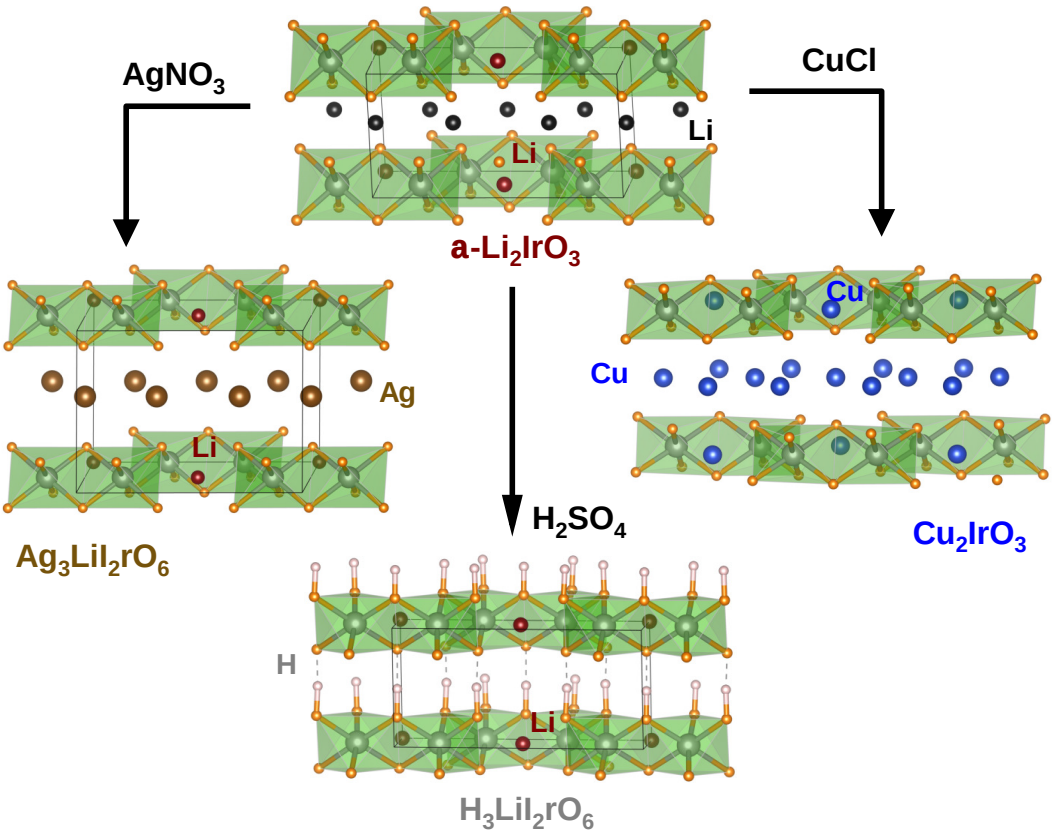

Figure 2.13: Chemical substitutions in α-Li_2IrO_3 via monovalent ions [31]. Parent structure contains Li atoms between the honeycomb layers (black), as well as in the centers of Ir hexagons (dark red). Only the former Li atoms are exchanged in $Ag_3LiIr_2O_6$ and $H_3LiIr_2O_6$, whereas a complete substitution is achieved in Cu_2IrO_3.

For now, chemical substitution has been presented exclusively for the layered iridates [1]. Li or Na atoms can be replaced by mono- and divalent ions while keeping the oxidation state of Ir at 4+. In general, new derivatives of the honeycomb iridates are synthesized by topotactic low-temperature ionic-exchange reaction. Exceptions are the $(Na_{1-x}Li_x)_2IrO_3$ solid solution for which single crystals can be obtained by the same technique as for pure Na_2IrO_3, and $H_3LiIr_2O_6$ prepared hydrothermally (see below). Chemical substitution by ionic exchange allows one to obtain new Kitaev iridates, which cannot be synthesized in any other way, for example, by a high-temperature annealing. On the other hand, new compounds are available as polycrystalline samples only, and it narrows the choice of characterization methods: for such anisotropic systems, the single-crystal experiments would be more informative.

[1] In fact, synthesis of β-H_2IrO_3 has been reported [123] in the vein of an electrocatalytic water splitting, but no magnetic studies were presented so far.

Substitution with monovalent cations. The most suitable option for chemical modifications seems the possible solid solution between Na_2IrO_3 and α-Li_2IrO_3. Despite the identical crystal structures, Na can only be partially substituted by Li leading to the $\mathbf{(Na_{1-x}Li_x)_2IrO_3}$ limited solid solution with the $x_{max} \simeq 0.25$ [124]. In this case, Li occupies hexagonal voids on the iridium honeycomb lattice forming $LiIr_2O_6$ planes separated by unaffected layers of Na, so the formula can be rewritten as "$Na_3LiIr_2O_6$". The LRMO persists upon Li doping, but the transition temperature is suppressed down to $T_N = 5.5$ K [124] for the maximum substitution level. The type of magnetic order is no longer simple zigzag one, but shows short- or long-range correlations hinting at a more complex magnetic behavior and local disorder [125, 126].

The next step in the synthesis of new iridates is doping by monovalent cations with comparable ionic radii of Li^+ or Na^+ ions. Probably, the only such candidates are nonmagnetic d^{10} Cu^+ and Ag^+ cations. Using CuCl [127] and $AgNO_3$ [128] as a source of required ions, new Kitaev iridates can be synthesized by a topotactic reaction. The partially substituted iridates – $\mathbf{Cu_3LiIr_2O_6}$, $\mathbf{Cu_3NaIr_2O_6}$ and $\mathbf{Ag_3LiIr_2O_6}$ – have the same crystal structure (Fig. 2.13): Li(Na)Ir_2O_6 honeycomb planes are separated by the nonmagnetic buffer layers of Cu or Ag atoms similar to "$Na_3LiIr_2O_6$" mentioned above. In the case of **Cu-substituted** compounds [127], the specific heat measurements as well as powder neutron diffraction indicate the suppression of magnetic order due to an absence of characteristic sharp anomalies in the data. On the other hand, large negative Curie–Weiss temperatures ($\theta_{CW} = -113$ K for $Cu_3NaIr_2O_6$ and $\theta_{CW} = -145$ K for $Cu_3LiIr_2O_6$) along with peak-like anomalies in the magnetic susceptibility around $\sim$ 15 K suggest predominantly antiferromagnetic behavior of these compounds. A slightly different picture arises for Ag-substituted iridate. Initially, $\mathbf{Ag_3LiIr_2O_6}$ seemed to be in close proximity to the Kitaev spin liquid [129]. The significant interlayer expansion by large Ag atoms was thought to induce a strong spin-orbit coupling mediated via the O–Ag–O bonds between the layers. The absence of magnetic order or spin freezing along with a two-step release of the magnetic entropy supported the idea of the QSL behavior. However, further examination of $Ag_3LiIr_2O_6$ revealed that structural disorder, in particular stacking faults, drastically affects the magnetic properties of this material. It turned out that the samples with a low concentration of stacking faults demonstrate long-range antiferromagnetic order below $T_N = 14$ K [130], and the proximity to the Kitaev spin liquid was a consequence of structural randomness in the crystal structure.

The full substitution of Na atoms in Na_2IrO_3 by treating with CuCl leads to another new Kitaev iridate, $\mathbf{Cu_2IrO_3}$ (Fig. 2.13). At low temperature it demonstrates a weak magnetic order, and a large Curie–Weiss temperature $\theta_{CW} = -110$ K in combination with a small $T_N = 2.7$ K indicates significant frustration index $f = |\theta_{CW}|/T_N$ of 40 assuming proximity to the QSL ground state [131]. Unfortunately, the stacking fault legacy of the parent compound is also presented in this case [132]. Moreover, mixing occupancy of

Cu/Ir sites introduces an additional disorder on the iridium honeycomb lattice: Cu^{1+}/Ir^{4+} cation disorders [131] dilute the honeycomb spin lattice and $Cu^{1+}(Ir^{4+})/Cu^{2+}(Ir^{3+})$ mixed valence due to oxidation and reduction processes creates a nonmagnetic and magnetic impurities breaking honeycomb pattern [132, 133]. The μSR experiments reveal coexistence of static and dynamic spins at low temperatures suggesting that the static contribution is caused by Cu^{2+} magnetic impurities while the undistorted parts of the honeycomb lattice manifest the Kitaev spin liquid [132]. From another point of view, the abundance of structural and chemical defects in Cu_2IrO_3 would rather cause disordered magnetism that mimics the QSL state.

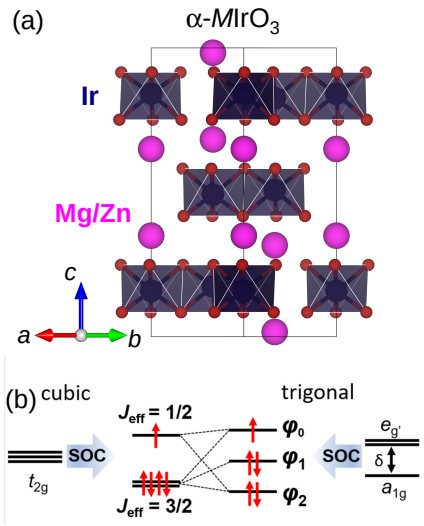

Figure 2.14: (a) Crystal structures of α-MIrO$_3$, where M = Mg, Zn or Cd. (b) Schematic illustration of the trigonal distortion in α-CdIrO$_3$.

Probably, the most promising QSL candidate among all chemically modified iridates known so far is a partially substituted $\mathbf{H_3LiIr_2O_6}$ (Fig. 2.13). Not only monovalent metals but also a hydrogen ion H^+ can play a role of the dopant. In contrast to other chemical derivatives of the layered iridates, $H_3LiIr_2O_6$ is synthesized hydrothermally by treating α-Li_2IrO_3 in sulfuric acid [134, 135], and can be obtained in both powder and single crystal form [136]. Thermodynamic measurements along with local probes by ^{1}H and ^{7}Li NMR reveal the absence of magnetic ordering down to 50 mK [135] as well as persistence of spin dynamics and low-energy excitations at the lowest temperatures examined by specific heat measurements. These observations imply that the ground state of $H_3LiIr_2O_6$ may be the Kitaev spin liquid. However, various kinds of defects in this material cast doubt on the QSL behavior. Firstly, there is abundance of the notorious stacking faults [134] inherent in all other layered iridates. Secondly, hydrogen atoms can occupy random positions between the $LiIr_2O_6$ magnetic honeycomb layers forming strong interlayer O–H$\cdots$O hydrogen bonds affecting also Ir–O bond distances. Both detailed crystal structure analysis [134] and *ab initio* calculations [137] indicate that H–O bonds affect the stacking pattern of the honeycomb layers and introduce randomness of magnetic interactions. Therefore, a random-singlet state instead of the Kitaev spin liquid may be a reason for the suppressed magnetic order in $H_3LiIr_2O_6$.

Substitution with divalent cations. The number of monovalent ions suitable for substitution into layered sodium and lithium iridates is limited. The main criteria for doping elements are the ionic radius comparable to Li^+

or Na^+ radii, and the ion charge to keep the oxidation state of Ir^{4+}. Moreover, the doping cations should be non-magnetic to prevent the disturbance of the honeycomb lattice due to additional magnetic interactions. As a solution, divalent metals may be considered as a doping element, resulting in the composition α-MIrO$_3$ where M is non-magnetic Mg^{2+}, Zn^{2+} or Cd^{2+} ions.

All three α-MIrO$_3$ compounds were synthesized via a low-temperature metathesis reaction using proper metal chlorides (in the case of Cd, an inert salt of NaCl is added to stabilize the target compound) [138, 139]. Due to divalent nature of the ions, the crystal structure of new iridates transforms from monoclinic to rhombohedral lattice system with the space group of $R\bar{3}$. In this case, the honeycomb layers of Ir_2O_6 with unoccupied voids are stacked along the c direction separated by buffer ions of M (Fig. 2.14a). Both **α-MgIrO$_3$** and **α-ZnIrO$_3$** exhibit a long-range magnetic order below 31.8 and 46.6 K [138], respectively. Comparable values of Curie-Weiss temperatures θ_{CW} and transition temperatures T_N result in the small values of the index f of 1.02 to 2.11 for both materials indicating a minor role of frustration effects on the honeycomb lattice. In the case of **α-CdIrO$_3$**, IrO_6 octahedra experience a strong trigonal distortion (Fig. 2.14b) leading to an effective magnetic moment of $\mu_{eff} = 2.26(4)\ \mu_B$ [139] and deviation from the $j_{eff} = 1/2$ moment of Ir^{4+} state. Additionally, α-CdIrO$_3$ undergoes a magnetic order at $T_N = 91$ K [139] like the other MIrO$_3$ compounds.

2.5 Motivation

Magnetic compounds with 2D or 3D spin lattices may serve as a suitable playground for the frustrated magnetism and spin-liquid behavior. There are variety of materials prone to such peculiar state that is caused by geometrical frustration. However, the number of compounds showing frustrated magnetism due to the bond-dependent exchange interactions is limited. Application of the Kitaev model along with the Jackeli–Khaliullin mechanism to real systems extends the list of QSL candidates and opens new ways for practical realization of this concept.

The family of Ir-based compounds with honeycomb-like lattice fits well in the Kitaev model. Nevertheless, pristine Na_2IrO_3 and polymorphs of Li_2IrO_3 are magnetically ordered and deviate from the pure QSL state. Probably, application of external stimuli or chemical modifications could improve the magnetic properties of these materials and bring closer to QSL. However, external pressure induces the magnetic collapse and eventually leads to the non-magnetic dimerized state. Chemical substitution of the alkali metals can suppress the magnetic order in some cases, but a new spin-liquid-like behavior may be explained as a disordered magnetism introduced by structural defects and randomness of magnetic interactions. Table 2.1 summarizes the most relevant parameters of the pure honeycomb-like iridates and their chemical derivatives.

Taking into account all of the above, β-Li_2IrO_3 may be considered as a good starting point for finding of new Kitaev materials with the hyperhoneycomb lattice. Several benefits should be mentioned:

- In contrast to the layered iridates, β-polymorph is structurally well ordered and does not suffer from stacking faults.
- The breakdown of magnetic order under pressure is accompanied by an intermediate partially-dimerized state. The suppression of magnetism occurs gradually with coexistence of frozen and dynamic spins. It means that with proper tuning tools, it's possible to find an optimal state in which spins can fluctuate without ordering or freezing.
- No results of chemical substitution into β-Li_2IrO_3 have been reported by now. Therefore, new QSL candidates with 3D honeycomb lattice may be synthesized by using the topotactic ionic exchange reaction as was done for the layered iridates.

Table 2.1: Summary of parent sodium and lithium iridates as well as their derivatives synthesized by ion-exchange reactions. The ionic radius r is presented for the six-fold coordinated ion [140]. The temperature θ_{iso} for γ-Li_2IrO_3 is not given due to a strong deviation from the Curie-Weiss law. The frustration index defined as $f = |\theta_{CW}|/T_N$, is not applicable for γ-Li_2IrO_3 and $H_3LiIr_2O_6$ (denoted as question mark). The asterisk marks the lowest measured temperature for $H_3LiIr_2O_6$ (no magnetic order down to 50 mK [135]).

Compound	r (Å)	μ_{eff} (μ_B)	θ_{iso} (K)	T_N (K)	f	Ref.
Na_2IrO_3	1.02	1.79	-120	$13-18$	8	[89, 92]
α-Li_2IrO_3	0.76	1.83	-33 to -100	~ 15	~ 5	[89, 92]
β-Li_2IrO_3	0.76	1.7–2.0	$+21$	$37-38$	0.6	[97]
γ-Li_2IrO_3	0.76	1.9–2.4	–	~ 40	?	[95]
"$Na_3LiIr_2O_6$"	0.76	1.8–2.0	-70	5.5	12.3	[124]
$Cu_3LiIr_2O_6$	0.77	2.1	-145	~ 15	9.7	[127]
$Cu_3NaIr_2O_6$	0.77	2.0	-113	~ 15	4.1	[127]
$Ag_3LiIr_2O_6$	1.15	1.87	-132	14	9.4	[130]
Cu_2IrO_3	0.77	1.93	-110	2.7	40	[131]
$H_3LiIr_2O_6$	–	1.60	-105	0.05*	?	[135]
α-$MgIrO_3$	0.72	1.73	-67.1	31.8	2.11	[138]
α-$ZnIrO_3$	0.74	1.73	-47.5	46.6	1.02	[138]
α-$CdIrO_3$	0.96	2.26	-280	90.9	3.08	[139]

Chapter 3

Synthesis and crystal structure

3.1 Synthesis of new Kitaev iridates

Layered sodium and lithium iridates have shown themselves as a good platform for chemical substitution to obtain new materials hosting Kitaev physics on the honeycomb lattice. Extending this idea to the three dimensional case, β-Li_2IrO_3 may act as a practical realization of the Kitaev model on the hyperhoneycomb lattice. And new derivatives may be obtained by the similar topotactic ion exchange reaction as in the case of Na_2IrO_3 or α-Li_2IrO_3. However, the robust nature of β-Li_2IrO_3 crystal structure limits the number of doping elements (Fig. 3.1). Li and Ir atoms occupy all octahedral positions without leaving any voids meaning that the size of the doping metal ion should be comparable with the lithium one. Moreover, the doping metal must be even smaller than Na^+ ion: difference between ion radii of alkali metals is not crucial but there is no "β-Na_2IrO_3" with the hyperhoneycomb lattice meaning that the size of Li ion is optimal for this family of iridates. Interestingly, β-Na_2PtO_3 does exist with the hyperhoneycomb motif of PtO_6 octahedra [141]. According to the table 3.1 of ionic radii for selected metals, only Cu^+ may be chosen for the ionic exchange because Ag^+ ion is too large in this case (also for the layered systems, only partially substitution is possible, see $Ag_3LiIr_2O_6$ [128, 130]). On the other hand, divalent metals offer more options: the radii of Mg, Zn and Cu ions are quite close to the Li^+ one. However, magnetic properties of Cu^{2+} ion should be taken into account: the electronic configuration ($3d^9$) implies the spin-$\frac{1}{2}$ behavior that would introduce unnecessary magnetic impurities on the hyperhoneycomb lattice.

Table 3.1: List of ionic radii r for the six-fold coordinated mono- and divalent ions [140] potential for ionic exchange.

Monovalent ion	r (Å)	Divalent ion	r (Å)
Li^+	0.76	Mg^{2+}	0.72
Cu^+	0.77	Cu^{2+}	0.73
Na^+	1.02	Zn^{2+}	0.74
Ag^+	1.15	Cd^{2+}	0.95
		Ca^{2+}	1.00

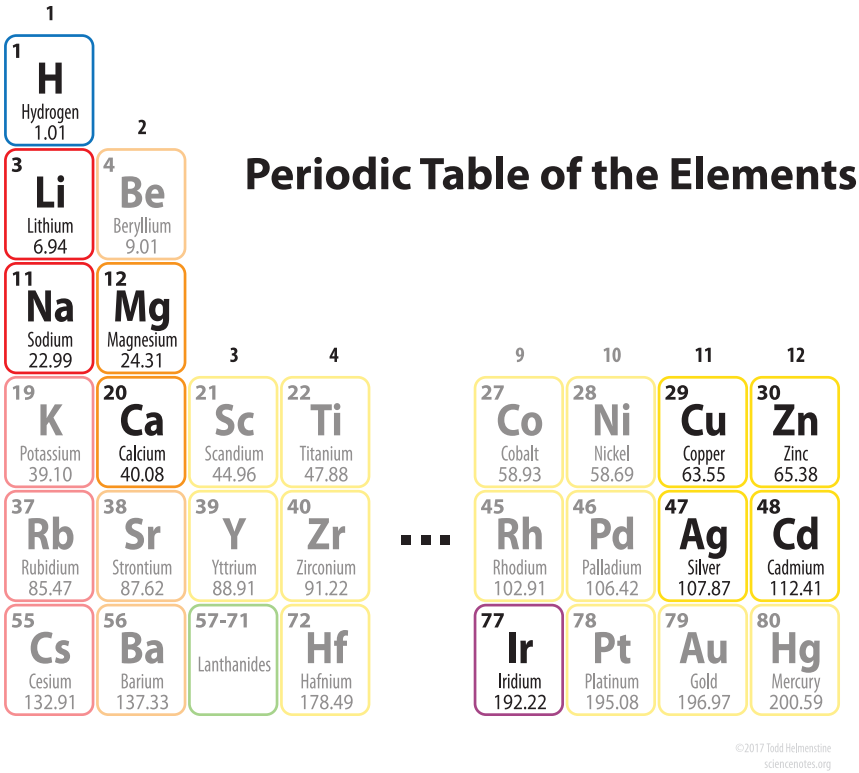

Figure 3.1: Part of the periodic table of the elements highlighting the most promising metals for the ionic substitution.

As for the other metals, substitution with Cd may lead to a large distortion of the crystal structure as in the case of $CdIrO_3$ [139]. Additionally, there is the post-perovskite phase of $CaIrO_3$ showing the orthorhombic structure without the honeycomb motif of IrO_6 octahedra along with the quenched $j_{\text{eff}} = \frac{1}{2}$ state [142].

Preparation of the parent compound The polycrystalline samples of β-Li_2IrO_3 were synthesized by a conventional solid state reaction from Li_2CO_3 ($\geq$ 99.99%, Alfa Aesar) and powder of Ir (99.95%, ChemPUR) in a molar ratio of 1.05 : 1. The well-ground mixture was placed in an alumina crucible, heated within three hours and annealed at 1050 – 1100 °C for 48 h in air [88], then furnace cooled to room temperature. The obtained powder product contained a mixture of the α- and β-polymorphs in a roughly equivalent ratio. Therefore, the mixture was re-ground several times and heated at the same temperature until the pure phase of β-Li_2IrO_3 was obtained. The overall reaction is expressed as

$$Li_2CO_3 + Ir + O_2 \xrightarrow{\text{air}} \beta\text{-}Li_2IrO_3 + CO_2 \uparrow . \tag{3.1}$$

The purity and quality of the synthesized parent compound were confirmed by x-ray diffraction (XRD).

3.1.1 Monovalent substitution

The first task was to perform isovalent substitution of Li with Cu(I) by a similar ionic exchange reaction as in the case of Cu_2IrO_3 [131]: mixture of β-Li_2IrO_3 and CuCl (99.995%, ROTI®METIC) in the mole ratio of 1 : 3 was placed into a covered alumina crucible and sealed under Ar in a quartz tube/ ampule. All sample preparations were performed in an argon glovebox due to the high hygroscopicity of the salts used. The sealed ampule with the mixture was heated at $1.5 - 2$ °C/min to $350 - 380$ °C, kept for $16 - 24$ h, and then cooled to room temperature. Excess of CuCl was removed by treating the sample with concentrated hydrochloric acid, the rest of the undissolved sample was washed several times with distilled water and dried by rinsing with acetone.

Surprisingly, this attempt was unsuccessful, and the resulting sample contained the pure β-polymorph without any sign of a new phase forming: reflection positions and profiles as well as cell parameters were unaffected. Further variation of reaction conditions haven't made any improvements: changing the mole ratio and increasing the heating time to 80 h gave the same negative result, the gradual increase of the reaction temperature up to $\sim$ 440 °C led to a partial degradation of the parent compound with the formation of IrO_2 as an impurity. After numerous synthesis attempts, it was concluded that Cu^+, probably, can't substitute Li^+ in β-Li_2IrO_3.

As was noticed earlier, the ionic radius of Ag atom is incompatible with the radius of Li^+, and one shouldn't expect any noticeable Ag substitution in β-polymorph. However, low-temperature ion exchange reaction could work to synthesize metastable compounds, particularly, when the doping ion is larger than the substituted one. Therefore, several attempts have been made to check the possibility of silver doping in β-Li_2IrO_3. AgCl (99.999%, Aldrich) or $AgNO_3$ (99.9995%, Alfa Aesar) were used as a source of Ag^+ ion for the ionic exchange reaction. The syntheses were performed in the same conditions as in the case of Cu^+-doping (see Table 3.2). In the result, as expected, no ionic exchange between β-Li_2IrO_3 and silver salts occurred, and no new products of lithium substitution were detected.

3.1.2 New iridates β-MIrO$_3$

The substitution with monovalent metals demonstrates a negative result without formation of new iridates. Due to the limited number of elements suitable for the ionic exchange, divalent metals must be considered as the next step for searching of new Kitaev materials based on β-Li_2IrO_3. Looking ahead, it is worth mentioning that divalent metal doping leads to new Kitaev iridates β-MIrO$_3$ where M = Zn or Mg. In order to avoid confusion with the layered honeycomb derivatives, new compounds are labeled with a β prefix as a reference to β-Li_2IrO_3 with the hyperhoneycomb lattice.

β-ZnIrO$_3$ The synthesis of the new zinc iridate was performed in a similar way as Cu_2IrO_3 [131] and the attempt with CuCl. In this case, $ZnCl_2$

(99.999%, Aldrich) was used as a source of Zn^{2+} ions, the mole ratio between the parent compound and an excess of zinc chloride varied between 1 : 1 and 1 : 3. Temperature and duration of the synthesis were also adjusted to optimize the reaction conditions. The best result was achieved by heating the mixture of β-Li_2IrO_3 and $ZnCl_2$ in the mole ratio of 1 : 2 at 380 °C for 48 h in the Ar atmosphere. In addition, zinc chloride melts at the temperature of $T_m \simeq 290$ °C meaning that the ionic exchange above this temperature occurs between solid and liquid phases improving the mixing of the reactants. The topotactic reaction can be expressed as

$$\beta\text{-}Li_2IrO_3 + xZnCl_2 \xrightarrow{Ar} \beta\text{-}\mathbf{ZnIrO_3} + (x-1)ZnCl_2 + 2LiCl. \qquad (3.2)$$

The residual $ZnCl_2$ and the byproduct LiCl were removed by treating the sample with the 10% solution of hydrochloric acid, washed several times with distilled water and dried by rinsing with acetone.

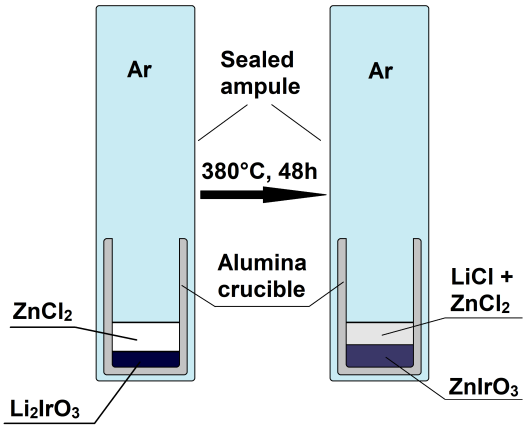

Figure 3.2: Schematic illustration of the ionic exchange setup on the example of the β-$ZnIrO_3$ synthesis.

β-$MgIrO_3$ Assuming similarity in the chemical substitution [138], synthesis of β-$MgIrO_3$ was attempted to synthesis at the exactly the same conditions as for β-$ZnIrO_3$ using $MgCl_2$ ($\geq$ 99.99%, ChemPUR) as a reactant. Surprisingly, no signs of substitution were found in this case; varying the reaction conditions didn't facilitate the ionic exchange as well. The reason for the unsuccessful substitution could be the low chemical activity of magnesium chloride particularly in this situation. As a workaround, one could think about another magnesium salt, especially, with a low melting temperature. For instance, magnesium nitrate hexahydrate with the formula of $Mg(NO_3)_2{\cdot}6H_2O$ (99.97%, Alfa Aesar) may be a good candidate as a reactant for the ionic exchange. Unlike other chlorides used, this salt is stable in air and has a very low melting point of $T_m \sim 90$ °C [143]. Therefore, the well ground mixture of β-Li_2IrO_3 and $Mg(NO_3)_2{\cdot}6H_2O$ in the mole ratio of 1 : 3 was placed into an alumina crucible and heated at 310 °C for 24 h directly in air. The increasing of synthesis temperature is not possible due to decomposition of magnesium nitrate above $T_{dec} \simeq 330$ °C [143]. Increasing the duration of the synthesis as well as re-annealing of β-$MgIrO_3$ samples at higher temperatures (up to 500 °C) don't affect the sample crystallinity/quality. The summarized reaction can be expressed as

$$\begin{aligned}&\beta\text{-}Li_2IrO_3 + x Mg(NO_3)_2 \cdot 6H_2O \xrightarrow{air}\\ &\beta\text{-}\mathbf{MgIrO_3} + (x-1)Mg(NO_3)_2 + 2LiNO_3 + x6H_2O.\end{aligned} \tag{3.3}$$

Byproducts of the reaction were removed by the same procedure as the previously synthesized β-$ZnIrO_3$ with hydrochloric acid solution, distilled water and acetone.

$Li_{2x}Mg_{1-x}IrO_3$ Partial substitution in the honeycomb sodium and lithium iridates was briefly discussed earlier in the corresponding section. And divalent metals were not suggested as doping elements for the layered systems. For the case of 3D structure of β-Li_2IrO_3, it also seemed unlikely because of the robust nature of the hyperhoneycomb lattice and difference in the ion charges of Li^+ and M^{2+} that could lead to a change in the oxidation state of iridium. Nevertheless, partial substitution of Li in β-polymorph is possible.

Systematic variation of synthesis conditions for β-$MgIrO_3$, namely the molar ratio of reagents, revealed that equivalent amounts of the parent compound and magnesium nitrate without an excess of the latter reacted with the formation of a new phase with the similar crystal structure, but the lattice constants differ from the cell parameters of β-$MgIrO_3$. Decreasing the fraction of $Mg(NO_3)_2{\cdot}6H_2O$ in the molar ratio led to contradictory results: samples showed a change in the lattice parameters but without any connection to the initial molar ratio of the reactants. Initially, the solid solution $Li_{2x}Mg_{1-x}IrO_3$ was suggested, and a lot of effort was put into the selection of synthesis conditions. However, only the tiny range or even one point of substitution level x demonstrated more or less reproducible results.

Eventually, the new partially substituted iridate β-$Li_{2x}Mg_{1-x}IrO_3$ with $x = 0.3$ or $Li_{0.6}Mg_{0.7}IrO_3$ [further, β-(Li,Mg)IrO_3 for short] was synthesized by topotactic ion exchange reaction from the mixture of β-Li_2IrO_3 and $Mg(NO_3)_2{\cdot}6H_2O$ in the molar ratio of $1 : 0.8$. The reaction conditions and subsequent treatments were identical to the synthesis for fully substituted β-$MgIrO_3$. One crucial remark is that the reproducibility of the synthesis strongly depends on the sample amount: for instance, the minimal mass of β-Li_2IrO_3 was at least 2 grams.

The new synthesized Kitaev iridates – β-$ZnIrO_3$, β-$MgIrO_3$, and β-(Li,Mg)IrO_3 – are all dark-grey or even black polycrystalline samples, stable in the air, difficult to press into pellets. No degradation in air was observed after 12 months. In contrast to the partially substituted β-(Li,Mg)IrO_3, β-$ZnIrO_3$ and β-$MgIrO_3$ samples can be prepared in a wide range of masses varying between 0.3 g and $\sim$ 1 g.

Table 3.2: Summary of synthesis conditions for the chemical substitution. *MNH* stands for magnesium nitrate hexahydrate $Mg(NO_3)_2{\cdot}6H_2O$. The asterisk denotes the composition $Li_{0.6}Mg_{0.7}IrO_3$

Reactant	Ratio	T (°C)	Atmosphere	Duration (h)	Result
CuCl	1 : 3	380 – 440	*Ar*	16 – 80	Degradation of β-Li_2IrO_3
AgCl $AgNO_3$	up to 1 : 3	350 – 380	*Ar*	16 – 48	No reaction
$ZnCl_2$	up to 1 : 3	350 – 380	*Ar*	16 – 48	β-$ZnIrO_3$
$MgCl_2$	1 : 2	350 – 400	*Ar*	16 – 48	No reaction
MNH	1 : 3	290 – 320	air	24 – 48	β-$MgIrO_3$
MNH	1 : 0.8	310	air	24	β-(Li,Mg)IrO_3*

3.2 Crystal structure

3.2.1 Methods of structural characterization

Preliminary sample characterization was performed by powder x-ray diffraction (PXRD) using laboratory diffractometer Rigaku MiniFlex 600 with CuKα radiation and work performance of 40 kV and 15 mA. Microstructure, space group and elemental analysis of β-$M$$IrO_3$ were performed by the transmission electron microscopy (TEM) and the energy dispersive x-ray spectrometry (EDX) methods. Further structural characterization of the samples was carried out by high-resolution PXRD and neutron powder diffraction with the Rietveld refinement of the crystal structure. The Jana2006 program [144] was used for the structure refinement. The experimental details and conditions are described below.

Electron microscopy. TEM investigation of the samples was performed by Maria Kirsanova and Artem Abakumov at Skolkovo Institute of Science and Technology (Moscow, Russia). The samples were prepared in air by crushing the crystals in a mortar in acetone and depositing drops of suspension onto holey carbon grids. Electron diffraction tomography (EDT) series and energy dispersive x-ray (EDX) spectra were collected manually with FEI Tecnai G2 transmission electron microscope operated at 200 kV. The selected area electron diffraction (SAED) patterns and high-resolution HAADF-STEM images were taken on aberration-corrected Titan G3 microscopes operated at 300 or 200 kV. EDT data were treated using PETS [145] and Jana2006 software [144].

Synchrotron XRD. High-resolution XRD data were collected at several temperatures between 10 and 500 K at the ID22 beamline of the European

Synchrotron Radiation Facility (ESRF; Grenoble) using the wavelength of 0.3542 Å, and the MSPD beamline of the ALBA synchrotron (Barcelona, Spain) using the wavelength of 0.3252 Å. The β-MIrO$_3$ samples were placed in thin-walled glass capillaries and cooled down using the He-flow cryostat. The capillaries were spun during the data collection. Diffracted signal was recorded by 14 (ALBA) and 13 (ESRF) scintillation detectors preceded by Si(111) analyzer crystals.

Powder neutron diffraction. Neutron diffraction data were collected at the D2B ($\lambda = 1.594$ Å) instrument at the Institut Laue-Langevin (ILL), Grenoble. The powder samples of β-MIrO$_3$ were loaded into a vanadium container and cooled down to 1.5 K with the standard Orange cryostat. All samples were measured at room temperature and 1.5 K except the partially substituted β-(Li,Mg)IrO$_3$ which was cooled down only to 20 K.

3.2.2 Details of the crystal structure

Crystal structures of new Kitaev iridates β-MIrO$_3$ bear both similarities and differences compared with the parent structure. First, the main common feature of the β-Li$_2$IrO$_3$ derivatives should be emphasized – preservation of the IrO$_6$ octahedra motif arranged on the hyperhoneycomb lattice as in the case of the parent β-Li$_2$IrO$_3$ structure. However, non-isovalent substitution of lithium atoms triggers symmetry lowering because two monovalent Li$^+$ ions have to be replaced by one divalent M^{2+} ion in order to keep the oxidation state of Ir at 4+. The latter can be shown by the charge balance trough the oxidation states of the ions in the parent and new compounds:

$$2\mathrm{Li}^{(+)} + \mathrm{Ir}^{(4+)} + 3\mathrm{O}^{(2-)} = \mathrm{Li_2IrO_3^{(0)}}$$
$$\mathrm{M}^{(2+)} + \mathrm{Ir}^{(4+)} + 3\mathrm{O}^{(2-)} = \mathrm{MIrO_3^{(0)}}$$

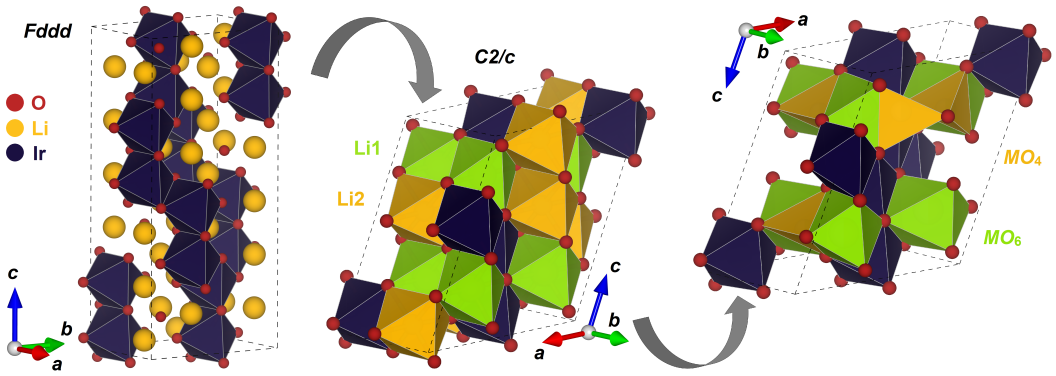

Figure 3.3: Visualization of the unit cell transformation of the orthorombic $Fddd$ space group into the monoclinic $C2/c$ ($P2_1/c$) one by symmetry lowering. The hyperhoneycomb motif of IrO$_6$ octahedra is presented in dark blue. The corresponding octahedral and tetrahedral positions are colored in green and yellow, respectively.

Figure 3.3 schematically illustrates the connection between an original structure of the parent compound and its transformation into the new monoclinic representations.

β-Li_2IrO_3 crystallizes in the orthorhombic space group $Fddd$ (#70) with one position of Ir forming the hyperhoneycmb sublattice, and two non equivalent positions of Li1 and Li2 that occupy two octahedral sites, 16 in total for one unit cell. Converting the orthorombic crystal system into the monoclinic one can be done by the transformation matrix $L_1(\mathbf{P}, p)$ or $L_2(\mathbf{P}, p)$ leading to the monoclinic space groups $C2/c$ (#15) or $P2_1/c$ (#14), respectively. In this definition, $\mathbf{P}$ represents the 3×3 rotation matrix, and p displays the origin shift.

$$L_1(\mathbf{P},p) = \begin{pmatrix} 0 & 1 & 0 & 0 \\ -1 & 0 & \frac{1}{2} & 0 \\ 0 & 0 & \frac{1}{2} & 0 \end{pmatrix}; \quad L_2(\mathbf{P},p) = \begin{pmatrix} 0 & 1 & 0 & \frac{1}{4} \\ -1 & 0 & \frac{1}{2} & \frac{1}{4} \\ 0 & 0 & \frac{1}{2} & 0 \end{pmatrix}.$$

New β-$M$$IrO_3$ compounds crystallize in one of these two monoclinic modifications in which Ir atoms form the hyperhoneycomb motif while one part of divalent M atoms occupies one of the octahedral sites previously taken by the Li atoms in the parent compound, and the remaining M^{2+} ions go into tetrahedral sites that have been empty before substitution.

β-$ZnIrO_3$ The crystal structure of zinc iridate is solved in the space group $P2_1/c$ which can be obtained from the initial $Fddd$ space group of the parent compound by the transformation matrix $L_2(\mathbf{P}, p)$. Edge-sharing IrO_6 octahedra form 3D framework with two types of cavities occupied by Zn atoms (Fig. 3.4 a). The first type is an octahedral position Zn1 similar to the previous site Li1 in the parent compound, and the second one is a new tetrahedral

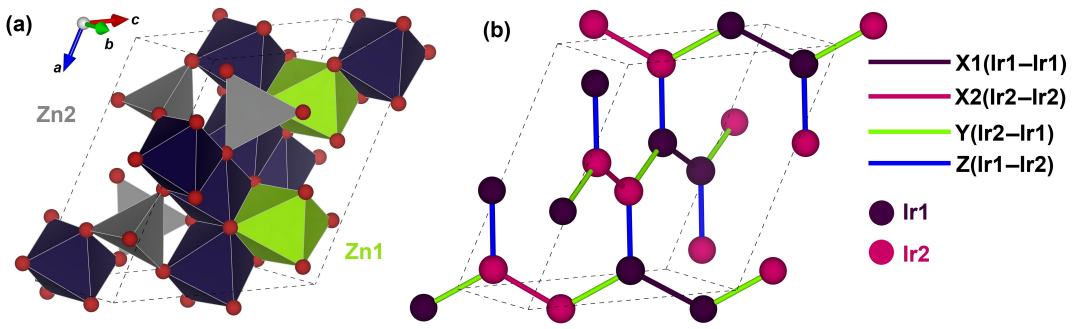

Figure 3.4: (a) Crystal structure of β-$ZnIrO_3$; the octahedral (Zn1) and tetrahedral (Zn2) positions are represented in green and gray, respectively. (b) Hyperhoneycomb Ir^{4+} network with the $X(X1, X2)$-, Y-, and Z-bonds labeled similar to the β-Li_2IrO_3 notation.

Table 3.3: Structural parameters of β-$ZnIrO_3$ from the Rietveld refinement of the neutron diffraction data. The space group is $P2_1/c$ (#14) and $Z = 8$, the lattice constants are $a = 8.7637(2)$ Å, $b = 5.9209(1)$ Å, $c = 9.9227(3)$ Å, $\beta = 116.12(1)$ deg. and $V = 57.79$ Å^3/f.u. at $T = 300$ K. Site occupancy is 1 for all atoms; U_{iso} is the isotropic displacement parameter and is given in Å^2.

Atom	Site	x	y	z	U_{iso}
Ir1	4e	0.3250(12)	0.122(3)	0.4167(7)	0.0013(5)
Ir2	4e	0.1594(11)	0.128(3)	0.0804(7)	
Zn1	4e	0.5065(14)	0.383(3)	0.2806(9)	0.0004(9)
Zn2	4e	0.1211(11)	0.622(4)	0.2519(15)	
O1	4e	0.0725(16)	0.607(3)	0.4221(13)	0.0001
O2	4e	0.1094(17)	0.126(3)	0.4329(12)	
O3	4e	0.3969(18)	0.148(3)	0.0920(13)	
O4	4e	0.5593(18)	0.112(3)	0.4149(13)	
O5	4e	0.7452(14)	0.393(4)	0.2589(12)	
O6	4e	0.2549(15)	0.355(4)	0.2537(13)	

position Zn2. Both sites are fully occupied by Zn atoms, however, the number of the positions is reduced to 8 (4 sites for each ZnO_4 and ZnO_6 structural units) due to the substitution of two Li atoms by one Zn atom.

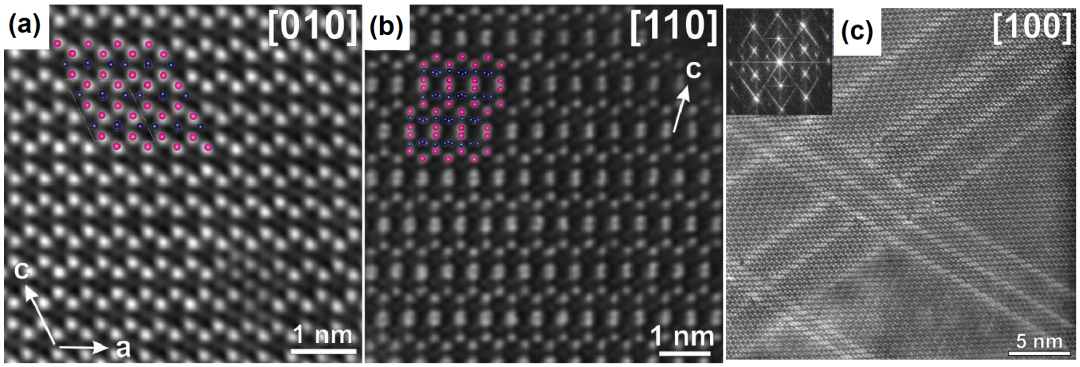

Figure 3.5: (a) [010] and (b) [110] projections of the structural model of β-$ZnIrO_3$ superimposed on the experimental HAADF-STEM images. Ir and Zn atoms are shown as purple and blue balls, respectively. O atoms are not shown. (c) [100] HAADF-STEM images of β-$ZnIrO_3$ illustrating {013}-confined planar defects in the honeycomb packing.

Moreover, the structural model of β-$ZnIrO_3$ adopts two distinguishable Ir sites – Ir1 and Ir2 – forming four independent Ir–Ir pairs (Table 3.3), while in the parent compound β-Li_2IrO_3 only one position of Ir is allowed with two types of Ir–Ir bonds. In the case of β-$ZnIrO_3$, the XYZ-bond notation of the Kitaev model (Fig. 3.4 b) can be applied as follows: three pairs of Ir1–Ir1, Ir2–Ir2 and Ir2–Ir1 bonds labeled as $X1$, $X2$ and Y, respectively, form

zigzag chains alternating along the c direction, and Ir1–Ir2 pair noted as Z bond binds the iridium chains. The full information about crystal structure refinement and structural parameters can be found in the Appendix A.

The synchrotron PXRD data (Fig. 3.8a) indicate an almost pure phase of β-$ZnIrO_3$ except several low-intensity peaks that can't be identified as any known compound, *e.g.* Ir, IrO_2, α-$ZnIrO_3$ or β-Li_2IrO_3. The β-$ZnIrO_3$ composition is confirmed by EDX and by the crystal structure refinement based on neutron diffraction data that are sensitive to both light Zn and O as well as heavy Ir atoms. Figure 3.5a-b demonstrates the perfect honeycomb packing of the Ir atoms with the average Ir–Ir bond distance of $\sim$ 3.02 Å that is slightly longer than in the parent compound with the average bond length of $\sim$ 2.97 Å [97]. However, the Ir–O bond distances calculated from the neutron data refinements at room temperature and 1.5 K, are slightly anisotropic indicating that IrO_6 octahedra are somewhat distorted (see Table 3.4). The bond length distortion (BLD) and the edge length distortion (ELD) parameters can be employed to quantify the degree of IrO_6 distortion which are defined as [146]

$$\mathrm{BLD}(\%) = \frac{100}{n}\sum_{i}^{n}\frac{|d_i - \langle d\rangle|}{\langle d\rangle}; \quad \mathrm{ELD}(\%) = \frac{100}{n}\sum_{i}^{n}\frac{|OO_i - \langle OO\rangle|}{\langle OO\rangle} \tag{3.4}$$

where d (OO_i) is the bond (edge) length of the polyhedron and $\langle d\rangle$ ($\langle OO\rangle$) is the average bond (edge) length. The BLD values calculated for both Ir1 and Ir2 sites are around 1.63% and 1.16%, respectively, and the ELD values are roughly around 3.5%. In comparison with the parent compound β-Li_2IrO_3, the BLD of IrO_6 octahedra is less than 0.04% with the average Ir–O bond distance of 2.025 Å [97].

Table 3.4: Ir–O bond distances at RT and 1.5 K (base temperature, BT) for the Ir1 and Ir2 positions of β-$ZnIrO_3$ obtained from the Rietveld refinement of the neutron diffraction data.

Type	d^{RT}_{Ir-O} (Å)	d^{BT}_{Ir-O} (Å)	Type	d^{BT}_{Ir-O} (Å)	d^{BT}_{Ir-O} (Å)
Ir1–O2	1.97(2)	2.01(2)	Ir2–O1	2.02(2)	2.01(2)
Ir1–O3	2.08(2)	2.055(19)	Ir2–O1	1.99(2)	2.00(2)
Ir1–O4	2.05(2)	2.02(2)	Ir2–O2	1.97(2)	2.01(2)
Ir1–O4	2.06(2)	2.04(2)	Ir2–O3	2.04(2)	2.07(2)
Ir1–O5	2.07(2)	2.06(3)	Ir2–O5	2.00(2)	2.00(3)
Ir1–O6	2.01(2)	2.01(3)	Ir2–O6	2.04(2)	2.04(3)

Additionally, some crystallites of β-$ZnIrO_3$ have planar defects confined to the {013} lattice planes of the parent *Fddd* subcell (Fig. 3.5c). The projected Ir–Ir distance within the defects is drastically shortened to $\sim$ 2.15 Å that might indicate changing of connectivity of the IrO_6 octahedra from edge-sharing to face-sharing along the defect and formation of thin slabs of the rock-salt type structure. Such defects may be a result of ionic exchange or

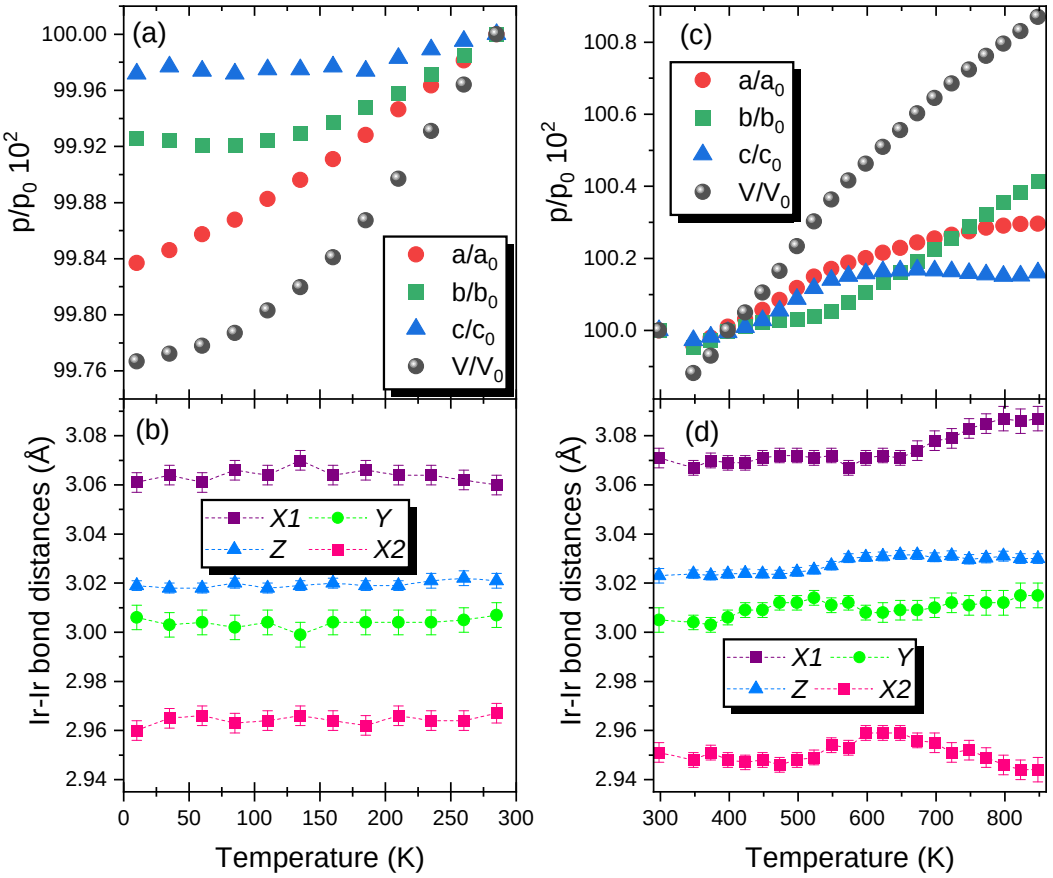

Figure 3.6: (a), (c) Lattice parameters and unit cell volume, and (b), (d) Ir–Ir bond distances of β-$ZnIrO_3$ as a function of temperature below and above room temperature, respectively. All lattice constants are normalized to the parameters at RT. The values of the monoclinic angle β are not given due to a change of less than 0.05 °.

inherited from the parent compound. Nevertheless, these defects are rare and may not affect magnetic properties and can be ignored.

Temperature evolution of the lattice constants as well as Ir–Ir bond distances plotted from the Rietveld refinement of the synchrotron PXRD data (Fig. 3.6a-b) do not demonstrate any drastic changes: the unit cell parameters steadily decrease with temperature while the lengths of the XYZ-bonds slightly fluctuate around their mean values. On the other hand, changes of the lattice constants upon warming deviate from the linear behavior above 550 K ($\sim$ 250 °C) that's also seen from the remarkable deviations in the Ir–Ir bond distances (Fig. 3.6c-d). However, no structural transformations and change of the space group $P2_1/c$ were detected by the crystal structure refinement at least up to 550 °C.

The Ir–O–Ir bond angles (Θ) calculated from the refinement of neutron diffraction data are strongly anisotropic and consistent with the changes of XYZ-bond distances (Table 3.5). Such diversity in bond length and angles values is caused, first of all, by a non-equivalent surrounding of oxygen atoms that are shared additionally between different types of Zn polyhedra.

For instance, along the longest *X1* bond the position O4 in the Ir1–O4–Ir1 angle is involved with two ZnO_6 octahedra, and along the *X2* bond the position O1 in the Ir2–O1–Ir2 angle is shared with only one ZnO_4 tetrahedron. Along the other *Y*- and *Z*-bonds the oxygen atoms are connected non uniformly with both tetrahedral and octahedral Zn positions. Additionally, the anisotropic nature of the bonds are affected by highly distorted of ZnO_6 and ZnO_4 units with the BLD values of 4.2% and 2.03%, respectively.

Table 3.5: Ir–Ir bond distances and Ir–O–Ir bond angles of β-$ZnIrO_3$ at RT and 1.5 K (BT) obtained from the Rietveld refinement of the neutron diffraction data.

Bond direction	d^{RT}_{Ir-Ir} (Å)	d^{BT}_{Ir-Ir} (Å)	Angles	Θ^{RT} (deg)	Θ^{BT} (deg)
intrachain X1	3.116(16)	3.087(17)	Ir1–O4–Ir1	98.6(9)	99.3(10)
intrachain X2	2.954(15)	2.930(17)	Ir2–O1–Ir2	94.9(9)	93.9(10)
intrachain Y	3.009(17)	3.027(19)	Ir1–O2–Ir2	99.3(8)	98.0(9)
			Ir1–O3–Ir2	93.8(7)	94.5(7)
between chains Z	2.994(9)	2.995(10)	Ir1–O5–Ir2	94.6(12)	95.0(14)
			Ir1–O6–Ir2	95.2(12)	95.3(14)

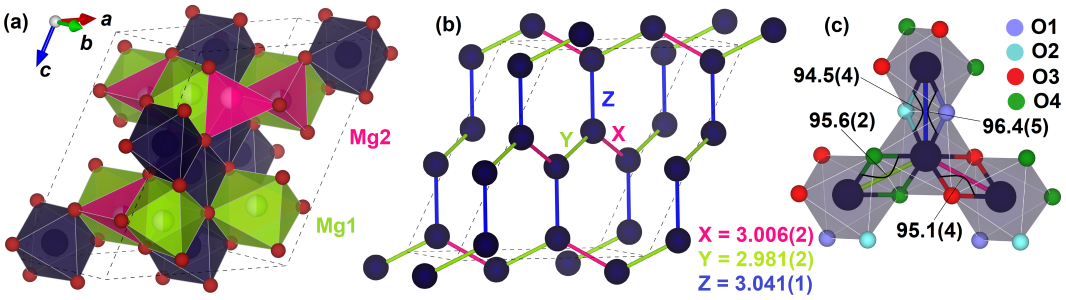

Figure 3.7: (a) Crystal structure of β-$MgIrO_3$. (b) Hyperhoneycomb lattice of Ir atoms in β-$MgIrO_3$ with the corresponding bond labeling. (c) Local lattice network of IrO_6 octahedra in β-$MgIrO_3$, displaying Ir–O–Ir bond angles and three different Ir–Ir bond distances.

β-$MgIrO_3$ Room-temperature crystal structure of β-$MgIrO_3$ is solved in the space group $C2/c$. The symmetry lowering doesn't disturb the hyperhoneycomb motif of IrO_6 framework (Fig. 3.9a-b), but triggers a disorder of the Mg sites in contrast to the well-ordered β-$ZnIrO_3$. However, now Mg^{2+} ions occupy all octahedral positions Mg1 as Li1 sites in β-Li_2IrO_3 and all tetrahedral sites Mg2 giving 16 positions of Mg atoms in total, but only with a partial filling (Fig. 3.7a). The distribution of Mg over the octahedral and tetrahedral sites obtained from the crystal structure refinement based on neutron diffraction data is nearly equal, with the occupancies of 48.4(5)% and 51.6(5)%, respectively (Table 3.6). The structural model of β-$MgIrO_3$ adopts only one position of Ir atoms and three distinct types of Ir–Ir bonds which can again

be denoted in terms of the Kitaev model. X- and Y-bonds form zigzag chains connected by the bridging Z-bond (Fig. 3.7b).

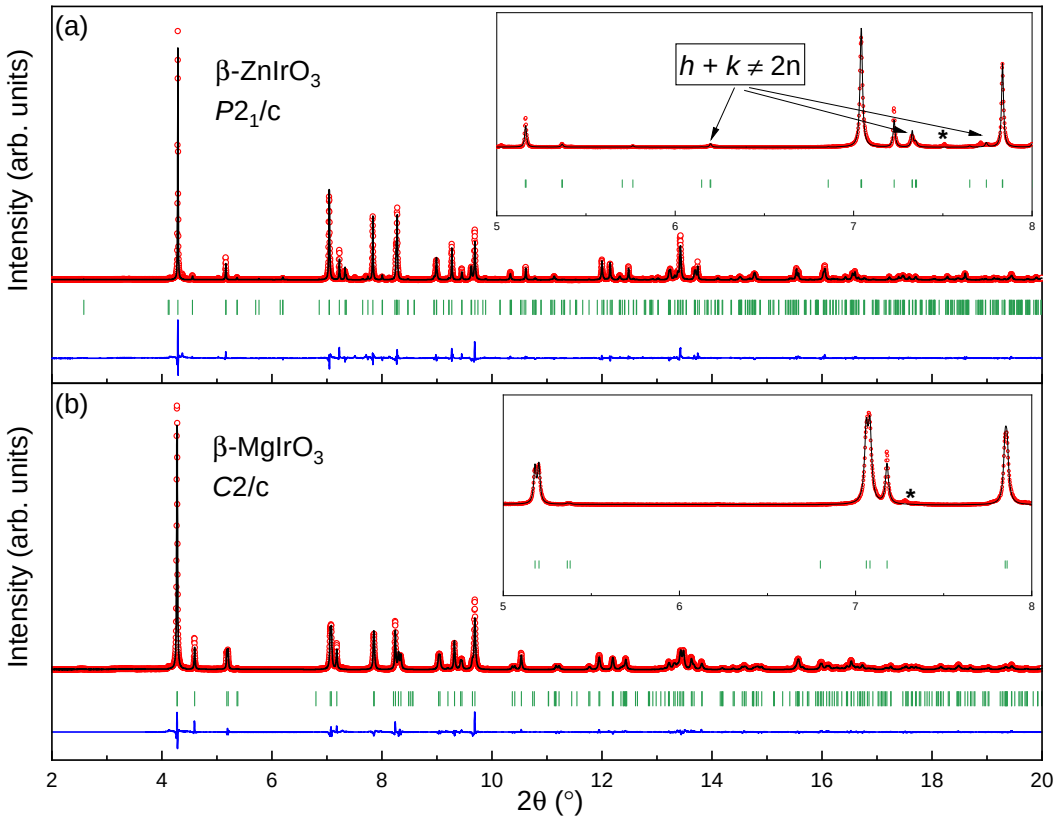

Figure 3.8: Rietveld refinements versus high-resolution XRD data of β-$ZnIrO_3$ (a) and β-$MgIrO_3$ (b) measured at room temperature. Vertical bars indicate the positions of Bragg reflections. Asterisks indicate unknown impurities. The refinement residuals are $R_p = 0.115$, $wR_p = 0.159$ and GoF $= 2.91$ for the β-$ZnIrO_3$ and $R_p = 0.083$, $wR_p = 0.110$ and GoF $= 2.52$ for the β-$MgIrO_3$. The insets show a zoomed region where P-reflections are visible in case of β-$ZnIrO_3$, and absent in case of β-$MgIrO_3$ due to C-centering.

Phase analysis of the synchrotron PXRD data indicates the absence of any impurity phases, but a couple of low-intensity reflections remained undescribed (Fig. 3.8 b). EDX analysis of β-$MgIrO_3$ samples demonstrates the Mg : Ir $= 1.04(8) : 0.96(8)$ atomic ratio confirming the stated composition. The choice of the C-centered space group, as opposed to the primitive one, was verified by electron microscopy experiments: as the EDT technique allows for significant suppression of multiple electron scattering, the reflection conditions were clearly observed in the EDT reciprocal lattice sections. The $h + k = 2n$ condition is fulfilled for all hkl reflections, confirming C-centering, whereas the $h0l, h, l = 2n$, $00l, l = 2n$ reflection conditions unequivocally suggest the $C2/c$ (#15) space group. Moreover, the presence of two distinguishable Mg positions in the structure can be suggested from the analysis of the HAADF signal profile of some well oriented [010] images (Fig. 3.9c). Two types of the minor intensity peaks – sharp well-resolved and

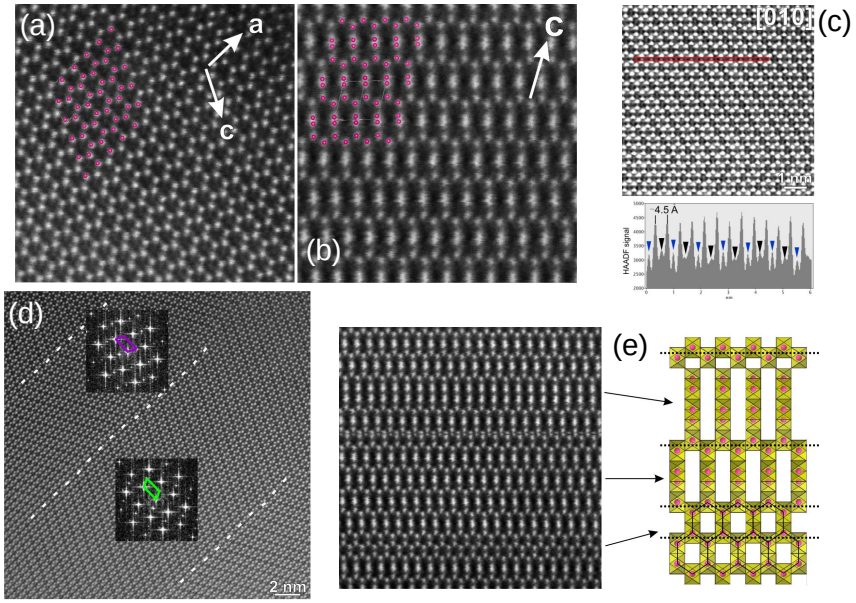

Figure 3.9: (a) [010] and (b) [110] projections of the model unit cell superimposed on the experimental HAADF-STEM image of β-$MgIrO_3$. Only Ir atoms are shown. (b) Fourier-filtered [010] HAADF-STEM image of β-$MgIrO_3$. The intensity profile along the Ir honeycomb packing (red rectangular) shows the presence of two types of peaks between Ir atoms, probably corresponding to two types of the Mg columns. (d) [010] HAADF-STEM image of the mirror-twin crystal of β-$MgIrO_3$. The FFT images taken from different areas of the crystallite are shown as insets. The unit cells for each area are shown with violet and green colors. The twin planes are marked with white dashed lines. (e) [110] HAADF-STEM image of β-$MgIrO_3$ and schematic illustration of the formation of antiphase bondaries (shown with black dash lines).

weak pronounced satellites – correspond to the different types of Mg positions; the difference in the peak intensity suggests the partial occupancy of these sites. Minor defects of the crystal structure visualized by electron microscopy (Fig. 3.9d)) were found in the samples. The different areas of the crystallite were mirror-twinned in some seeds. Additionally, some of the crystallites also demonstrated stacking disorder on the [110] HAADF-STEM images, related to formation of randomly located antiphase boundaries (APBs) normal to the c axis (Fig. 3.9e)).

At room temperature, the crystal structure of β-$MgIrO_3$ retains the perfect honeycomb packing of Ir atoms with Ir–Ir distance of 3.00(2) Å without a pronounced anisotropy in the bond directions as well as in the values of Ir–O–Ir bond angles (Fig. 3.7). The IrO_6 octahedra are marginally distorted with the BLD of 1.15% and the ELD of 3.4% that is comparable with the values of these parameters for β-$ZnIrO_3$. The random distribution of Mg atoms between the tetrahedral and octahedral positions may conceal the distortions by averaging the Ir–Ir bond length distances and the angles Θ.

Upon warming above room temperature, the unit cell parameters of β-$MgIrO_3$ increase linearly with temperature at least up to 500 K ($\sim$ 200 °C)

Table 3.6: Structural parameters of β-$MgIrO_3$ from the Rietveld refinement of the neutron diffraction data. The space group is $C2/c$ (#15) and $Z = 8$, the lattice constants are $a = 8.7238(2)$ Å, $b = 5.9737(1)$ Å, $c = 9.8320(2)$ Å, $\beta = 115.99(1)$ deg. and $V = 57.57$ Å^3/f.u. at $T = 300$ K. g and U_{iso} denote site occupancy and the isotropic displacement parameter in Å^2, respectively.

Atom	Site	x	y	z	g	U_{iso}
Ir	$8f$	0.9166(7)	0.8713(9)	0.0802(4)	1	0.0030(5)
Mg1	$8f$	0.7370(18)	0.139(3)	0.2285(10)	0.489(5)	0
Mg2	$8f$	0.6326(10)	0.878(3)	0.2547(14)	0.511(5)	
O1	$4e$	0	0.645(2)	0.25	1	0.0036(5)
O2	$4e$	0.5	0.602(2)	0.25		
O3	$8f$	0.6889(7)	0.8713(13)	0.0841(6)		
O4	$8f$	0.6515(8)	0.3990(12)	0.0861(6)		

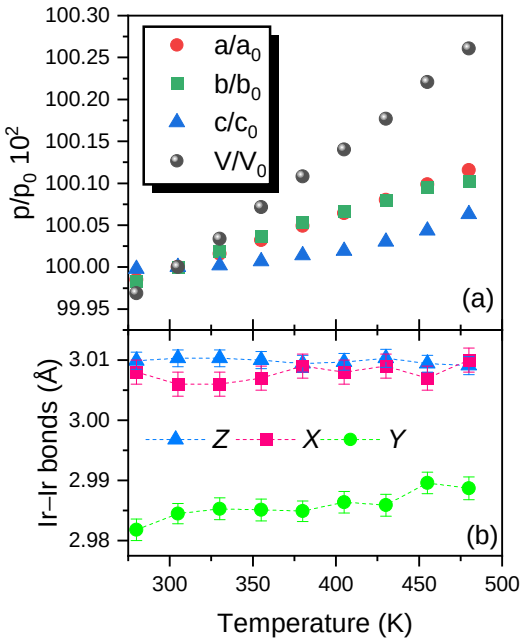

Figure 3.10: Temperature evolution of the lattice parameters and unit cell volume (a), and Ir–Ir bond distances (b) of β-$MgIrO_3$ upon warming above 300 K. All lattice constants are normalized to their values at RT. The values of the monoclinic angle β are not given due to a change of less than 0.05 °.

without a transition into a higher symmetric space group; the Ir–Ir bond distances do not change significantly as well (Fig. 3.10). However, the most unexpected feature of β-$MgIrO_3$ is the first-order phase transition upon cooling accompanied by partial magnetism collapse due to dimerization of one of the Ir–Ir bonds. Later, dimerization transition in β-$MgIrO_3$ will be described in detail in the corresponding section 3.2.3).

β-(Li,Mg)IrO_3 Preliminary, it was suggested that β-$Li_{2x}Mg_{1-x}IrO_3$ crystallized in the same $C2/c$ space group as the fully substituted compound β-$MgIrO_3$. However, the profile refinement of the high-resolution PXRD data showed broadening or splitting of some particular reflections (inset in Fig. 3.11). As mentioned in the Section 3.1.2, different initial ratio of the reactants (β-Li_2IrO_3 and $Mg(NO_3)_2{\cdot}6H_2O$) led to a formation of the final product with the uncontrolled degree of substitution. On the other hand, the lattice parameters for two selected initial ratios clearly show a decrease in all directions with reduction of the Mg doping (Table 3.7). Therefore, as synthesis of β-$Li_{2x}Mg_{1-x}IrO_3$ with $x \simeq 0.3$ demonstrates reproducible results, further study of the partially substituted magnesium iridate was focused on the samples with the composition $Li_{0.6}Mg_{0.7}IrO_3$ (ratio 1 : 0.8) [β-(Li,Mg)IrO_3 for short].

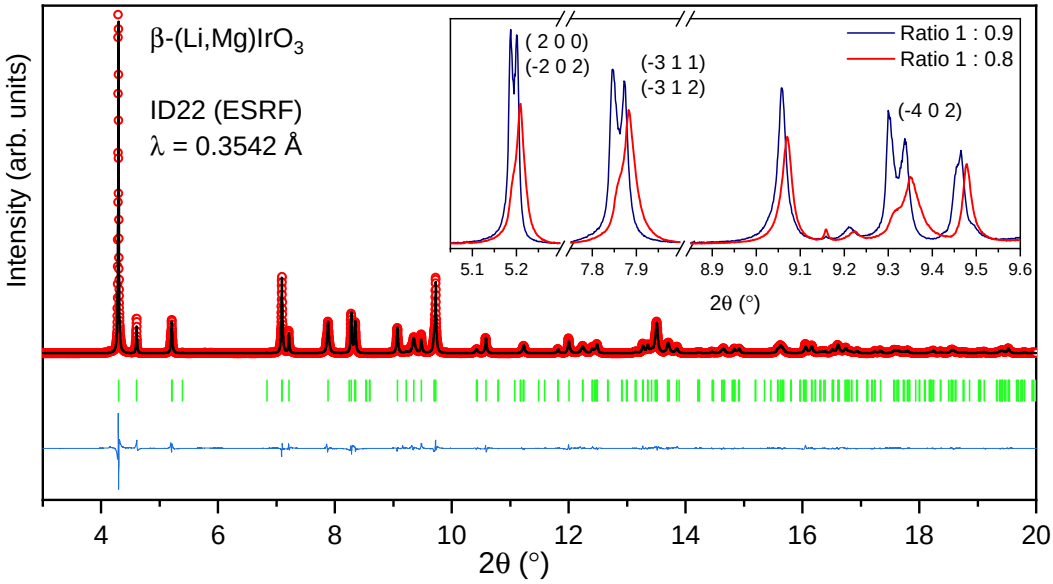

Figure 3.11: Rietveld refinement versus high-resolution XRD data of β-(Li,Mg)IrO_3 (initial composition 1 : 0.8) at room temperature. The tick marks show reflection positions for the $C2/c$ structure. The refinement residuals are $R_p = 0.083$, $wR_p = 0.113$ and GoF $= 4.82$. The inset shows a comparison of zoomed XRD profiles between two β-$Li_{2x}Mg_{1-x}IrO_3$ phases synthesized with different composition ratio. Broadened/splitted reflections are labeled in brackets.

The attempts to refine the structure in the different monoclinic symmetry groups ($C2/m$ or $P2_1/c$) didn't improve the profile matching. On the other hand, the reflection splitting/broadening might be caused by the presence of the second phase of β-(Li,Mg)IrO_3 with slightly different composition – the ratio between magnesium and lithium. The preparation of this iridate with a specified formula was quite tricky and ambiguous. Therefore, a set of phases with fluctuating composition of $Li_{0.6\pm\delta}Mg_{0.7\pm\delta}IrO_3$ could be prepared instead of single-phase compound. Unfortunately, adding the second phase with the similar lattice parameters as for β-(Li,Mg)IrO_3 led to the same unsuccessful results without improvement of the refinement. Another source of additional reflections could be a superstructure due to site separation of

Table 3.7: Comparison of the partially-substituted β-$Li_{2x}Mg_{1-x}IrO_3$ compounds synthesized with the different initial ratio of reactants – β-Li_2IrO_3 and $Mg(NO_3)_2{\cdot}6H_2O$, respectively: lattice parameters (a, b, c, β), and unit cell volume V per formula unit. The refinement was performed with suggested $C2/c$ space group.

Ratio	a (Å)	b (Å)	c (Å)	β (deg)	V (Å^3)
1 : 0.9	8.7255(2)	5.9541(1)	9.8416(1)	116.24(1)	57.32
1 : 0.8	8.6932(1)	5.9433(1)	9.8317(2)	116.30(1)	56.92

Li and Mg atoms. Nevertheless, further refinements of the x-ray (Fig. 3.11) and neutron diffraction data were done in approximation of the space group $C2/c$ to track main features of the crystal structure.

Table 3.8: Structural parameters of β-(Li,Mg)IrO_3 from the Rietveld refinement of the neutron diffraction data. The space group is $C2/c$ (#15) and $Z = 8$, the lattice constants are $a = 8.6880(3)$ Å, $b = 5.9414(2)$ Å, $c = 9.8104(4)$ Å, $\beta = 116.20(1)$ deg. and $V = 56.80$ Å^3/f.u. at $T = 300$ K. g and U_{iso} denote site occupancy and the isotropic displacement parameter in Å^2, respectively.

Atom	Site	x	y	z	g	U_{iso}
Ir	$8f$	0.9178(7)	0.8778(14)	0.0811(4)	1	0.0053(6)
Mg1	$8f$	0.727(5)	0.126(8)	0.227(2)	0.427(6)	0
Li1					0.538	
Mg2	$8f$	0.628(2)	0.869(7)	0.239(3)	0.263(6)	0
Li2					0.082	
O1	$4e$	0	0.647(3)	0.25	1	0.0006(5)
O2	$4e$	0.5	0.605(2)	0.25		
O3	$8f$	0.6896(9)	0.8682(18)	0.0764(9)		
O4	$8f$	0.6556(7)	0.3962(15)	0.0854(7)		

Assuming the structural model of magnesium iridate, the partially substituted β-(Li,Mg)IrO_3 adopts the hyperhoneycomb motif of IrO_6 octahedra as well as disordered tetrahedral and octahedral positions both occupied by Mg and Li atoms. The crystal structure and XYZ-bond notation of the Ir–Ir pairs can be illustrated by the same Fig. 3.7a-b as for the structure of β-$MgIrO_3$. EDX analysis of the β-(Li,Mg)IrO_3 sample demonstrates the $Mg/Ir = 0.69(2)$ atomic ratio suggesting that $x \sim 0.3$ in $Li_{2x}Mg_{1-x}IrO_3$ (initial composition 1 : 0.8). The following composition $Li_{0.6}Mg_{0.7}IrO_3$ was used to refine the neutron diffraction data, particularly, to estimate the distribution of Li and Mg atoms between their positions. Thus, Mg and Li atoms mostly occupy the

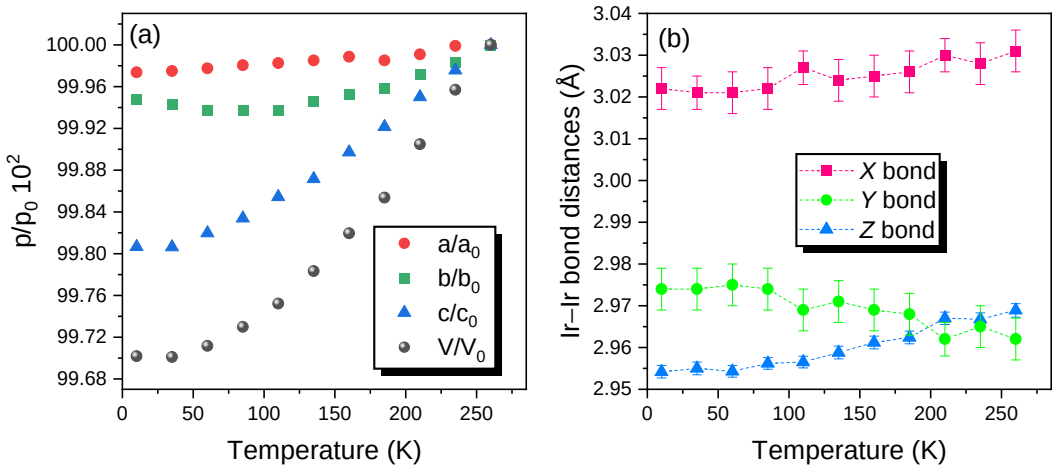

Figure 3.12: (a) Temperature dependence of the unit cell constants of β-(Li,Mg)IrO_3 and (b) XYZ-bond distances. The values of the monoclinic angle β are not given due to a change of less than 0.03 °.

octahedral site Mg1/Li1 with the fraction of 62.8(9)% and 86.8(9)%, respectively, while the tetrahedral position Mg2/Li2 is significantly depopulated, with the Mg occupancy of 37.2(9)% and only 13.2(9)% of Li atoms (Table 3.8).

Temperature dependence of the cell constants of β-(Li,Mg)IrO_3 demonstrates minor reduction of the a and b parameters, and faster decrease along the c direction that could be correlated with the evolution of Ir–Ir bond distances. The mentioned non-uniform distribution of substituted metals manifests itself in an anisotropic behavior of the XYZ-bonds upon cooling: the X-bonds are lengthened comparing with the shortened Y- and Z-bonds. Further reduction of the last one corresponds to a more pronounced decrease of the c lattice parameter along which the Z-bonds are located (Fig. 3.12).

Table 3.9: Ir–Ir bond distances and Ir–O–Ir bond angles of β-$Li_{0.6}Mg_{0.7}IrO_3$ at RT obtained from the Rietveld refinement of the neutron diffraction data.

Bond direction	d^{RT}_{Ir-Ir} (Å)	Angles	Θ^{RT} (deg)
intrachain X	3.064(13)	Ir–O3–Ir	98.8(8)
intrachain Y	2.929(14)	Ir–O4–Ir	93.4(7)
between chains Z	2.969(5)	Ir–O1–Ir	94.5(16)
		Ir–O2–Ir	95.8(16)

Similar anisotropic behavior can be tracked by changes of the Ir–O–Ir bond angles (Table 3.9), however, a reason of relatively small Θ angle by the Y-bonds remains unclear. The IrO_6 octahedra seem the most undistorted among other new substituted iridates with the BLD and ELD values of 0.7% and 2.97%, respectively. But it is necessary to keep in mind that the crystal structure of β-(Li,Mg)IrO_3 may be more complex than the suggested model

with the $C2/c$ space group, and partial occupancy of tetrahedral and octahedral positions strongly affects the Ir–Ir bonds and corresponding bridging angle Θ.

3.2.3 Dimerization transition in β-$MgIrO_3$

β-$MgIrO_3$ undergoes a first-order phase transition upon cooling with a structural transformation from the high-temperature (**HT**) phase into the low-temperature (**LT**) phase. This transition was monitored by synchrotron x-ray diffraction that revealed a gradual suppression of the reflections, accompanied by the growth of new peaks at nearby positions. The reverse transition could also be tracked upon warming (Fig. 3.13 and 3.14a). The **LT**-phase adopts the same $C2/c$ symmetry but slightly different lattice parameters and the reduced volume of $V_{LT} = 56.65$ Å^3/f.u. vs. $V_{HT} = 57.38$ Å^3/f.u. at 1.5 K with the small volume collapse of $\sim -1.3\%$. Detailed inspection of the crystal structure determined from x-ray and neutron data showed that the distributions of Mg atoms over the octahedral and tetrahedral sites is nearly unchanged, whereas $\frac{1}{3}$ of the Ir–Ir distances is shortened from about 3.0 Å in the **HT**-phase to 2.67 Å in the **LT**-phase along the Z-bond (Fig. 3.14b). The latter distance, which is shorter than 2.71 Å in metallic iridium, serves as a fingerprint of structural dimerization and magnetic collapse. Magnetic susceptibility of β-$MgIrO_3$ is indeed affected by this structural phase transition that will be shown later in the Chapter 4. This behavior is quite similar to Li_2IrO_3 where Ir–Ir distances of $2.6 - 2.7$ Å were detected upon magnetic collapse under pressure [113, 116, 117].

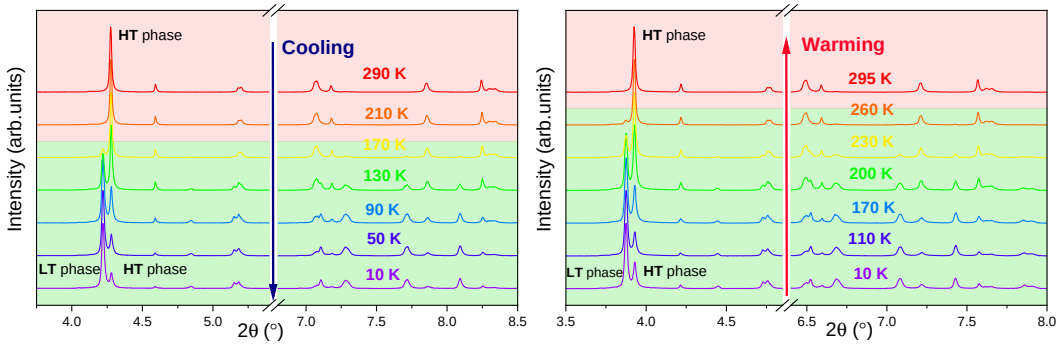

Figure 3.13: X-ray diffraction patterns of β-$MgIrO_3$ at different temperatures upon cooling (left) and warming (right) regimes.

Several distinct features of β-$MgIrO_3$ are nevertheless worth mentioning. First, the transition happens at ambient pressure upon cooling, similar to Li_2RuO_3 [147–150] and α-$MoCl_3$ [151] with $4d$ transition metals. Stronger spin-orbit coupling in the $5d$ Ir^{4+} ion is expected to stabilize the magnetic nondimerized phase [113] and eliminate magnetic collapse at ambient pressure. β-$MgIrO_3$ clearly violates this trend. Second, the transition is accompanied by an unprecedented, 200 K broad thermal hysteresis (Fig. 3.15). In contrast, the width of the thermal hysteresis upon the dimerization transition

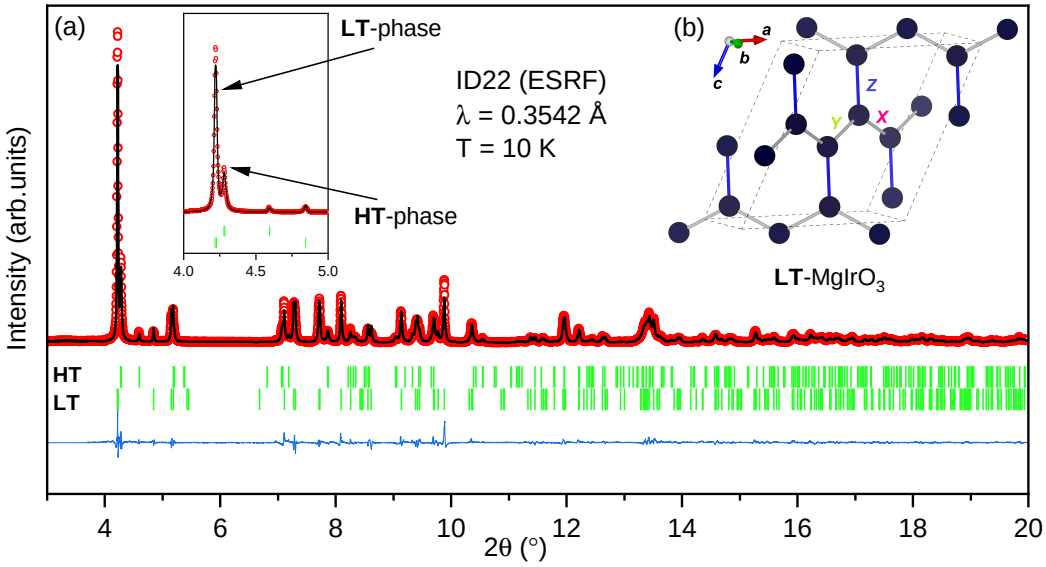

Figure 3.14: (a) Rietveld refinement versus high-resolution XRD data of β-$MgIrO_3$ at 10 K. The tick marks show reflection positions of the nondimerized **HT**-phase and dimerized **LT**-phase. The refinement residuals are $R_p = 0.086$, $wR_p = 0.113$ and GoF $= 2.14$. The inset shows a zoomed area with the most intense reflection emphasizing a coexistence of two phases at low temperatures. (b) Hyperhoneycomb network of Ir atoms in the **LT**-$MgIrO_3$ with the corresponding bond labeling. The direction of dimerization – the Z-bond – is colored in blue.

is below 10 K in Li_2RuO_3 [150] and α-$MoCl_3$ [151], and does not exceed 50 K in α-$RuCl_3$ under pressure [152].

Third, the transition is incomplete, with about 30-35% of the magnetic **HT**-phase remaining at low temperatures (Fig. 3.15a). This ratio is not affected by the cooling rate. Synchrotron experiments performed after fast (10 K/min) and slow (1 K/min) cooling revealed the same fraction of the **HT**-phase at 10 K. Yet another, and even more crucial peculiarity is that this dimerization transition is triggered by the application of negative pressure to the iridate framework: the unit cell volume of the parent compound β-Li_2IrO_3 is remarkably smaller ($V = 55.69$ Å^3/f.u. [97]) than the volumes of the **HT**- and **LT**-phase. Interestingly, the framework responds to the transition, and the Ir–Ir distances in the non-dimerized **HT**-phase also change upon cooling as the **LT**-phase is progressively formed. The changes in the two phases are in fact opposite in nature. The lattice constants of the **HT**-phase slightly decrease upon cooling, while the a and b parameters of the dimerized phase are greatly expanded by 2.1% and 1.8%, respectively, and significant contraction by $\sim -3.8\%$ along the c direction is observed (Fig. 3.15c-d). This anisotropic behavior of lattice parameters in both phases is also seen by changes of the Ir–Ir bonds. Whereas Z-bonds are shortened in the **LT**-phase, X-bonds are shortened in the **HT**-phase, albeit only by small margin, with the shortest Ir–Ir distance of 2.93 Å(Fig. 3.15e-f).

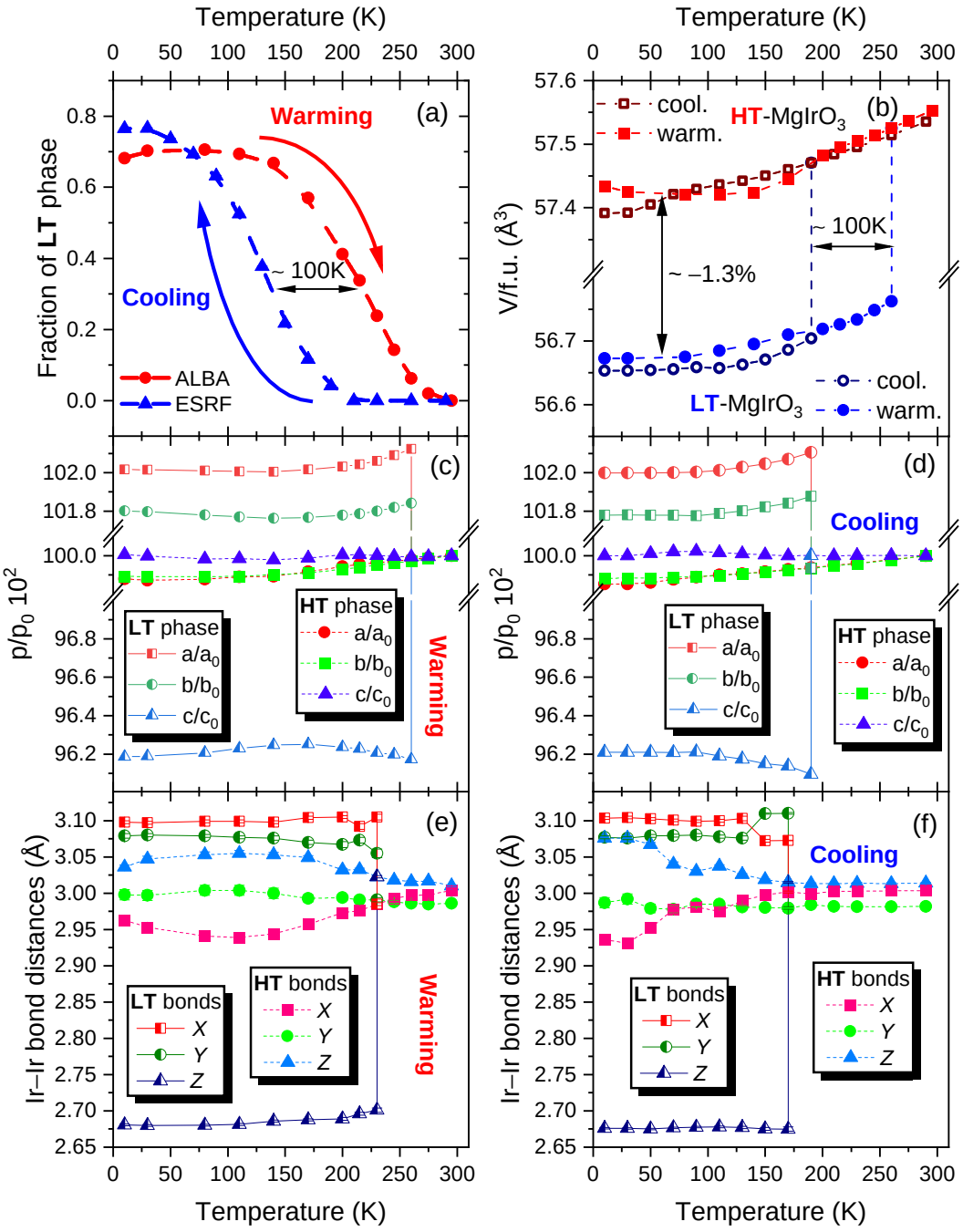

Figure 3.15: (a) Volume fraction of the **LT**-phase of β-$MgIrO_3$ as a function of temperature upon warming and cooling. (b) Temperature dependence of the unit cell volume V per formula unit of the **HT**- and **LT**-phases. (c),(d) lattice parameters and (e), (f) Ir–Ir bond distances in the XYZ-bond notation as a function of temperature upon warming and cooling, respectively. If not shown, the error bar is smaller than the symbol size. All lattice constants are normalized to the values of the **HT**-phase at RT.

The opposite behavior of the Ir–O–Ir bond angles in the **HT**- and **LT**-phases completely complements the temperature evolution of Ir–Ir bond distances. Shortening of the *Z*-bond in the **LT**-phase leads to the drastic narrowing of the Ir–O1–Ir and Ir–O2–Ir angles and expansion of other Θ's (Table 3.10).

Table 3.10: Ir–O–Ir bond angles of the **HT**- and **LT**-phases of β-$MgIrO_3$ at room temperature and 1.5 K obtained from the Rietveld refinement of the neutron diffraction data.

Angles	Θ^{RT} (deg)	$\Theta^{BT}_{\mathbf{HT}}$ (deg)	$\Theta^{BT}_{\mathbf{LT}}$ (deg)	Bond direction
Ir–O1–Ir	96.1(6)	96.0(16)	81.8(5)	between chains Z
Ir–O2–Ir	94.9(5)	100.3(17)	84.6(5)	
Ir–O3–Ir	95.2(4)	92.2(13)	100.3(5)	intrachain X
Ir–O4–Ir	95.6(3)	93.8(9)	100.4(4)	intrachain Y

3.2.4 Similarities of the β-MIrO$_3$ compounds

In the previous section, the main features of the crystal structure of each β-MIrO$_3$ compound were highlighted separately. However, besides retaining the hyperhoneycomb lattice of Ir atoms, new substituted Kitaev iridates demonstrate other similarities that will be discussed now.

Lattice expansion. Two different strategies for tuning magnetic properties in the Li_2IrO_3 family can be assumed: external pressure and chemical substitution. As discussed earlier, pressure experiments lead to a significant contraction of the unit cell volume that eventually results in the dimerization of Ir–Ir bonds and magnetic collapse. On the other hand, choosing the right doping element for the Li substitution in β-Li_2IrO_3 may on the contrary lead to the lattice expansion and be understood as the application of negative pressure to the hyperhoneycomb framework. The latter should leave the system away from the long-range magnetic order as J, K and Γ terms in the Kitaev model are strongly dependent on the local geometry: the distances between Ir atoms and the Ir–O–Ir bridging angles on the hyperhoneycomb lattice.

In the case of the new iridates β-MIrO$_3$ synthesized by ionic exchange reaction with divalent metals, the unit cell volumes have increased noticeably compared to the parent compound β-Li_2IrO_3 (Table 3.11). Enlarged cell volumes affect the crucial Ir–Ir bond distances and Ir–O–Ir bond angles leading to their increase; the Θ angles approach 100° along particular bond directions that probably tune the new iridates in the direction of the Kitaev limit, with the large ferromagnetic K and $|J|, |\Gamma| \ll |K|$ [17].

Interestingly, chemical substitution with divalent cations into the layered iridate α-Li_2IrO_3 leads to lattice compression [31] and long-range magnetic order in α-$MgIrO_3$ and α-$ZnIrO_3$ [138] (see also Table 3.12).

Except clear changes of the cell volume, the expansion of the a parameter is also prominent from the pure β-Li_2IrO_3 to β-$ZnIrO_3$. This may be a result of one octahedral position being emptied rather than appearing of the new tetrahedral one. This behavior can be compared to the fully substituted β-H_2IrO_3 ($Fddd$) in which all Li atoms are exchanged by hydrogen. H atoms mostly form short H–O bonds close to the IrO_6 octahedra and rather occupy a particular position [123]. Therefore, one can assume that the major part of octahedral sites are emptied which also manifests itself in a great expansion along the a direction (Table 3.11). Additionally, the same tendency can be tracked between pure α-Li_2IrO_3 and partially depleted $Li_{2-x}IrO_3$ [153]. Deintercalation of Li atoms from pure α-Li_2IrO_3 upon electrochemical cycling leads to a depletion of Li octahedral sites within the honeycomb Ir_2O_6 layers and formation of interlayer tetrahedral positions of LiO_4. In turn, this affects the lattice parameters of $Li_{2-x}IrO_3$ with an expansion along the a direction (Table 3.12).

Table 3.11: Comparison of parent β-Li_2IrO_3 and substituted compounds with the hyperhoneycomb lattice: ionic radius r for the six-fold coordinated ion [140], lattice parameters (a, b, c, β), and unit cell volume V per formula unit. Lattice parameters of the new magnesium iridates, β-Li_2IrO_3 and β-H_2IrO_3 ($Fddd$) have been re-calculated for the $P2_1/c$ unit cell of β-$ZnIrO_3$ to facilitate the comparison.

Compound	r (Å)	a (Å)	b (Å)	c (Å)	β (deg)	V (Å^3)	Ref.
β-$ZnIrO_3$	0.74	8.7656	5.9228	9.9249	116.15	57.82	This work
β-$MgIrO_3$	0.72	8.7221	5.9726	9.8325	116.02	57.54	This work
β-(Li,Mg)IrO_3	0.76/0.72	8.6932	5.9433	9.8317	116.30	56.92	This work
β-Li_2IrO_3	0.76	8.4562	5.9104	9.8655	115.38	55.69	[97]
β-H_2IrO_3	–	9.0717	5.3961	10.3242	116.06	56.75	[123]

Table 3.12: Comparison of parent α-Li_2IrO_3 and substituted compounds with the honeycomb lattice: ionic radius r for the six-fold coordinated ion [140], lattice parameters (a, b, c, β), and unit cell volume V per formula unit. Lattice parameters of $AIrO_3$ with A = Mg, Zn ($R\bar{3}$) have been re-calculated for the $C2/m$ unit cell of α-Li_2IrO_3 to facilitate the comparison.

Compound	r (Å)	a (Å)	b (Å)	c (Å)	β (deg)	V (Å^3)	Ref.
α-$MgIrO_3$	0.72	5.158	8.935	4.418	90	53.46	[138]
α-$ZnIrO_3$	0.74	5.199	9.005	4.445	90	54.20	[138]
α-Li_2IrO_3	0.76	5.175	8.936	5.119	109.83	55.68	[86]
$Li_{0.5}IrO_3$	–	5.219	8.898	4.455	91.36	51.71	[153]

Symmetry lowering. The crystal structure of the new β-MIrO$_3$ iridates suggests the lower monolinic space group in contrast to the higher symmetric orthorhombic one of the original β-Li$_2$IrO$_3$. Symmetry lowering introduces the pronounced anisotropy of Ir–Ir bond distances and distribution of angles between the X-, Y -, and Z-bonds caused by its non-uniform environment of MO$_4$ and MO$_6$ polyhedra. In β-ZnIrO$_3$, anisotropic behavior of the parameters is more distinct, but the structure remains ordered due to distinguishable positions of Zn atoms. In β-MgIrO$_3$ and β-(Li,Mg)IrO$_3$, the structure is strongly affected by cation disorder, and the partial occupancy of tetrahedral and octahedral positions additionally influence on the XYZ-bonds and corresponding angles which ultimately leads to spontaneous dimerization upon cooling in β-MgIrO$_3$ (see the Section 3.2.3).

The presence of anisotropy in the XYZ-bond directions as well as cation disorder in M metal positions affect the magnetic properties of the new Kitaev iridates that will be shown in the next chapter.

Chapter 4

Magnetic properties of β-MIrO$_3$

Despite the similarities of the β-MIrO$_3$ crystal structures manifested in the preservation of the hyperhoneycomb motif of Ir atoms and lattice expansion in comparison with the parent compound β-Li$_2$IrO$_3$, magnetism in the new Kitaev iridates is unique upon closer examination and significantly differs from each other. Prominent anisotropy in the structure of each compound described in the previous Chapter 3 leads to a noticeable diversity in magnetic properties of β-MIrO$_3$. Therefore, each compound will be discussed separately to emphasize the differences in magnetic behavior.

4.1 Methods of characterization

Magnetization. Magnetization was measured using the MPMS3 (Magnetic Property Measurement System) SQUID magnetometer from Quantum Design. The molar susceptibility χ_{mol} was defined by the following equation:

$$\chi_{\text{mol}} = \frac{M}{H} \cdot \frac{M_{\text{mol}}}{m} \cdot 4\pi \cdot 10^{-6} \left[\frac{\text{m}^3}{\text{mol}}\right] \approx \frac{M}{H} \cdot \frac{M_{\text{mol}}}{m} \left[\frac{\text{emu}}{\text{mol}}\right]. \tag{4.1}$$

Here, M stands for magnetization in emu, H is magnetic field in Oe, M_{mol} is molar mass in g/mol, and m is mass of a sample in g. High-temperature paramagnetic part of the magnetic susceptibility was fitted using the Curie-Weiss law with subsequent calculation of the effective magnetic moment μ_{eff} measured in Bohr magnetons μ_{B} per formula unit by the following expressions:

$$\chi_{\text{mol}} = \frac{C}{(T - \theta_{CW})} \tag{4.2}$$

$$\mu_{\text{eff}} = 797.8\sqrt{\chi^{SI}_{\text{mol}} T}\ \mu_{\text{B}} \approx 2.827\sqrt{C}\ \mu_{\text{B}} \qquad [7] \tag{4.3}$$

where C is a Curie constant measured in emu mol^{-1} K^{-1}, θ_{CW} is the Curie-Weiss temperature in K, χ^{SI}_{mol} is molar susceptibility measured in m^3 mol^{-1}.

The magnetization expressed in Bohr magneton per formula unit (μ_{B}/f.u.) was defined as:

$$M = \frac{M[\text{emu}]}{\mu_{\text{B}} N_A} \cdot \frac{M_{\text{mol}}}{m} \approx \frac{M[\text{emu}]}{5585} \cdot \frac{M_{\text{mol}}}{m} \left[\frac{\mu_{\text{B}}}{\text{f.u.}}\right]. \tag{4.4}$$

High-filed magnetization measurements were performed in the Dresden High Magnetic Field Laboratory using a pulsed magnet powered by an 1.44 MJ capacitor bank. With an inner bore of 20 mm, the magnet yielded fields up to 57 Tesla with a rise time of 7 ms and the total pulse duration of about 20 ms. Magnetic moment of the sample was obtained by integration of the voltage induced in a compensated pick-up coil system surrounding the sample. Each measurement was performed twice, with and without the sample, in order to remove the background signal contribution.

Heat capacity. Specific heat measurements were carried out on a polycrystalline sample pressed into pellets with the average mass of $\sim$ 7 mg in the Quantum Design PPMS (Physical Property Measurement System) with thermal relaxation method.

μSR measurements. Ambient-pressure μSR experiments were carried out on the HiFi spectrometer at the STFC-ISIS (UK) pulsed muon source, and on the GPS spectrometer at the PSI (Switzerland) continuous muon source. The μSR time spectra were analyzed using the MUSRFIT software package [154] for the data collected at PSI, and the WIMDA software package [155] for the data collected at STFC-ISIS. 2 g polycrystalline samples were used.

4.2 Static and dynamic spins in β-$ZnIrO_3$

4.2.1 Magnetization and specific heat measurements

Figure 4.1a shows the temperature dependence of the DC magnetic susceptibility χ_{mol} for β-$ZnIrO_3$ measured in several fields. The curves do not demonstrate any drastic temperature anomalies or a sharp increase/decrease of the molar susceptibility in the entire temperature range meaning a complete suppression of the magnetic order ($T_{\text{N}} \simeq 38$ K) of the parent compound β-Li_2IrO_3. Only below $T_a \sim 5$ K the magnetic susceptibility changes slope and reaches the constant value. Calculated Fisher's heat capacity [156] corresponds to a broad rounded peak at the same temperature T_a at 0.1 T as well as an increase below 50 K at different fields indicating a deviation from the paramagnetic behavior. At higher temperatures, inverse susceptibility follows the conventional Curie-Weiss behavior (Fig. 4.1b) with the paramagnetic effective moment of 1.81(1) μ_{B} that resembles 1.73 μ_{B} expected for the $j_{eff} = \frac{1}{2}$ state of Ir^{4+}. The latter follows from:

$$\mu_{\text{eff}} = g_J \mu_{\text{B}} \sqrt{\mathcal{J}(\mathcal{J}+1)}, \quad \text{where } g_J = 2 \text{ and } \mathcal{J} = \frac{1}{2} \qquad [7] \qquad (4.5)$$

The Curie-Weiss temperature is ferromagnetic ($\theta_{\text{CW}} = 12.4(2)$ K), similar to the powder-averaged value of $\theta_{\text{CW}} = 21$ K in β-Li_2IrO_3 [98]. Here, one might try to estimate the frustration index $f = |\theta_{\text{CW}}|/T_{\text{N}}$, but this parameter

is determined only for the systems with a clear magnetic transition. Therefore, in the case of β-$ZnIrO_3$ this approach is not applicable.

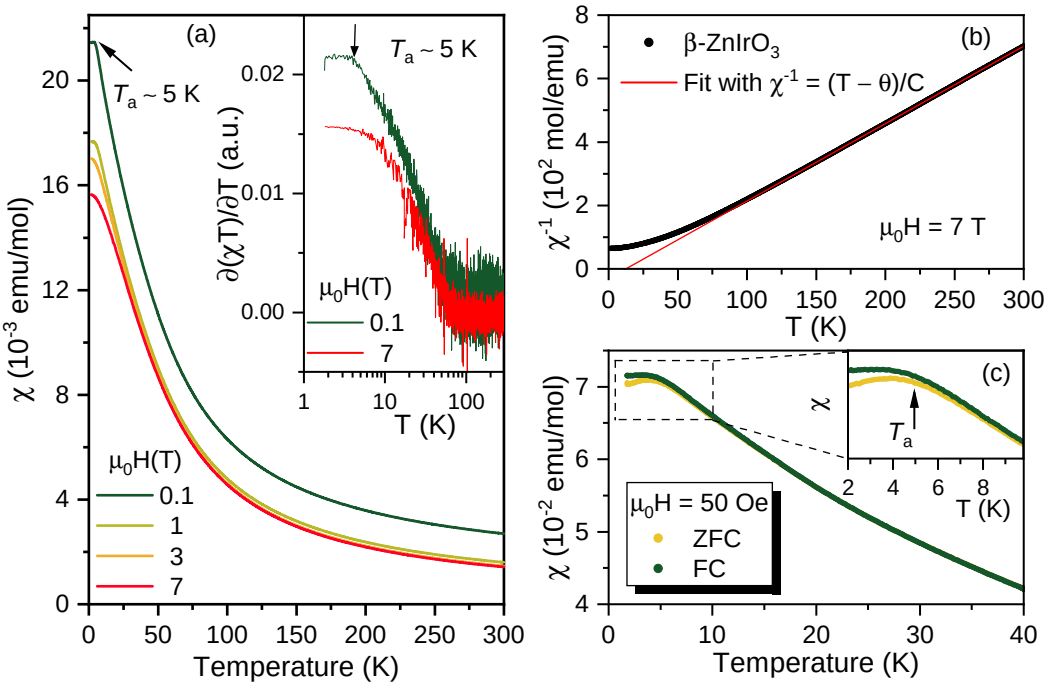

Figure 4.1: (a) Temperature dependence of DC magnetic susceptibility for β-$ZnIrO_3$ at several fields. The black arrow marks the anomaly temperature T_a. The inset shows the Fisher's heat capacity at 0.1 and 7 T. (b) Inverse magnetic susceptibility $1/\chi$; the red solid line displays the Curie-Weiss fit at high temperatures between 150 and 300 K. (c) Zero-field-cooled (ZFC) and field-cooled (FC) susceptibility data measured at 50 Oe. The inset shows the zoomed area of $\chi(T)$ up to 10 K.

In the absence of a clear long-range magnetic order, the next step was measuring the magnetization in zero-field cooling (ZFC) and field cooling (FC) regimes at small fields to inspect whether spins in the system freeze or not. Indeed, the susceptibility curves most clearly bifurcate below $T_a \sim 5$ K and only above 15 K completely overlap (Fig. 4.1c). Despite the curves splitting in DC measurements, AC susceptibility data illustrated by Fig. 4.2 disprove a typical spin-glass behavior in β-$ZnIrO_3$: while the real parts χ' resemble ZFC-susceptibility behavior without a characteristic for spin glasses frequency shift of the peak maximum and decrease of the peak intensities, the imaginary parts χ'' almost remain constant and slightly fluctuate around mean values.

Isothermal magnetization of β-$ZnIrO_3$ at 3 K (the inset in Fig. 4.3a) demonstrates linear behavior up to 7 T. In the high-field magnetization data, two anomalies are observed at $H_{c1} \sim 10$ T and $H_{c2} \sim 14$ T, one is better visible in the differential susceptibility dM/dH (Fig. 4.3b) and another one in $M(H)$ (Fig. 4.3a), respectively. While the origin of the anomaly in dM/dH is unclear, a smeared kink observed at 14 T suggests an induced phase transition at this field, however, the saturation plateau has not been achieved. The magnitude of magnetization at H_{c2} is remarkably large, $\sim 0.37\ \mu_B$/f.u., but is very close

to $\frac{1}{3}$ of the saturation value (1 μ_B/f.u.) expected for Ir^{4+} with $j_{eff} = \frac{1}{2}$ and observed magnetization at $H_c \simeq 2.8$ T for β-Li_2IrO_3 [97, 98]. Above 14 T, the data demonstrate the linear increase in $M(H)$, as confirmed by the flat curve on the differential susceptibility dM/dH suggesting the absence of any further field-induced transformations above H_{c2}.

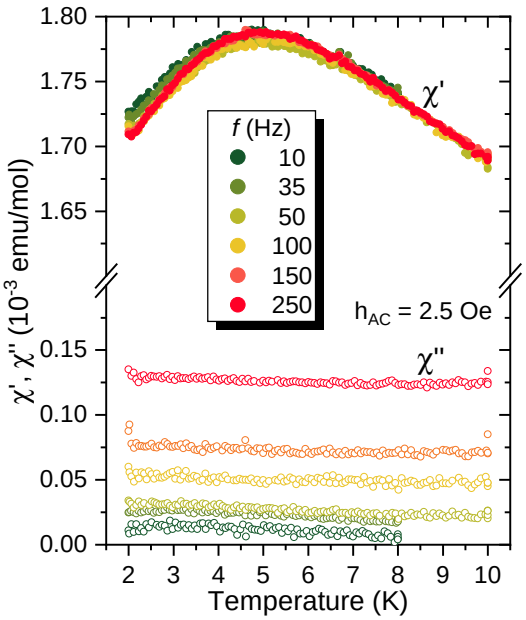

Figure 4.2: Real (χ') and imaginary (χ'') parts of β-$ZnIrO_3$ AC magnetic susceptibility as functions of temperature for frequencies from 10 to 250 Hz in the external field of 10 Oe. The amplitude of the oscillating magnetic field is 2.5 Oe.

In accord with this, temperature dependence of the specific heat divided by temperature C/T measured at different fields also demonstrates the absence of a long-range magnetic order in β-$ZnIrO_3$ as well as any anomaly at T_a visible in the susceptibility data (Fig. 4.3c). Based on the crystal structure analysis, the new zinc iridate is free from the structural disorder and the phonon contribution at low temperatures should be negligible meaning that any possible magnetic transition would be visible in the recorded data. On the other hand, in the absence of a decent non-magnetic compound with the similar structure to be used as a lattice contribution, the full magnetic heat capacity of β-$ZnIrO_3$ is not available yet. However, the low-temperature ($T < T_a \sim 5$ K) specific heat data can be analyzed using the power law $C/T = \gamma + \beta T^2$ (Fig. 4.3d), where the Sommerfeld coefficient γ (the linear term) represents the electron contribution to the specific heat, and β is the Debye constant specific for each material. Although the resulted fits are less accurate due to the limited number of measured temperatures, the γ-values were found nonzero corresponding to $\gamma = 10.1(3)$ mJ/mol K^2 in zero field measurements and $\gamma = 2.3(3)$ mJ/mol K^2 at 14 T. Therefore, the finite term γ in the specific heat suggests possible fermionic excitations typical of a QSL state.

Nevertheless, the preliminary characterization of β-$ZnIrO_3$ by magnetization and heat capacity measurements reveals the suppression of the long-range magnetic order, but weak splitting of ZFC/FC susceptibility curves below 5 K suggests some sort of spin freezing and deviation from the purely spin-liquid behavior. To shed a light on this ambiguity, the new Kitaev iridate β-$ZnIrO_3$ was studied by μSR technique which is sensitive to a local magnetism in the frustrated systems.

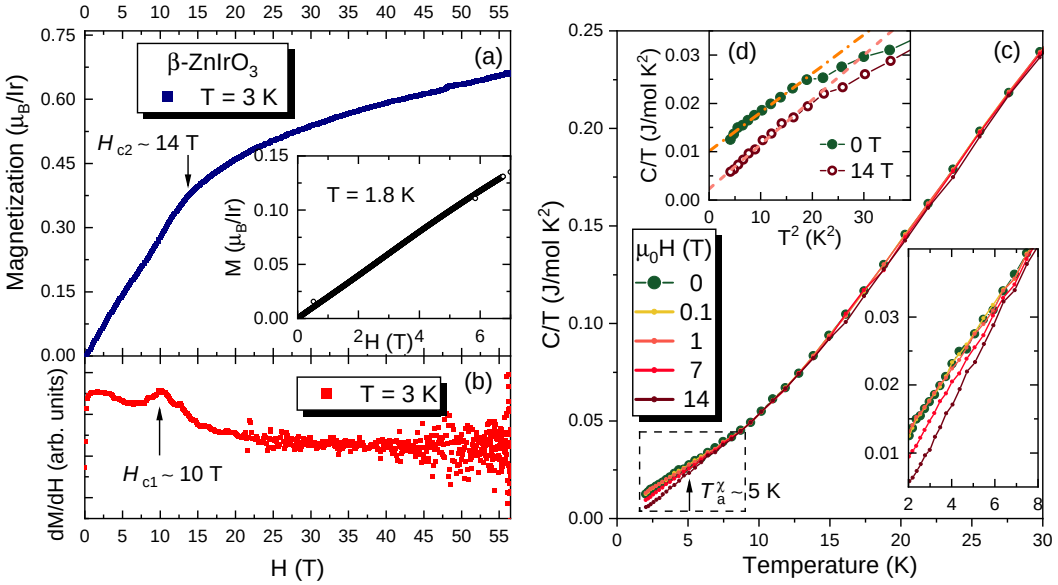

Figure 4.3: (a) Magnetization (M) and (b) differential susceptibility (dM/dH) curves of β-ZnIrO$_3$ at 3 K. The inset shows the DC isothermal magnetization $M(H)$ as a function of magnetic field measured at 1.8 K. (c) Temperature dependence of the specific heat divided by temperature C/T for β-ZnIrO$_3$. The inset displays the enlarged view of the low-temperature range from 2 to 8 K. (d) C/T versus T^2 plots at 0 and 14 T below 7 K. The dashed lines are the fits to the equation $C/T = \gamma + \beta T^2$.

4.2.2 μSR study

Weak Transverse Field (wTF) measurements. First of all, it will be useful to verify whether spins in β-ZnIrO$_3$ fluctuate or freeze, and if there is a mixture of static and dynamic contributions, then evaluate their ratio and determine the characteristic temperatures. μSR transverse field measurements in the weak external field (wTF) are commonly used [157] for such purpose. The wTF data were described as a sum of two functions (multiplied by a weak exponential decay) representing static and paramagnetic contributions, respectively:

$$\begin{aligned} A_{wTF}(t) &= A_0 \left[f_{st} G_z^L(t) + (1 - f_{st}) \cos(\omega t + \phi) \right] e^{-\lambda t}, \\ G_z^L(t) &= \frac{1}{3} + \frac{2}{3}(1 - \lambda_{st} t) e^{-\lambda_{st} t} \end{aligned} \tag{4.6}$$

where f_{st} stands for the fraction of static spins, ω is the oscillation frequency corresponding to the weak transverse field of 20 G, $G_z^L(t)$ is the Kubo-Toyabe relaxation function, and λ_{st} is the relaxation rate describing random local fields at muon sites (so-called Lorentzian Field Distribution). Since the experiments on β-ZnIrO$_3$ were performed at both HiFi (STFC-ISIS) and GPS (PSI) facilities, the absolute values of variable and starting parameters differ from each other. The total asymmetry A_0 was fixed during the fitting at a

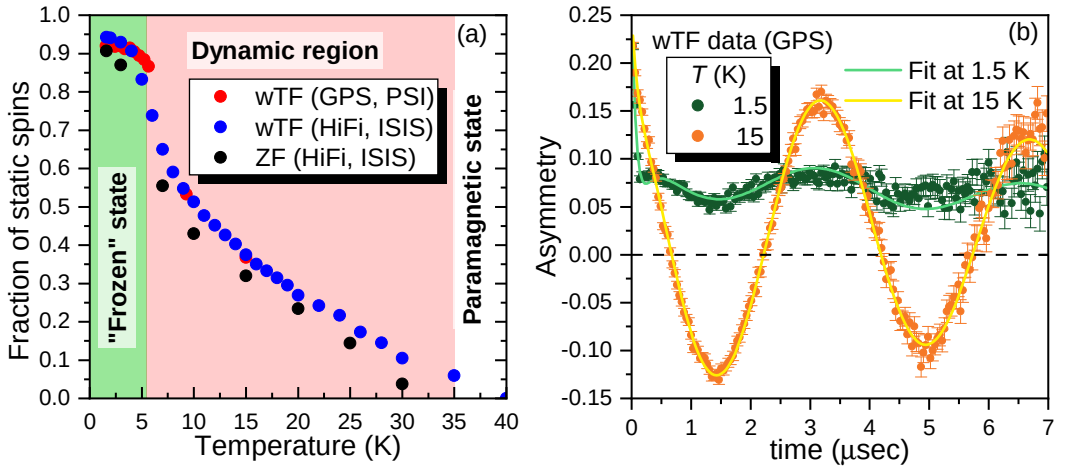

Figure 4.4: (a) Volume fraction of static spins measured in the wTF and ZF experiments on β-$ZnIrO_3$. The color panels separate different temperature regions described in the text. (b) wTF-μSR time spectra at selected temperatures. The solid lines represent a fit to the data.

constant values of 0.278 and 26.95 from the calibration of the GPS and HiFi spectrometers, respectively. The phase ϕ was also set to an average values of 31.5 and -4 from the fitting of high-temperature data in the paramagnetic range. Therefore, the contribution of static spins f_{st} in both experiments was recalculated to the relative volume fraction illustrated in Fig. 4.4a.

The fit of the wTF data indicates three distinguishable temperature regions. The first one manifests itself by a large static contribution below 5.5 K that is close to the temperature T_a from the magnetic susceptibility measurements. The fraction of static spins reaches 90–95% corresponding to a "frozen" state in β-$ZnIrO_3$. The rest of the spins seems to be intrinsic and dynamic because the paramagnetic background contribution, on the one hand, is negligible in the experiments at the GPS, and, on the other hand, was taken into account in the HiFi measurements. Additionally, the phase analysis of high-resolution PXRD didn't show a significant amount of any impurity phases in the β-$ZnIrO_3$ samples, therefore, the paramagnetic contribution from possible impurity phases is irrelevant. The strong effect of internal static fields is also visible from the wTF-μSR time spectra at selected temperatures (Fig. 4.4b) from an abrupt drop of the asymmetry spectra as well as by a reduced signal of the oscillating paramagnetic spins.

The second temperature range lies between 5.5 and $\sim$ 35 K in which the fraction of frozen spins gradual decreases with temperature. The coexistence of static and paramagnetic contributions in this range, "Dynamic region", can also be seen from the wTF-μSR time spectra at higher temperatures of $\sim 3T_a$ where the total asymmetry is still not fully recovered due to the presence of static moments (Fig. 4.4b). The last temperature range starts above 35 K where the whole sample becomes paramagnetic. In total, μSR data collected at the different muon facilities are consistent, and the volume fraction of static spins is reproduced quite well. To clarify the magnetism of β-$ZnIrO_3$ in the frozen and dynamic regions, further μSR measurements were performed in

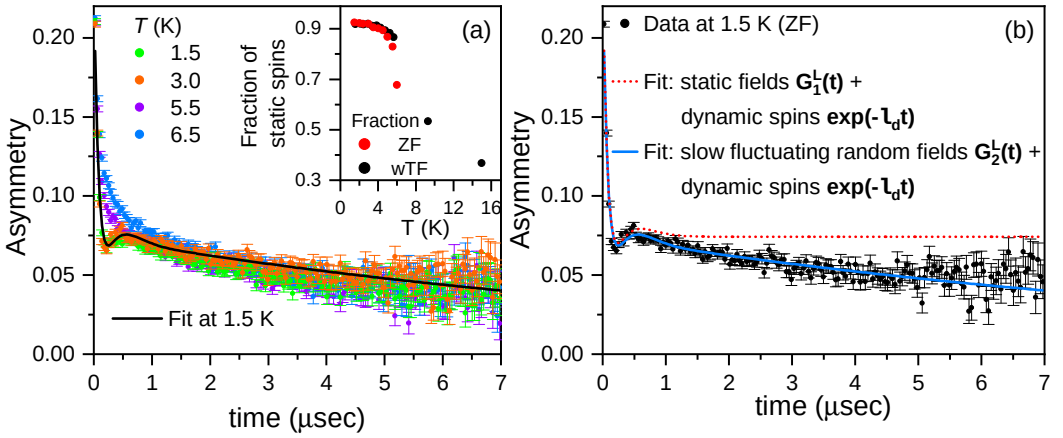

Figure 4.5: (a) Representative zero field (ZF) time spectra of β-$ZnIrO_3$. The solid line is a fit to the data at 1.5 K. The inset shows the fraction of static spins obtained from the fit to the ZF and wTF measurements at GPS. (b) Muon asymmetry at 1.5 K with two approaches of describing the ZF data.

the absence of external fields (zero field (ZF) mode).

Frozen state. Preliminary wTF measurements revealed that around 90% of the sample exhibits static magnetism, however, no well-defined oscillations that would be expected in the case of long-range magnetic order were seen in the zero field measurements. Instead, ZF-μSR time spectra demonstrate the fast relaxation at $t < 0.2$ μs with small but still pronounced dip as a contribution of static spins, and the slow relaxation tail. The denoted minimum shrinks with temperature and vanishes above $\sim$ 5.5 K corresponding to the transition into the dynamic region (Fig. 4.5a).

The ZF data representing the frozen state were primarily collected at GPS (PSI) and fitted by the sum of two functions that describe frozen and dynamic spins, respectively:

$$\begin{aligned} A_{ZF}(t) &= A_1 \left[f_{st} G_z^L(t) + (1 - f_{st}) e^{-\lambda_d t} \right], \\ G_1^L(t) &= \frac{1}{3} + \frac{2}{3}(1 - \lambda_a t) e^{-\lambda_a t}, \\ G_2^L(t) &= \frac{1}{3} e^{-\frac{2}{3}\nu t} + \frac{2}{3}(1 - \lambda_a t) e^{-\lambda_a t} \end{aligned} \tag{4.7}$$

where f_{st} stands for the fraction of static spins, $G_z^L(t)$ is the Kubo-Toyabe relaxation function (see below), and λ_d is the relaxation rate of dynamic moments. The asymmetry A_1 represents the signal amplitude of the sample estimated from the wTF measurements through the total asymmetry and the phase as $A_1 = A_0 \cos(\phi) = 0.278 \cos(31.5) \simeq 0.237$. The Kubo-Toyabe relaxation function $G_z^L(t)$ in the form of $G_1^L(t)$ with one variable parameter λ_a (the spatial field distribution) was originally proposed to fit the main static contribution below $\sim$ 5.5 K. In this form, the depolarization function $G_1^L(t)$

corresponds to randomly oriented static magnetic moments when the internal field is mostly uniform but there is no clearly defined direction of the field [157, 158]. The total relaxation function $A_{ZF}(t)$ with $G_1^L(t)$ describes the fast relaxation part quite well, but does not fit the $\frac{1}{3}$-tail at longer times. Therefore, the second function $G_2^L(t)$ was applied to fit the ZF data. Indeed, the modification of the $\frac{1}{3}$-tail to the form of $\frac{1}{3}\exp(-\frac{2}{3}\nu t)$ significantly improved the fit of the data, as illustrated in Fig. 4.5b, while the initial damping rate of the $\frac{2}{3}$-component was kept unchanged. Here, the relaxation rate λ_a represents the half-width at half-maximum of the Lorentzian distribution of random internal fields, and ν corresponds to the rate of fluctuations of the local field [66, 159]. Moreover, the fraction of static spins f_{st} obtained interdependently from the fit of ZF-μSR is in a good agreement with the static contribution calculated from the wTF data (Fig. 4.4a).

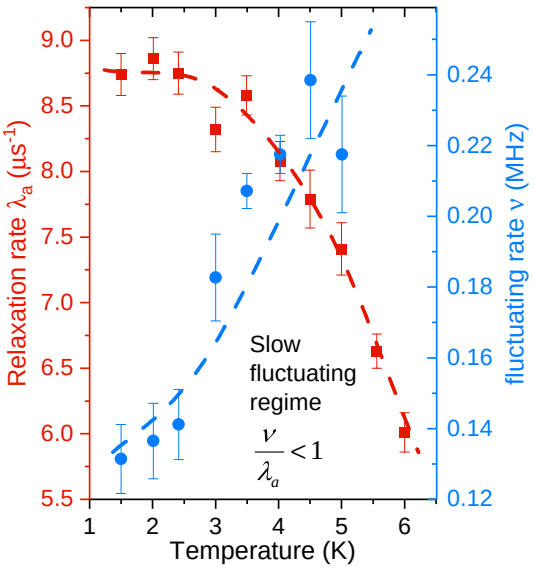

Figure 4.6: Temperature dependence of the relaxation rate λ_a representing the local fields distribution and the fluctuation rate ν in the frozen region – the case of slow modulations or quasi-static local fields. The dashed lines are guides for the eye.

The extracted parameters λ_a and ν are plotted in Fig. 4.6. Whereas the relaxation rate λ_a as the local field distribution reduces with temperature down to 6 K, the hopping rate ν rapidly increases up to $\sim$ 5 K – around the same temperature T_a of the anomaly in the magnetic susceptibility data. In the frozen state below 5 K, the spins are not fully static, and the resulting fitting function $A_{ZF}(t)$ represents a coexistence of slow fluctuating random fields with $a/\nu \ll 1$ (slow hopping) [66] and a small fraction of dynamic spins. The λ_a values that describe the width of the local fields distribution return mean static field $\langle B \rangle = a/\gamma_\mu \simeq 105$ Oe at 1.5 K and $\langle B \rangle \sim 71$ Oe at 6 K ($\gamma_\mu = 2\pi \times 1.35 \times 10^{-2}$ μs^{-1} Oe^{-1} = 851.615 MHz/T) as a weakening of the internal fields. In the case of α- and β-Li_2IrO_3 which develop the long-range magnetic order, the oscillation frequency ω for the particular field direction is used instead of the spatial distribution of local fields. For α-Li_2IrO_3, the oscillation frequency of $\omega \approx 15$ MHz [93] at the lowest temperature would return the mean field $\langle B \rangle \simeq 176$ Oe. For β-Li_2IrO_3 with the three oscillating frequencies of 2.7, 3.3, and 4 MHz [106], the mean field as a sum of these contributions corresponds to $\langle B \rangle \simeq 117$ Oe. The $\langle B \rangle$-value of the new β-$ZnIrO_3$ appears to be lower but comparable with the magnetically ordered parent compounds suggesting the similar contribution of the Ir magnetic moments, but leading to a disordered magnetic state in β-$ZnIrO_3$. Further data analysis between 5.5 and 6 K was performed with

less accuracy due to the non-ideal fit of the data by the suggested relaxation function $A_{ZF}(t)$ with $G_2^L(t)$, where a dip in the fast relaxation part vanishes (Fig. 4.6a), and the fraction of static spins starts to gradually decrease indicating the transition into the dynamic region.

Dynamic region The low temperature range, *i.e.* frozen region, was comprehensively studied at GPS (PSI), while the informative ZF-μSR data above 5 K were collected at HiFi (ISIS). In Fig. 4.7a, the fast relaxation is primarily observed as a missing polarization at $t < 0.2$ μs which is outside the bandwidth of the pulsed muon facility. However, the remaining data are sufficient to make some conclusions about spin behavior in the dynamic region.

Generally, the coexistence of fast and slow relaxation processes may be fitted by the sum of simple exponential decays. After trying several functions, ZF-μSR spectra at temperatures above 5.5 K were described by

$$A_{ZF}(t) = A_{fast}e^{-\sqrt{\lambda_{fast}t}} + A_{pm}e^{-\lambda_{pm}t} + A_{bg}, \tag{4.8}$$

where the first term represents a "root-exponential" decay of the fast depolarization process, the second term expresses a paramagnetic spin contribution to the muon depolarization, and the term A_{bg} is a temperature independent non-relaxing background signal from those muons that stop in the sample holder or cryostat tails. The corresponding A_{fast} and A_{pm} amplitudes were recalculated into the fractions of static and paramagnetic spins with respect to the background (Fig. 4.4a). It worth mentioning that the relaxation function in the form of stretched exponent $e^{-(\lambda t)^{\beta}}$ was originally suggested to describe the fast relaxation contribution in the ZF-μSR spectra. However, data fit with β as a variable parameter led to the values of $0.44 - 0.5$ and did not qualitatively affect the extracted relaxation rates λ_{fast} and λ_{pm} as well as the ratio of static and dynamic contributions. Therefore, the parameter β was fixed during the refinement and set to a constant value of 0.5 that yields the final form $e^{-\sqrt{\lambda_{fast}t}}$. Moreover, the "root-exponential" form of the relaxation function may be interpreted as the case of rapidly fluctuating random fields [66, 159].

In the dynamic region, the fast-relaxation rate λ_{fast} rapidly decreases with temperature and follows the fraction of static spins obtained from the fit of the wTF-μSR data. On the other hand, the paramagnetic rate λ_{pm} is much slower than λ_{fast} with the maximum value of 0.089(6) μs^{-1} at 6.5 K and then slightly decreases with temperature (Fig. 4.7b). The presence of two different relaxation channels, λ_{fast} and λ_{pm}, in the dynamic region suggests that static spins of the random local fields in the frozen region progressively "unfreeze" above 5.5 K. One part of the spins contribute to the paramagnetic fraction with the slow relaxation rate λ_{pm}, while the rest of them still demonstrates fast relaxation component λ_{fast} caused by local fields.

The absence of a clear transition from the frozen to paramagnetic state along with a broad intermediate (dynamic) region with the width of $\sim$ 30 K

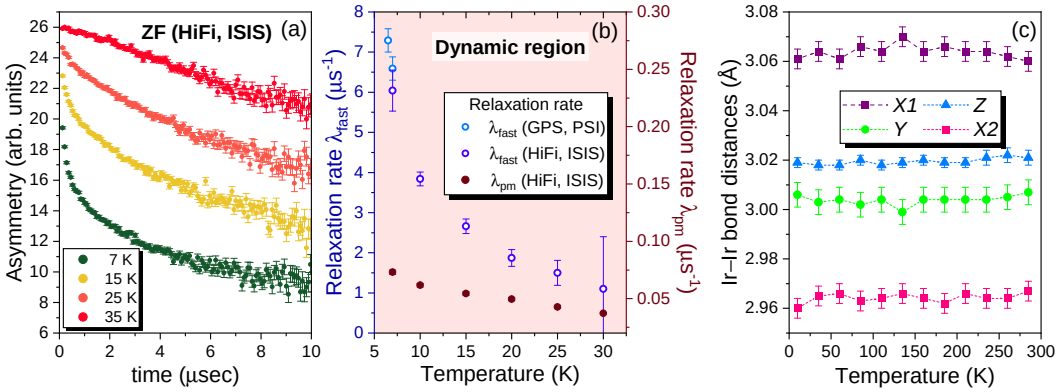

Figure 4.7: (a) Zero-field μSR time spectra in the dynamic region at selected temperatures. (b) Temperature dependence of the muon relaxation rates, λ_{fast} and λ_{pm}, in the dynamic region. (c) Ir–Ir bond distances of β-$ZnIrO_3$ as a function of temperature from the crystal structure refinement.

between them suggests the spin-glassy ground state in β-$ZnIrO_3$. Upon cooling, progressively developing short-range order correlations in the dynamic region lead to almost complete freezing of spins below $T_a \simeq 5$ K. However, even at the lowest temperature of 1.5 K, a small fraction of dynamic moments is still presented in the sample, and the "static" spins associated with the quasi-static random fields retain slow fluctuations, as described by the fluctuation rate ν. The main question is whether the formation of separate spin clusters takes place or the magnetic moments gradually freeze in a random way. Most probably, the answer lies somewhere in the middle: strong anisotropy of the Ir–Ir bond distances facilitates the formation of short-range order upon cooling or, in other words, clustering of iridium pairs, but temperature-independent behavior of the Ir–Ir bond lengths (Fig. 4.7c) suggests that at some point magnetic interactions between iridium ions overcome thermal fluctuations resulting in the partially frozen-spin state.

Interestingly, upon the completion of our work a publication reporting the synthesis and basic magnetization measurements on β-$ZnIrO_3$ appeared [160]. This compound is different from ours because it shows the *Fddd* symmetry and, therefore, a significant amount of structural disorder related to the random distribution of Zn^{2+} ions in the structure. Intriguingly, the magnetic behavior of such disordered samples is very similar to ours, yet no local probe like muSR was used to analyze their spin dynamics.

4.3 Magnetic collapse in β-$MgIrO_3$

4.3.1 Magnetic behavior of the nondimerized phase

Preliminary characterization. β-$MgIrO_3$ shows a structural phase transition accompanied by the appearance of the dimerized low-temperature (**LT**) phase that was extensively studied by x-ray and neutron diffraction

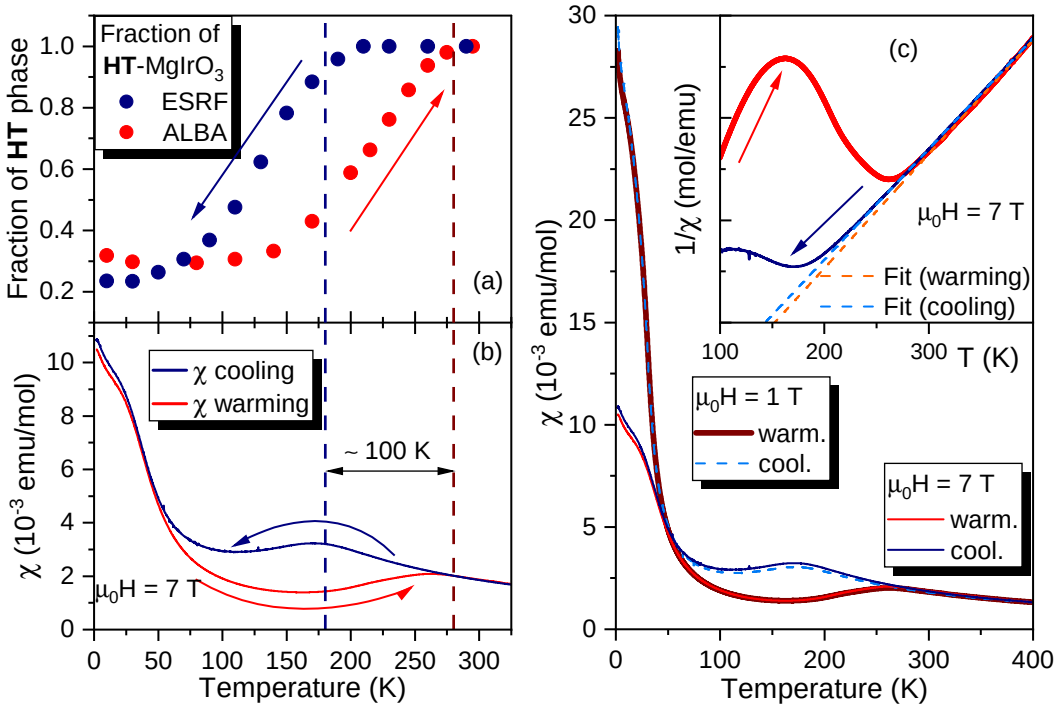

Figure 4.8: Comparison of the volume fraction of the **HT**-phase (a) and magnetic susceptibility measured at 7 T (b) as a function of temperature upon warming and cooling. (c) Temperature dependence of the β-$MgIrO_3$ magnetization at selected fields. The inset shows inverse susceptibility at high temperatures in the field of 7 T and the corresponding Curie-Weiss fit upon warming and cooling (dashed lines).

measurements described in detail in the Section 3.2.3. The transition, however, is incomplete; around $30-35\%$ of the high-temperature (**HT**) phase persists at the lowest temperature. Ir–Ir bond distances of the nondimerized β-$MgIrO_3$ slightly changes upon cooling leaving the **HT**-phase magnetic that should be seen from magnetization measurements.

First of all, the **LT**-**HT** transition is observed in the magnetic susceptibility data by a broad thermal hysteresis that corresponds well with the fraction of the **HT**-phase from the PXRD measurements (Fig. 4.8a-b). The transition is field-independent and completed at around 170 K and 270 K upon cooling and warming, respectively (Fig. 4.8c). At higher temperatures, inverse susceptibility follows the conventional Curie-Weiss behavior with the paramagnetic effective moment of $\sim 1.90\ \mu_B$ close to the μ_{eff} of β-$ZnIrO_3$ and expected values for the $j_{eff} = \frac{1}{2}$ state of Ir^{4+}. The Curie-Weiss temperature is ferromagnetic ($\Theta_{warm} = 62.6(3)$ K and $\Theta_{cool} = 50.7(1)$ K). At lower temperatures, magnetic susceptibility decreases upon cooling, similar to the instances of magnetic collapse in β-Li_2IrO_3 [118], α-$MoCl_3$ [151], and α-$RuCl_3$ [161]. However, the decreasing trend due to the gradual formation of the non-magnetic **LT**-phase is countered by the increasing susceptibility of the remaining **HT**-phase. Its contribution becomes dominant below 100 K where susceptibility steadily increases as the fraction of the **HT**-phase reaches the constant value. This proves that magnetic collapse in β-$MgIrO_3$ is only partial, unlike in all

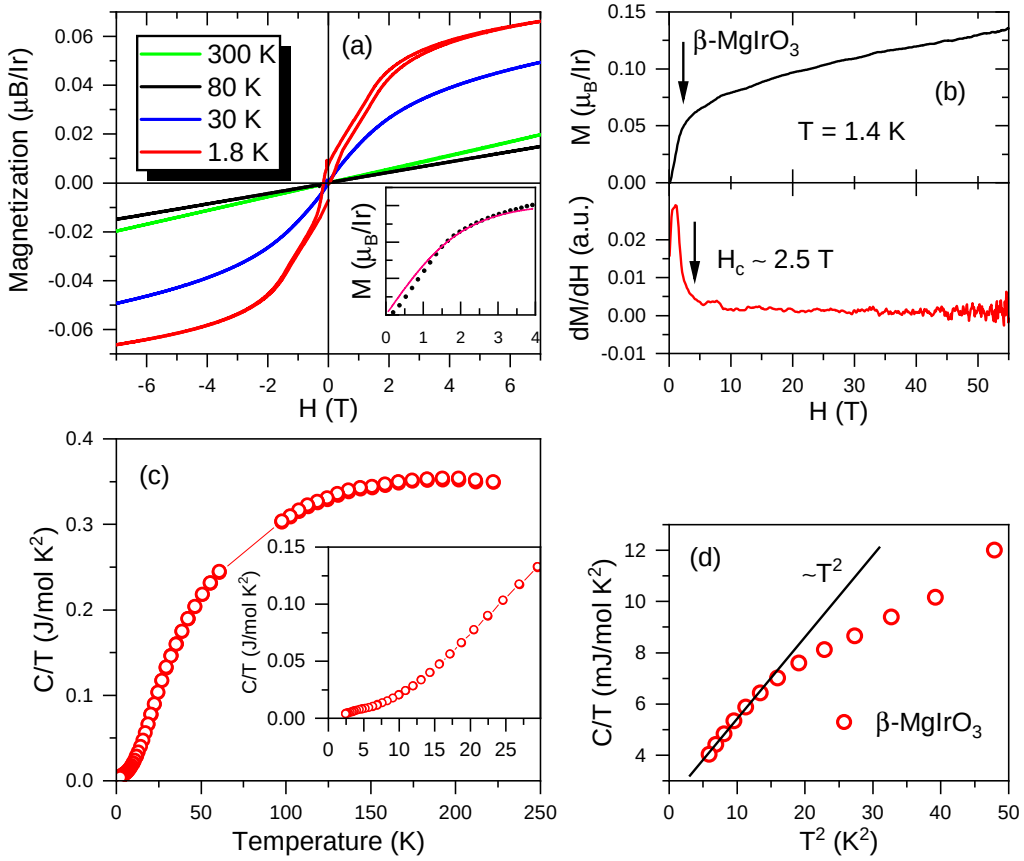

Figure 4.9: (a) Hysteresis loops of β-$MgIrO_3$ measured at 1.8, 30, 80, and 300 K. The inset shows a zoomed area of the high-field magnetization at 1.4 K versus the fit to the Eq. 4.11. (b) High-filed isothermal magnetization $M(H)$ at 1.4 K (upper panel) and differential susceptibility (dM/dH) curve (lower panel). The black arrow marks the kink at $H_c \sim 2.5$ T in the magnetization data. (c) Temperature dependence of the specific heat divided by temperature C/T in zero field. The inset shows the expanded view of the low-temperature data below 30 K. (d) C/T versus T^2 plot of β-$MgIrO_3$. The solid line is the fit to the equation $C/T = \gamma + \beta T^2$.

other materials studied to date. The **HT**-phase further shows an anomaly around 23 K. In low fields, this anomaly is accompanied by the divergence of the field-cooled and zero-field-cooled measurements, a hallmark of spin freezing (Fig. 4.10a), and was probed by the AC susceptibility measurements (see below).

Figure 4.9a demonstrates DC isothermal magnetization $M(H)$ of β-$MgIrO_3$ as a function of magnetic field measured at selected temperatures. Above 80 K, the sample shows a paramagnetic behavior by the linear increase of $M(H)$. A slightly bigger slope of the magnetization curve at 300 K than at 80 K is associated with the ratio of magnetic and dimerized phases: at room temperature β-$MgIrO_3$ is fully transformed into the **HT**-phase, while below 270 K the **LT**-phase gradually develops suppressing the fraction of the magnetic **HT**-phase. The deviation from the linear behavior of the magnetization curve at 30 K, just above the anomaly in the susceptibility data, may indicate

strongly interacting moments. At 1.8 K the hysteresis loop opens with a maximum coercive field of $\sim$ 1.6 kOe and remanent magnetization $\sim$ 0.00762 μ_B per formula unit. Above $H_c \sim$ 2.5 T, there is a kink in magnetization, followed by a gradual increase above 3 T. The magnitude of the magnetization above H_c is rather small, $\sim$ 0.06 μ_B/Ir, suggesting a weak ferromagnetism as in the case of the canted $j_{\text{eff}} = 1/2$ moments in Sr_2IrO_4 [162].

At high magnetic fields up to 56 T it was not possible to reach a saturation plateau. A smeared kink from the isothermal magnetization $M(H)$ is also observed by the drop in the differential susceptibility (dM/dH) around $H_c \sim$ 2.5 T (Fig. 4.9b). Thus, we tried to fit the low-field part of M with the Brillouin function at $T = 1.4$ K. In the case of paramagnetic spins, the magnetization is described by

$$M = M_s B_J(y), \tag{4.9}$$

where M_s stands for the saturation magnetization and $B_J(y)$ is the Brillouin function given by

$$B_J(y) = \frac{2J+1}{2J}\coth\left(\frac{2J+1}{2J}y\right) - \frac{1}{2J}\coth\left(\frac{y}{2J}\right) \text{ [7]} \tag{4.10}$$

with $y = g_J \mu_B JB/k_B T$. Assuming $J = \frac{1}{2}$ for β-$MgIrO_3$, the Brillouin function 4.10 reduces to

$$B_{1/2}(y) = \tanh(y). \tag{4.11}$$

Using $g_J = 2$, the Bohr magneton $\mu_B = 9.274 \times 10^{-24}$ J/T and the Boltzmann constant $k_B = 1.38 \times 10^{-23}$ J/K at $T = 1.4$ K, the variable parameter y can be reduced to $y = 0.48B$, where B is the magnetic field in Tesla. Thus, one can try to fit the low-field data by the Eq. 4.11. However, a close look at the data revealed a noticeable deviation from the simple linear behavior of the Brillouin function below the saturation magnetization (the inset in Fig. 4.9a), meaning that spins in the magnetic **HT**-phase are not paramagnetic, and, probably, demonstrate short-range order.

No sharp feature is observed in the zero-field specific-heat measurements of β-$MgIrO_3$ (Fig. 4.9c) indicating the absence of long-range magnetic order, particularly, in the **HT**-phase. However, it's difficult to say if a broad maximum typical for spin glasses is present in the measured data. The low-temperature ($T < 5$ K) specific heat data plotted as C/T vs. T^2 can be fitted by the equation $C/T = \gamma + \beta T^2$ (Fig. 4.9d), the finite linear term was found to $\gamma = 2.4(1)$ mJ/mol K^2. However, the deviation from the linear behavior at higher temperatures suggests that some additional contributions to the heat capacity should be considered. The results of the specific heat measurements must be taken into account with caution as the magnetic **HT**-phase is only 30% of the total sample volume, and the rest is an additional contribution to the specific heat signal as the nonmagnetic **LT**-phase.

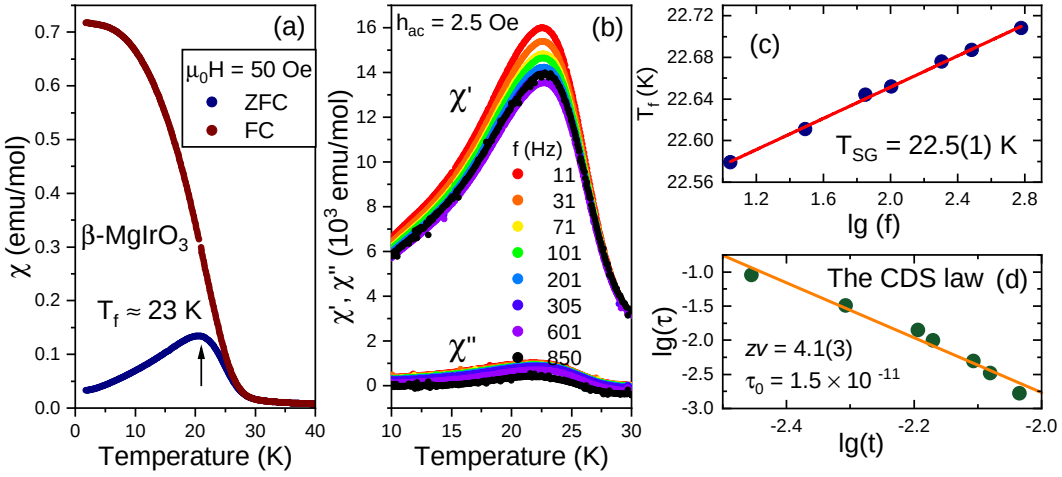

Figure 4.10: (a) Zero-field-cooled (ZFC) and field-cooled (FC) DC susceptibility data measured at 50 Oe. (b) Temperature dependence of the real (χ') and imaginary (χ'') parts of the AC magnetic susceptibility of β-$MgIrO_3$ measured at different frequencies from 11 Hz to 850 Hz in the external field of 5 Oe. The amplitude of the oscillating magnetic field is 2.5 Oe. (c) Estimation of the spin-glass transition temperature T_{SG} to the linear fit of T_f vs $\lg(f)$. (d) Frequency dependence of the freezing temperature plotted as a $\lg(\tau)$ vs $\lg(t)$, where reduced temperature $t = (T_f - T_{SG})/T_{SG}$. The solid line represents the best fit to the critical dynamic scaling law.

AC magnetization. The spin-glass-like state suggested by the bifurcation of the ZFC/FC magnetic susceptibility, was probed by AC magnetization measurements. The real part χ' shows a peak around 23 K (the anomaly in DC measurements) and, as it may be seen from Fig. 4.10b, does not demonstrate a strong frequency dependence. However, a close look at the position of the χ' peak maximum suggests another scenario. To estimate the temperature T_g of a possible spin-glass transition, AC magnetic susceptibilities at each frequency f (Hz) were fitted by a smooth curve and then differentiated. An intersection of the resulting curves with the abscissa axis was taken for the frequency-dependent freezing temperature T_f as the peak maximum of χ'. Firstly, the frequency shift in T_f is a useful criterion [66] for comparing between different spin-glass systems and distinguishing a canonical spin glass from a spin-glass-like material or a superparamagnet. The relative shift in the freezing temperature per decade of frequency denoted as δT_f (the name X is also used) can be defined as

$$\delta T_f = \frac{\Delta T_f}{T_f \Delta(\lg f)}. \tag{4.12}$$

For the **HT**-phase of β-$MgIrO_3$, this parameter was found as $\delta T_f \simeq 0.0033(13)$ that's significantly smaller then the relative shift reported for the canonical spin-glass systems (*e.g.*, $\delta T_f \sim 0.005$ for $CuMn$) indicating an unconventional nature of the spin glass (SG) in the new magnesium

iridate. Further, the value of the SG transition temperature T_{SG} was determined by extrapolating the T_f versus $\lg(f)$ plot (Fig. 4.10c), which gives $T_{SG} = 22.5(1)$ K that should correspond to the DC (equilibrium) value of T_f in the limit of $f \to 0$. Indeed, the evaluated spin-glass temperature is really close to the temperature of the susceptibility anomaly from the ZFC measurements.

An effective way to probe the system for the SG behavior is to examine if it follows the critical dynamics scaling law (CDS law) [66]; that is, the relaxation time τ diverges at T_{SG} as

$$\tau = \tau_0 \left(\frac{T_f - T_{SG}}{T_{SG}} \right)^{-z\nu}, \tag{4.13}$$

where τ is the relaxation time corresponding to the measured frequency ($\tau = 1/f$), τ_0 represents the microscopic flipping time of the fluctuating spins, T_f is the frequency-dependent freezing temperature, and $z\nu$ is called the dynamic critical exponent.

It is useful to rewrite the Eq. 4.13 as

$$\lg(\tau) = \lg(\tau_0) - z\nu \lg(t), \tag{4.14}$$

where reduced temperature $t = (T_f - T_{SG})/T_{SG}$. The slope and intercept of the plot give an estimate of τ_0 and $z\nu$, respectively. Figure 4.10d illustrates a log-log plot of the relaxation times τ versus reduced temperatures t with the fit to the CDS law. As far as one can see, the data points barely follow a linear behavior and deviate from the conventional CDS law. The best fit was obtained with $\tau_0 = 1.5 \times 10^{-11}$ s and $z\nu = 4.1(3)$. For the different spin glasses, the magnitude of $z\nu$ typically varies between about 4 and 12 [66], particularly, $6 - 8$ for the diluted systems and $10 - 12$ for the conventional three-dimensional spin glasses [163]. Meanwhile, for conventional phase transitions, $z\nu$ usually is around 2. In the case of the **HT**-phase of β-$MgIrO_3$, the value of $z\nu$ lies on the border of values for the typical SG systems, whereas the magnitude of the microscopic flipping time τ_0 is rather larger than in conventional spin glasses ($\tau_0 \sim 10^{-13\pm1}$ s), however, it is still of reasonable size. The poor fit of the frequency dependence of T_f along with the almost negligible relative shift δT_f may also be affected by the presence of the dimerized **LT**-phase that should act as a diamagnetic contribution to the measured values. Another scenario is that β-$MgIrO_3$ does not really behave as a classical spin-glass system and weakly follows the CDS law, but some sort of spin-freezing process is obvious. Nevertheless, as in the case of β-$ZnIrO_3$, the μSR measurements were performed on this compound to shed further light on the low-temperature magnetism.

4.3.2 μSR study of β-$MgIrO_3$

wTF measurements. The muon spin relaxation (μSR) experiments in the zero field (ZF) and weak transverse field (wTF) of 20 G were performed

on the GPS spectrometer at the PSI, Switzerland. Probing the local magnetism of the **HT**-phase in the presence of the large amount of the dimerized **LT**-phase may be tricky as not much research has been done for dimerized systems studied by muons so far. Nevertheless, the fraction of static spins was determined from wTF measurements by fitting the data using the same relaxation function $A_{wTF}(t)$ of Eq. 4.6 applied for the data analysis of β-$ZnIrO_3$. The fraction of static spins starts increasing below about 30 K and changes by $\sim$ 0.3 between 30 K and 10 K (Fig. 4.11a). This change corresponds to 30% fraction of the **HT**-phase in the sample, whereas the paramagnetic signal is related to the fraction of the **LT** dimerized phase similarly to the μSR study of β-Li_2IrO_3 under pressure [106]. Interestingly, the absolute values of the static and paramagnetic fraction from the wTF-μSR do not correspond to the ratio of the **HT**- and **LT**-phases in this temperature range meaning that additional static contribution is present up to 40 K and possibly at higher temperatures, probably due to an interaction of muons with the Ir–Ir dimerized bonds. Above 30 K, above the anomaly of the magnetization data, there is still some static contribution, which can be seen from the presence of fast depolarization in the wTF μSR time spectra (Fig. 4.11c). On the one hand, an incomplete transformation to paramagnetic state from the wTF fit could be the result of muon-dimer interactions as it behaves at 10 K. On the other hand, the static contribution may be explained in the view of short-range order correlations above T_{SG} as in the case of β-$ZnIrO_3$

ZF measurements. First of all, the ZF-μSR time spectra do not demonstrate well-defined oscillations (Fig. 4.11d), consistent with the absence of long-range magnetic order in β-$MgIrO_3$, and only show a small dip along with the fast depolarization part at small times. Therefore, the corresponding ZF data were fitted similarly to the frozen region of β-$ZnIrO_3$ by the sum of two functions that represent static and dynamic contributions, respectively:

$$\begin{aligned} A_{ZF}(t) &= A_1 \left[f_{st} G_z^L(t) e^{-\lambda_m t} + (1 - f_{st}) e^{-\lambda_{pm} t} \right], \\ G_z^L(t) &= \frac{1}{3} + \frac{2}{3}(1 - \lambda_L t) e^{-\lambda_L t} \end{aligned} \tag{4.15}$$

where f_{st} stands for the fraction of spins, $G_z^L(t)$ is the Kubo-Toyabe relaxation function, and λ_L is the relaxation rate describing random local fields at muon sites. The parameters λ_m and λ_{pm} are relaxation rates of the static and dynamic contributions. Similar values of f_{st} from the ZF and wTF fits confirm an internal consistency of the measured data. In this case, the static contribution expressed by $G_z^L(t)$ was described without additional modifications of the relaxation function. The ZF-μSR data identify static local fields developing below 30 K as the origin of the magnetic susceptibility anomaly at 25 K. The λ_L values that describe the width of the field distribution gradually increase upon cooling and return mean static field $\langle B \rangle = a/\gamma_\mu \simeq 168$ Oe at 5 K. The broadening of the magnetic transition suggests magnetic inhomogeneity, which is probably related to the random distribution of the Mg^{2+} ions between the octahedral and tetrahedral sites.

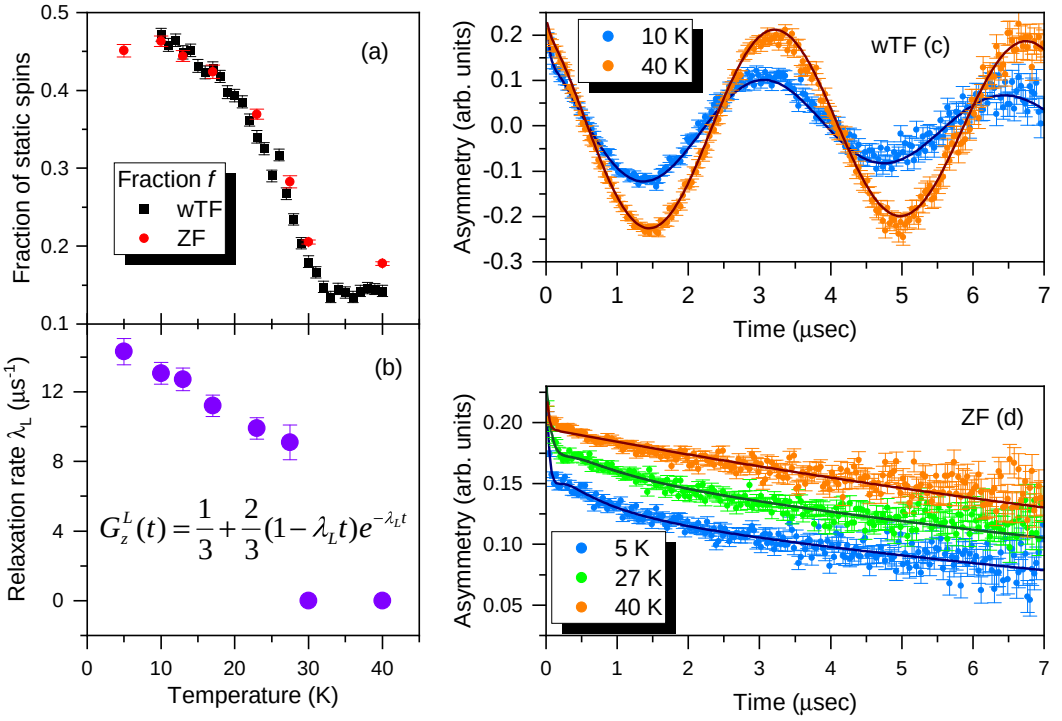

Figure 4.11: (a) Fraction of static spins from the wTF and ZF measurements on β-$ZnIrO_3$. (b) Relaxation rate λ_L as a function of temperature. (c) wTF- and (d) ZF-μSR time spectra at selected temperatures. The solid lines are the fits to the data.

Additionally, the abrupt drop in the local fields values λ_L (Fig. 4.11b) is associated with the poor fitting of the high-temperature ZF data: while the relaxation rate λ_m of the static contribution is almost temperature-independent up to 27.5 K with the average value of 1.3(2) μs^{-1}, above 30 K it increases drastically. Probably, another relaxation function should be used to properly describe the high-temperature region, but in the absence of more data points, all the ZF-μSR data were fitted by the proposed Eq. 4.15.

Despite the ambiguous interpretation of the μSR data, the main idea can still be traced: the remaining **HT**-phase demonstrates some sort of disordered magnetism which can be characterized by the development of a frozen state upon cooling.

4.4 Spin-glass transition in β-$Li_{2x}Mg_{1-x}IrO_3$

New Kitaev iridates discussed previously – β-$ZnIrO_3$ and β-$MgIrO_3$ – show a high degree of structural order along with the well reproducible magnetic properties. The situation is different with partially substituted β-$Li_{2x}Mg_{1-x}IrO_3$. As mentioned in the Chapter 3, the Li/Mg ratio was difficult to control, and

synthesized compounds demonstrated a composition, which didn't correspond to the initial one in the synthesis. Therefore, this should affect magnetic properties of the final products. Indeed, figure 4.12 illustrates the field-cooled and zero-field-cooled magnetization measurements of the samples with a different ratio of initial reagents.

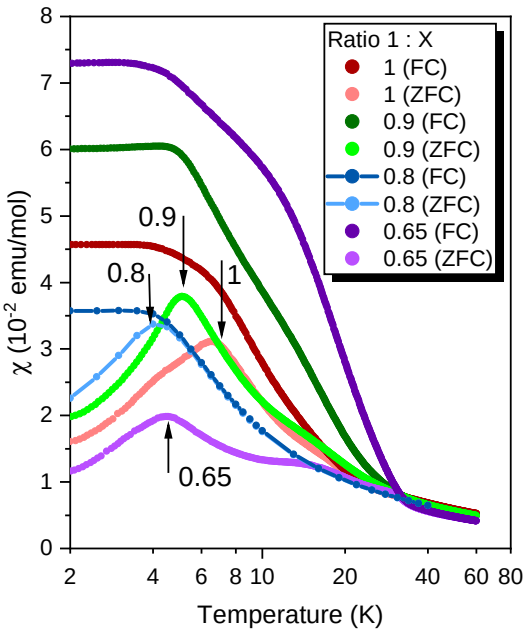

Figure 4.12: Temperature dependence of ZFC and FC susceptibilities for different starting compositions given in the molar ratio of β-Li_2IrO_3 and $Mg(NO_3)_2 \cdot 6H_2O$ as $1 : X$, measured in the field of 50 Oe. The black arrows mark a peak position in the ZFC susceptibility for each composition.

All samples show the divergence of the ZFC/FC curves below 40 K resembling glassy behavior of the fully substituted β-$MgIrO_3$. However, the magnetic susceptibility in each case is accompanied by additional features, *e.g.* a secondary peak or a stronger difference between ZFC and FC susceptibilities, that do not show any obvious dependence of magnetic properties on the degree of lithium substitution. Moreover, the measured samples could contain secondary phases or structural complexity that, for instance, was shown for two compositions with the initial ratio of reactants – 1 : 0.8 and 1 : 0.9 – in the Section 3.2.2.

Thus, study of magnetic properties in the partially substituted series β-$Li_{2x}Mg_{1-x}IrO_3$ was focused on the one well-reproducible composition with $x \simeq 0.3$ denoted as β-(Li,Mg)IrO_3 with the initial ratio of reactants as 1 : 0.8. Particularly, this compound was used for high-resolution PXRD and neutron diffraction measurements that demonstrate a well-defined crystal structure with minimum of structural ambiguity (broadened / splitted reflections).

DC magnetization measurements. In the disordered β-$MgIrO_3$, the first-order phase transition was tracked by a broad thermal hysteresis in XRD and magnetization data. In β-(Li,Mg)IrO_3, the cation disorder is much more pronounced and associated with the additional random distribution of Mg and Li atoms between the tetrahedral and octahedral positions. However, no structural transition was detected by high-resolution PXRD measured in a wide temperature range. The bulk DC magnetization illustrated by Fig. 4.13a indicates the absence of any phase transformation as well, and the susceptibility curves measured upon cooling and warming perfectly overlap (for instance, in the field of 1 T). Inverse susceptibility can be nicely fitted using the Curie-Weiss law down to 50 K (Fig. 4.13b). The calculated effective moment

of 1.67(2) μ_B corresponds to the $j_{eff} = \frac{1}{2}$ state of Ir^{4+}, however, the absolute value is lower than for the fully substituted β-$ZnIrO_3$ and β-$MgIrO_3$. The Curie-Weiss temperature Θ_{CW} of $-16.0(3)$ K is now antiferromagnetic, but the same order of magnitude as in other β-$MIrO_3$ compounds. β-(Li,Mg)IrO_3 further shows an anomaly around 5 K which in small field manifests itself by an irreversibility of the field-cooled and zero-field-cooled data.

The isothermal magnetization measured at 2 and 10 K (Fig. 4.14a) shows no hysteresis loop but a steady non-linear increase with no sign of saturation up to 7 T. Even in high-fields measurements (the inset in Fig. 4.14a), the magnetization does not reach the saturation plateau. Figure 4.14b shows the temperature dependence of the heat capacity divided by temperature C/T up to 35 K. No sharp anomalies as indication of a long-range order were observed in the presented data, however, a broad peak around $T_{max} \sim 6$ K can be seen in the absence of field. A close look at the low-temperature range reveals a second anomaly at lower temperatures, a kink in C/T at $T_a \sim 2.5$ K (Fig. 4.14c). While the broad hump at T_{max} can be referred to the spin-glass behavior as a shift of the freezing temperature (a broad maximum $20-40$ percent above T_f [66, 67]), the origin of the second anomaly at T_a remains unknown. In the applied magnetic fields, these anomalies are mostly suppressed. Interestingly, the low-temperature specific-heat data do not follow the power law $C(T) = \gamma T + \beta T^3$ temperature dependence as can be seen from the C/T versus T^2 plot (Fig. 4.14d) indicating the presence of an additional contribution to the specific heat.

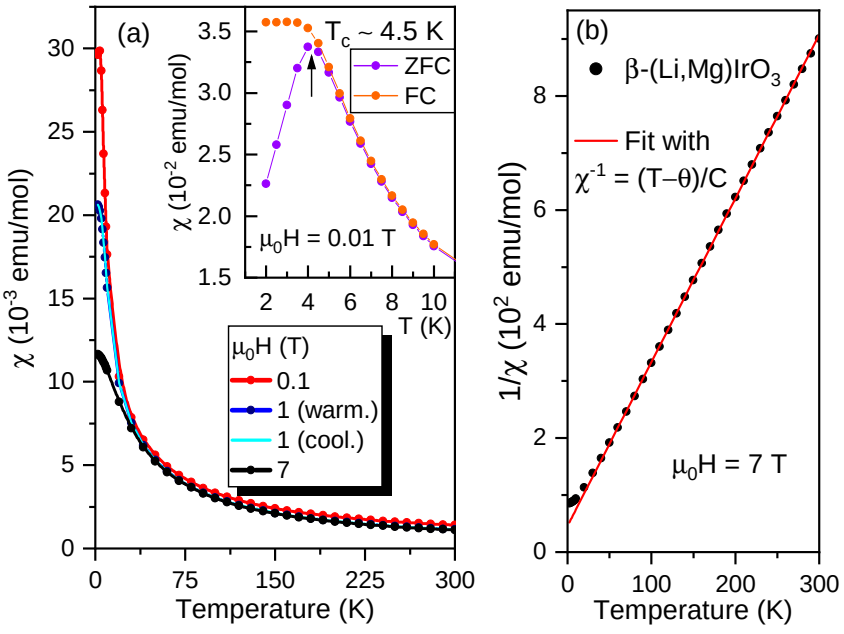

Figure 4.13: (a) Temperature-dependent magnetic susceptibility $\chi(T)$ of β-(Li,Mg)IrO_3 measured in various magnetic fields. At 1 T, the susceptibility curves upon cooling and warming are fully overlapped. The inset shows the splitting of the magnetization curves in the ZFC and FC regimes below 5 K. (b) Inverse magnetic susceptibility with the fit to the Curie-Weiss law at 7 T.

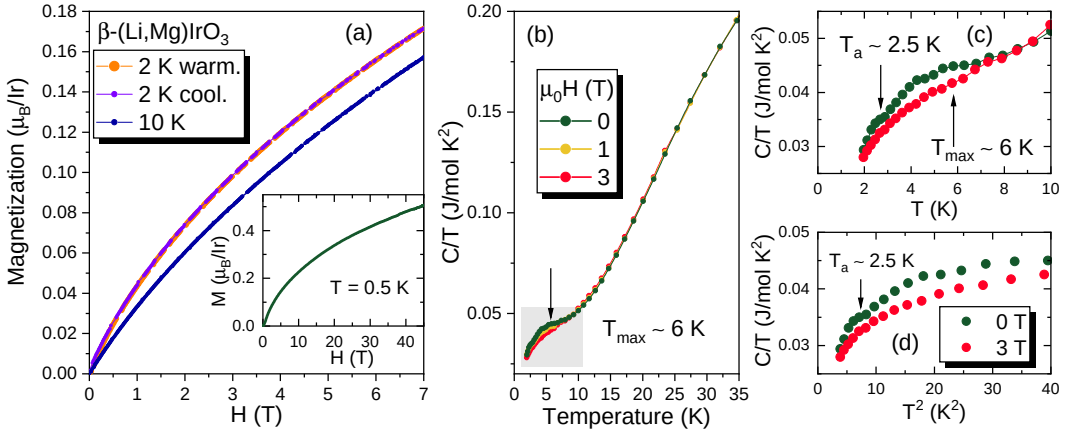

Figure 4.14: (a) Magnetization curves of β-(Li,Mg)IrO_3 at 2 and 10 K. The orange and purple dots are the data taken at 2 K upon warming and cooling, respectively. The inset shows the high-filed isothermal magnetization $M(H)$ at 0.5 K. (b) Temperature dependence of the specific heat divided by temperature C/T in zero magnetic field, and at 1 and 3 T. The black arrow marks an anomaly at T_{max}. (c) Enlarged view of C/T between 2 and 10 K (the shaded area in (b)). Two anomalies at 2.5 and 6 K are labeled. (d) C/T versus T^2 plots up to 7 K at zero magnetic field and 3 T.

AC magnetization measurements. Splitting of the ZFC/FC susceptibility curves below the anomaly temperature T_f as well as a broad peak at slightly higher temperatures in the specific heat imply spin-glassy behavior, now in the case of the partially substituted β-(Li,Mg)IrO_3. Moreover, the FC magnetization almost remains temperature independent below 5 K that is also a feature of canonical spin glasses. Applying the same measurement procedure that was used for β-$MgIrO_3$, the spin-glass transition in β-(Li,Mg)IrO_3 was studied by AC magnetization measurement.

First of all, the real χ' and imaginary χ'' parts of the AC magnetic susceptibility exhibit pronounced anomalies: the amplitude and peak position of which strongly depend on the excitation frequency, and the position of the maxima increases with the increasing frequency (Fig. 4.15a-b). Such behavior of $\chi'(T)$ and $\chi''(T)$ is the characteristic feature of a spin-glass ordering and hence indicates a spin-glass-type transition in β-(Li,Mg)IrO_3 with a freezing temperature $T_f \sim 4.5$ K. The relative shift of the freezing temperature calculated by the Eq. 4.12 was found as $\delta T_f = 0.032(3)$, which is five times larger than the relative shift for the diluted spin glasses (*Cu*Mn, *Au*Mn) and an order of magnitude smaller than for a superparamagnet (*e.g.*, $\delta T_f = 0.28$ for a-(Ho_2O_3)(B_2O_3) [66]). However, the magnitude of δT_f is comparable to that of insulating spin glasses [69, 70] and characterizes β-(Li,Mg)IrO_3 as the so-called cluster glass. The spin-glass transition temperature determined by the linear fit of the frequency dependence of T_f corresponds to $T_{SG} = 4.51(2)$ K (Fig. 4.15c).

In contrast to the fully substituted magnesium iridate, β-(Li,Mg)IrO_3 can be much better described by the critical dynamics scaling law using the equations 4.13 and 4.14. The best fit was obtained with $\tau_0 = 7.0 \times 10^{-8}$ s and

$z\nu = 4.3(1)$ (Fig. 4.15d). The value of $z\nu$ is consistent with the spin-glass behavior in β-(Li,Mg)IrO_3. However, the microscopic flipping time τ_0 is significantly large compared to the canonical spin-glass systems suggesting a slow spin dynamics in β-(Li,Mg)IrO_3, likely due to the presence of strongly interacting clusters rather than individual spins.

Another route to describe the spin-glass transition through AC magnetization measurements is the analysis by the empirical Vogel-Flucher law (VFL) [66, 164] originally proposed for describing the viscosity of supercooled liquids or real glasses [165, 166]. Now, the frequency dependence of the freezing temperature T_f can be described in terms of the VFL as

$$f = f_0 \exp\left(-\frac{E_a}{k_B(T_f - T_0)}\right), \tag{4.16}$$

where k_B is the Boltzmann constant, f_0 stands for the characteristic attempt frequency, E_a is the average thermal activation energy, and T_0 is a new parameter – the Vogel-Fulcher temperature, which is often interpreted as a measure of intercluster interaction strength. For different spin glasses, the value of T_0 is usually lower than the transition temperature T_{SG}. The estimation of three variable parameters f_0, E_a, and T_0 can be done in two different ways, both of which give consistent values of these parameters. The first one is fixing the value of attempt frequency to $f_0 = 1/\tau_0$, the microscopic flipping time $\tau_0 = 7.0 \times 10^{-8}$ s as determined from the CDS law fit. In order to get the linear behavior of the freezing temperature T_f, it is convenient to rewrite the equation 4.16 as

$$\ln\left(\frac{f_0}{f}\right) = \frac{E_a}{k_B(T_f - T_0)},$$

which can be rearranged to

$$T_f = \frac{E_a/k_B}{\ln(f_0/f)} + T_0. \tag{4.17}$$

Thus, E_a/k_B and T_0 can be estimated from the slope and intercept of the semi-logarithmic plot shown in Fig. 4.15e-f. The value of Vogel-Fulcher temperature $T_0 (< T_{SG}) = 4.03(3)$ K and the activation temperature $E_a/k_B = 9.1(3)$ K were obtained from the fit. The other way to determine the key parameters of the VFL is to independently calculate T_0 by following the method suggested by Souletie and Tholence [164] in order to avoid inconsistencies due to fixing the attempt frequency f_0. The Vogel-Fulcher temperature was found as $T_0 = 3.95$ K and then used to find E_a and $\tau_0 = 1/f_0$. By rearranging the equation 4.16 as

$$\ln(f) = \ln(f_0) - \frac{E_a/k_B}{T_f - T_0}, \tag{4.18}$$

the characteristic parameters were estimated as $\tau_0 = 2.24 \times 10^{-8}$ s and

$E_a/k_B = 11.1(4)$ K that are in a good agreement with the previously estimated activation energy and characteristic relaxation time. Thus, the Vogel-Fulcher temperature T_0 is nonzero indicating the formation of spin clusters in β-(Li,Mg)IrO_3 and suggesting a cluster spin-glass behavior.

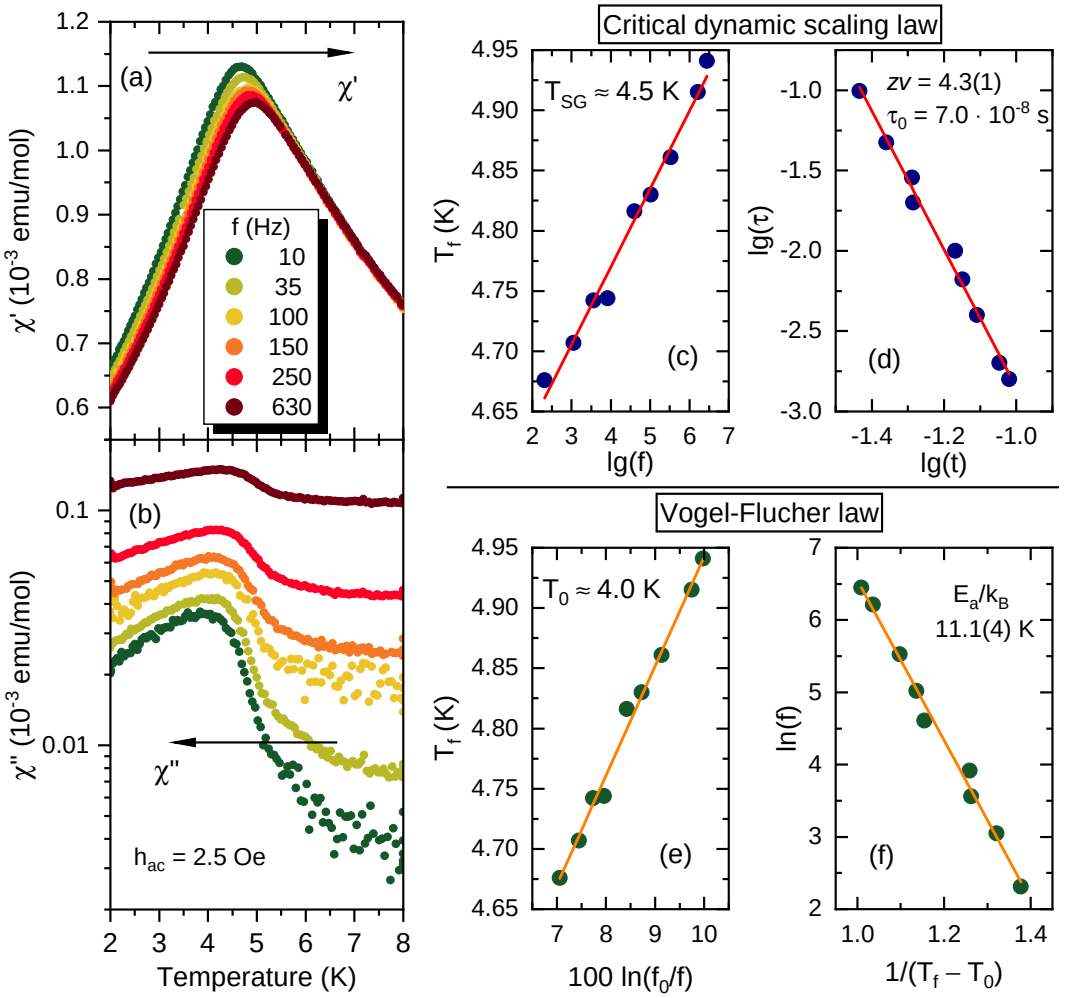

Figure 4.15: Temperature-dependent real $\chi'(T)$ (a) and imaginary $\chi''(T)$ (b) parts of the AC magnetic susceptibility of β-(Li,Mg)IrO_3 measured at different frequencies from 10 Hz to 630 Hz in the external field of 10 Oe. The amplitude of the oscillating magnetic field is 2.5 Oe. CDS law fits plotted as frequency dependence of the freezing temperature (T_f vs $\lg(f)$) (c), and frequency dependence of the reduced temperature ($\lg(f)$ vs $\lg(t)$) (d). Vogel-Fulcher law fits plotted as T_f vs $100\ \ln(f_0/f)$ at the constant attempt frequency $f_0 = 1/\tau_0$ (e), and $\ln(f)$ vs $1/(T_f - T_0)$ at the constant VF temperature $T_0 = 3.95$ K (f).

4.5 β-MIrO$_3$: tendency to spin-freezing?

Achieving the quantum spin-liquid state in the Ir-based compounds initiated the research in the way of chemical substitution of the parent sodium and lithium iridates. However, most of these modified materials still show the long-range magnetic order, or demonstrate disordered magnetism of some sort. Unfortunately, the new Kitaev iridates – β-ZnIrO$_3$, β-MgIrO$_3$ and β-(Li,Mg)IrO$_3$ – have also failed to become true spin liquids and also show disordered ground state.

In contrast to the magnetically ordered α-ZnIrO$_3$ and α-ZnIrO$_3$ compounds, the new Kitaev iridates with the hyperhoneycomb structure do not demonstrate the LRMO. Although the magnetic order is suppressed in β-MIrO$_3$ in contrast to the parent compound β-Li$_2$IrO$_3$, the short-range order correlations intensively develop below critical temperatures. In the case of partially and fully substituted magnesium iridates, freezing processes are pronounced, leading to the conventional spin-glass transition in β-(Li,Mg)IrO$_3$, which is hitherto rare in Kitaev magnets [31]. In the case of β-ZnIrO$_3$, spins seem to gradually freeze with temperature lowering, however, there is no sign of the spin-glass transition. Instead, the system shows a coexistence of static and dynamic spins at the lowest temperatures. Moreover, the random local fields in β-ZnIrO$_3$ are not associated with completely frozen moments, but lead to some sort of slowly fluctuating state.

Table 4.1: Comparison of parent iridates and their derivatives, as well as new Kitaev iridates: effective magnetic moment μ_{eff}, Curie-Weiss temperature θ_{CW}, critical temperature T_C (*i.g.* T_{N} or spin-glass transition T_{SG}), mean value of the Ir–O–Ir angle Θ, and unit cell volume V per formula unit. The asterisk denotes the lowest measured temperature for $H_3LiIr_2O_6$.

Compound	μ_{eff} (μ_{B})	θ_{CW} (K)	T_{C} (K)	Θ (deg)	V (Å^3)	Ref.
α-Li$_2$IrO$_3$	1.83	-70	~ 15	91.1	55.68	[86]
β-Li$_2$IrO$_3$	1.7–2.0	$+21$	$\simeq 38$	94.6	55.69	[97, 98]
Cu$_2$IrO$_3$	1.93	-110	2.7	98.2	71.37	[131]
$H_3LiIr_2O_6$	1.60	-105	0.05*	99.5	56.07	[135]
α-MgIrO$_3$	1.73	-67.1	31.8	94.0	53.46	[138]
α-ZnIrO$_3$	1.73	-47.5	46.6	95.7	54.20	[138]
β-ZnIrO$_3$	1.81(1)	$+12.4$	~ 5	96.2	57.82	This work
β-MgIrO$_3$	1.89–1.92	$+56$	22.5	95.5	57.54	This work
β-(Li,Mg)IrO$_3$	1.67(2)	-16	4.51	95.8	56.92	This work

Ionic exchange in β-Li$_2$IrO$_3$ by Zn^{2+} and Mg^{2+} expands the unit cell with the increase of the Ir–Ir bond lengths and Ir–O–Ir angles (Table 4.1) that should push the new β-MIrO$_3$ compounds closer to the Kitaev limit.

In fact, presence of the non-equivalent tetrahedral and octahedral positions of the non-magnetic cations also affect the magnetic properties in the new Kitaev iridates emphasizing the influence of structural disorder for the QSL candidates. The partially substituted β-(Li,Mg)IrO_3 demonstrates randomness of the Li and Mg positions which undoubtedly affects the local environment of Ir atoms on the hyperhoneycomb lattice leading to the conventional spin-glass state. The less disordered β-$MgIrO_3$ still develops a spin-freezing tendency, but less pronounced that leads to the non-canonical SG state. Finally, β-$ZnIrO_3$ shows a high degree of structural order without site mixing or partially occupied positions. However, the strong anisotropy of the Ir–Ir bonds and non-uniform local environment of the IrO_6 octahedra lead away from the spin-liquid state that results as short-range order correlations and the magnetically disordered ground state in β-$ZnIrO_3$.

Additionally, the random distribution of the Mg^{2+} ions between the octahedral and tetrahedral sites in β-$MgIrO_3$ also results in an unconventional glassy state below 30 K. But what is more interesting, this causes the unexpected first-order phase transition associated with the structural dimerization and magnetic collapse of the **LT**-phase. Chemical substitution acting as negative pressure still destabilizes magnetism in β-$MgIrO_3$. Therefore, a logical question arises: how would β-$MgIrO_3$ exhibit a *magnetic–dimerized* phase transition upon compression? The high-resolution PXRD experiments as well as magnetization measurement performed under external pressure would shed some light on it, and the results of these measurements will be discussed in the next chapter.

Chapter 5

Magnesium iridates under pressure

5.1 Methods

High-resolution PXRD. A small sample of the β-MIrO$_3$ powder was loaded into a diamond anvil cell (DAC) for pressure generation, and helium was used as pressure transmitting medium. The powder x-ray diffraction patterns were obtained using synchrotron radiation at the beamline ID15B at the European Synchrotron Radiation Facility (ESRF), Grenoble at $T = 100$ K and room temperature. A Eiger2 9 M CdTe (DECTRIS) detector and a wavelength of 0.41055 Å were used. The pressure in the DAC was determined *in situ* by the ruby luminescence method. Additional high-pressure XRD experiments performed on the extreme condition beamline P02.2 at PETRA III (DESY) in Hamburg using a Perkin Elmer XRD1621 area detector and a wavelength of 0.2902 Å. The pressure was determined by the shift of the ruby luminescence line.

The resulting two-dimensional (2D) x-ray images were integrated using the Dioptas program [167]. The collected data were analyzed by Le Bail and Rietveld refinements using the Jana2006 software [144].

Magnetization measurements. Magnetization measurements under applied pressure were performed by Bin Shen at Institute of Physics, University of Augsburg (Augsburg, Germany). Magnetization was measured using the MPMS3 SQUID magnetometer from Quantum Design. The powder samples were loaded into an opposed-anvil-type CuBe pressure cell. Measurements of β-MgIrO$_3$ were carried out with a 1.8-mm anvil culet and a gasket with the sample space diameter of 0.9 mm. In this case, pressures up to 1.8 GPa could be reached. Higher pressures, up to 2.1 GPa, were achieved in the case of β-(Li,Mg)IrO$_3$ with a 1-mm anvil culet and a gasket with the sample space diameter of 0.5 mm. Daphne oil 7373 was used as the pressure-transmitting medium. Pressure was determined by measuring the superconducting transition of a small piece of Pb. Magnetization of the empty cell was taken as the background.

Pressure was applied at room temperature. The data were collected upon cooling up to 4 K and then upon warming to room temperature. Then the pressure was increased at room temperature, and the procedure was repeated until the highest pressure feasible with the current gasket was reached.

5.2 Irreversible pressure-induced dimerization in β-$MgIrO_3$

β-$MgIrO_3$ demonstrates an unusual structural and magnetic behavior at ambient pressure: it undergoes a first-order phase transition upon cooling accompanied by a magnetic collapse due to formation of the shortened Ir–Ir bonds of ~ 2.67 Å in the dimerized **LT**-phase. Such a tendency to dimerization probably means that an application of external pressure will also lead to the structural transition from magnetic to non-magnetic state at relatively small pressure values.

Compression. Indeed, a stability region of the **HT**-phase of β-$MgIrO_3$ ends at $P_{d1} \simeq 1.5$ GPa (dimerization pressure) above which the coexistence of **HT**- and **LT**-phases is observed at room temperature (Fig. 5.2a). However, the *pressure*-induced structural transition is complete in contrast to the β-$MgIrO_3$ transformation upon cooling and warming at ambient pressure, and above $P_{d2} \simeq 2.7$ GPa the system converts into the **LT**-phase that can be tracked by suppression of the reflections of the magnetic phase above P_{d2} (Fig. 5.1a) and **HT**/**LT** fraction ratio obtained from the Rietveld refinement of the PXRD data (see the inset in Fig. 5.2b). **NB**: preservation of the **HT**/**LT** notation for the magnetic and dimerized phases is caused by the identity of the phase transition upon compression and cooling. As will be shown below, pressure dependence of the lattice parameters and Ir–Ir bond distances of β-$MgIrO_3$ follows the same way as temperature one.

First, a small volume collapse is observed across the phase boundaries, reaching $\sim -1.09\%$ trough the **HT**/**LT** phase transition (Fig. 5.2) that is in a good agreement with the temperature-induced dimerization (the reduced volume by $\sim -1.27\%$ at 1.5 K, Section 3.2.3). Similar volume collapses have been observed in β-Li_2IrO_3 at 300 K [116, 168] ($\sim -0.7\%$ at the $Fddd \rightarrow C2/c$ transition).

Second, the main contribution to the volume reduction is caused by the anisotropic behavior of the lattice parameters of the **LT**-phase. While the lattice constants of the **HT**-phase decrease linearly with pressure, the c parameter of the dimerized phase has a stronger pressure dependence than its a and b counterparts (Fig. 5.2b). Upon transition to the **LT**-phase ($P_{d1} \simeq 1.5$ GPa), a remarkable expansion of the a ($\sim 2.1\%$) and b ($\sim 1.6\%$) lattice parameters is observed, whereas the c axis is compressed drastically ($\sim -3.7\%$) followed by a monotonic decrease with pressure. Compression rates of the **HT**- and **LT**-phases listed in Table 5.1 additionally highlight an anisotropic behavior of the lattice constants and unit cell volume.

Third, this anisotropic behavior also affects the changes of the Ir–Ir bonds in both phases. A complete description of the evolution of the Ir-Ir bond distances across the phase boundaries is shown in Fig 5.2c. Despite the preferred orientation that affected the accuracy of the extracted Ir–Ir distances, the main features are clearly distinguishable. Above 1.5 GPa, $\frac{1}{3}$ of the bonds

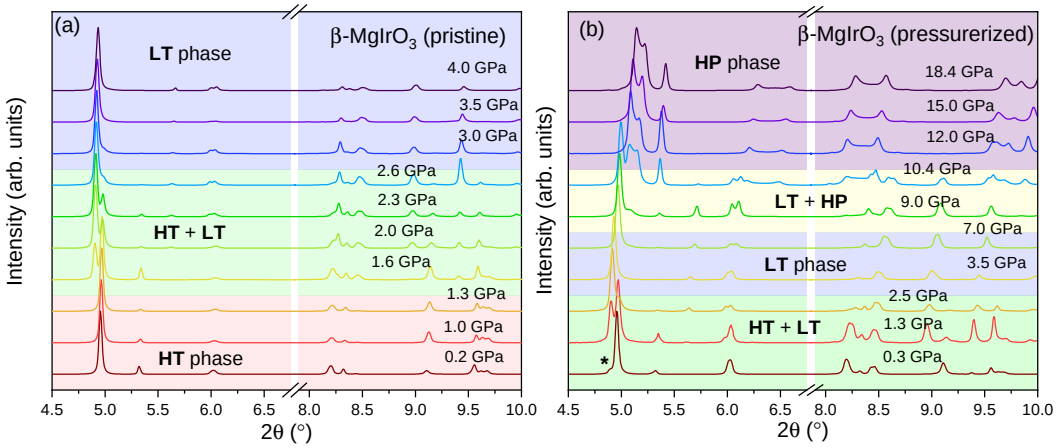

Figure 5.1: Powder x-ray diffraction patterns of the pristine (a) and pressurized (b) β-$MgIrO_3$ as a function of pressure at $T = 300$ K. (a) Between $1.5 - 2.7$ GPa, a coexistence of the **HT**- and **LT**-phases is observed. (b) Asterisk marks the presence of the **LT**-phase at $P \simeq 0.3$ GPa.

is drastically shortened up to $\approx 2.66 - 2.7$ Å as a consequence of faster contraction of the c lattice parameter, indicating formation of the Ir–Ir dimers along the Z-bond between two iridium zigzag chains (Fig. 5.2d), whereas the X- and Y-bonds are slightly lengthened. Such bond separation in length is an evidence of dimerization process in the **LT**-phase of β-$MgIrO_3$, and the behavior of the lattice constants along with differentiation of the XYZ-bonds under applied pressure corresponds to the dimerization of β-$MgIrO_3$ upon cooling.

Table 5.1: Compression rates of the lattice parameters and volume for each identified structure at $T = 300$ K upon compression of the pristine and pressurized β-$MgIrO_3$. The compression rate is defined as $\frac{\frac{x-x_0}{x_0}}{p-p_0}$, where $x(x_0)$ is the final (initial) parameter and $p(p_0)$ is the final (initial) pressure for each phase boundary. All values are in units of %/GPa.

Phase	$\frac{\Delta a/a_0}{\Delta P}$	$\frac{\Delta b/b_0}{\Delta P}$	$\frac{\Delta c/c_0}{\Delta P}$	$\frac{\Delta V/V_0}{\Delta P}$
HT-$MgIrO_3$ (pristine)	$-0.33(3)$	$-0.23(3)$	$-0.16(2)$	$-0.67(3)$
LT-$MgIrO_3$ (pristine)	$-0.14(3)$	$-0.21(4)$	$-0.28(5)$	$-0.63(1)$
LT-$MgIrO_3$ (pressurized)	$-0.16(2)$	$-0.23(1)$	$-0.20(1)$	$-0.58(2)$
HP-$MgIrO_3$ (pressurized)	$-0.12(2)$	$-0.14(1)$	$-0.14(1)$	$-0.42(2)$

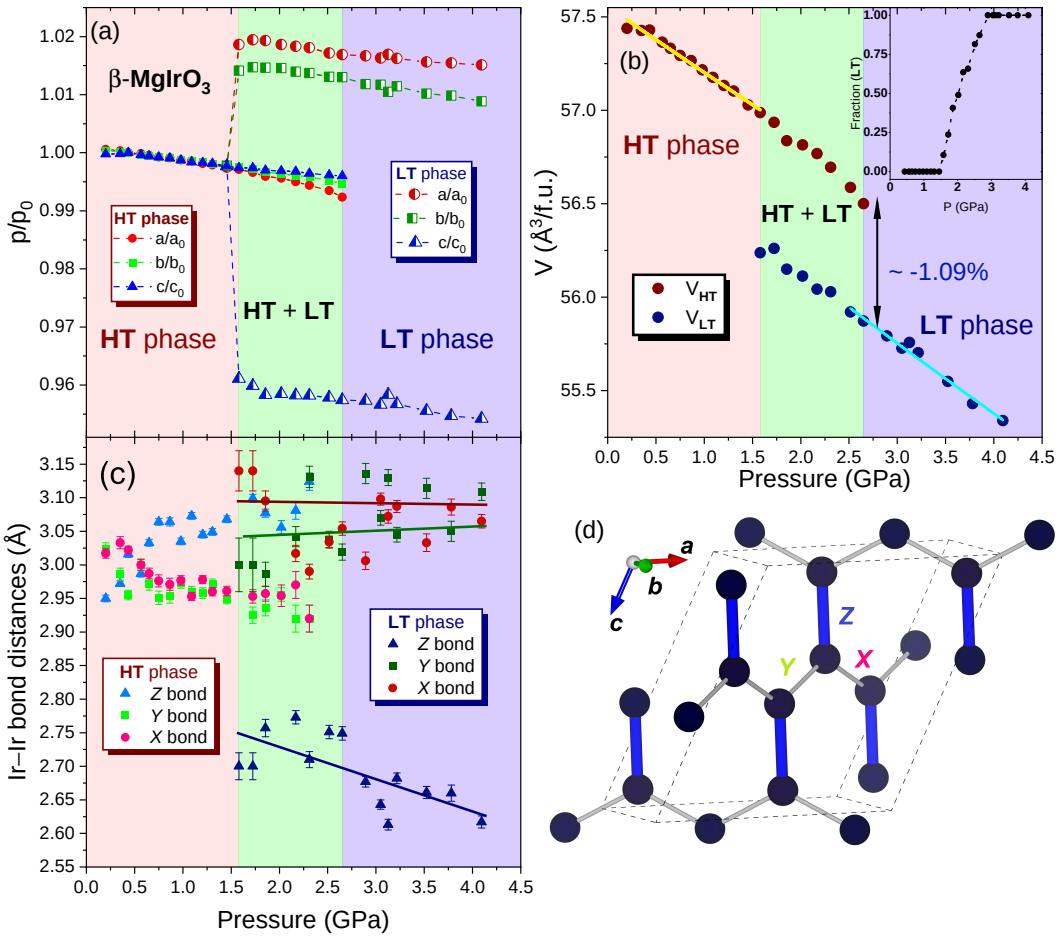

Figure 5.2: (a) Lattice parameters of β-$MgIrO_3$ at $T = 300$ K as a function of pressure measured upon compression. All lattice constants are normalized to the parameters at the lowest pressure of 0.2 GPa. (b) Pressure-volume relationship of β-$MgIrO_3$ at $T = 300$ K. The solid lines are fits with the second-order Murnaghan equation of state (see text). The inset shows the volume fraction of the **LT**-phase as a function of pressure. (c) Pressure dependence of the Ir–Ir bond distances for the **HT**- and **LT**-phases in the XYZ-bond notation at $T = 300$ K. If not shown, the error bar is smaller than the symbol size. The solid lines are guides for the eye. (d) Hyperhoneycomb network of Ir atoms in the **LT**-β-$MgIrO_3$ with the corresponding bond labeling. The direction of dimerization – the Z-bond – is colored in blue.

Pressurized β-$MgIrO_3$. However, the *pressure*-induced phase transition was not fully reversible meaning that once the β-$MgIrO_3$ was pressurized and transformed into the dimerized **LT**-phase, its return to the magnetic **HT**-phase upon decompression was incomplete and accompanied by a pressure hysteresis. Even at $P = 0.29$ GPa ($T = 300$ K), that is 5 times smaller than the dimerization pressure P_{d1}, there are small (roughly 2% of the volume fraction) but visible traces of the dimerized phase in the β-$MgIrO_3$ sample. Therefore, *pristine* β-$MgIrO_3$ means the sample previously not affected by the pressure, and *pressurized* β-$MgIrO_3$ stands for the sample which has already been compressed.

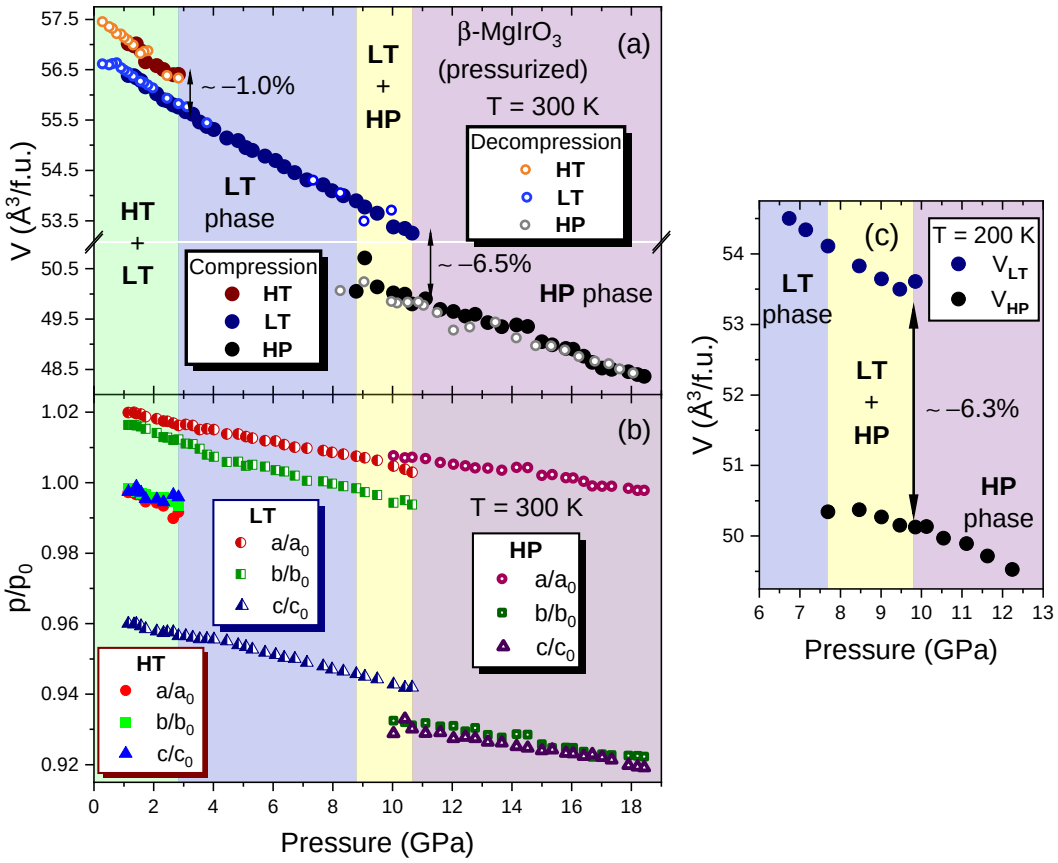

Figure 5.3: Pressure dependence of the volume (a) and lattice parameters (b) of the pressurized β-$MgIrO_3$ at $T = 300$ K measured upon compression. Additionally, the volume of the **HT**-, **LT**- and **HP**-phases of β-$MgIrO_3$ upon decompression is given (a). All lattice constants are normalized to the parameters at the lowest pressure of ~ 0.3 GPa. (c) Pressure-volume relationship of β-$MgIrO_3$ at $T = 200$ K measured upon compression.

Nevertheless, application of external pressure to the pressurized sample reveals the completion of the phase transition from the **HT**- to the **LT**-phase at $P \simeq 2.8$ GPa and a small volume discontinuity ($\sim -1.0\%$) that is consistent with results of the phase transition for the pristine β-$MgIrO_3$. Interestingly, above $P_{d3} = 8.8$ GPa another phase transition can be detected by the significant volume collapse ($\sim -6.5\%$) and a symmetry lowering. As mentioned

above, the sample shows signs of texturing, and subsequent data processing was done only by profile (Le Bail) fitting without the crystal structure determination. The best profile refinement of the new high-pressure (**HP**) phase of β-$MgIrO_3$ could be performed in the triclinic space group $P\bar{1}$. The second phase transition is characterized by the narrow region of the **LT**/**HP**-phase coexistence ($\simeq$ 1.9 GPa), and above $P_{d4} = 10.7$ GPa only the high-pressure phase remains (Fig. 5.1b). Whereas the unit cell angles (α, β and γ) of the **HP**-phase slightly deviate from the parameters of the **LT**-phase (see Table 5.2), the lattice constants are strongly affected by the pressure: enormous compression of $\sim -6.8\%$ in the b direction unlike the minor changes of the a ($\sim 0.3\%$) and c ($\sim -1.4\%$) lattice parameters. An anisotropic contraction of the lattice constants is seen for most phases (see Table 5.1). The reason of such a drastic volume reduction of the **HP**-phase may be a subsequent dimerization of one of the Ir–Ir bonds (X or Y) within the zigzag chain in addition to the already shortened Z bond. For instance, the remarkable compression along the b axis in β-Li_2IrO_3 above 4.5 GPa leads to the dimerization of the Y-bond in the $C2/c$ phase [116, 168]. Similar correlations between lattice contraction and bond dimerization may also take place in the case of the **HP**-$MgIrO_3$.

In addition, the pressure dependencies of the volume V and lattice parameters r ($r = a, b, c$) at room temperature were fitted separately for the **HT**- and **LT**-phases with a second-order Murnaghan equation of state (EoS) [169] to obtain the bulk moduli $B_{0,V}$ and $B_{0,r}$ according to

$$V(P) = V_0 \left[\left(\frac{B_0'}{B_{0,V}} \right) P + 1 \right]^{-1/B_0'}, \tag{5.1}$$

$$r(P) = V_0 \left[\left(\frac{B_0'}{B_{0,r}} \right) P + 1 \right]^{-1/3B_0'}, \tag{5.2}$$

with B_0' fixed to 4. The data in the phase coexistence regions were excluded to avoid ambiguities caused by the two-phase refinement. The results are summarized in Table 5.3. For the **HT**-phase, the bulk modulus was found as $B_{0,V} \approx 160(6)$ GPa that is a significantly large value compared to the other (hyper)honeycomb iridates, such as α-Li_2IrO_3 (106 GPa) [113] and β-Li_2IrO_3 (100 GPa). Additionally, the bulk moduli $B_{0,r}$ related to the cell parameters are anisotropic with the highest value $B_{0,c} = 170(11)$ GPa along the c direction. For the pristine **LT**-$MgIrO_3$, the bulk moduli $B_{0,r}$ were calculated with less accuracy due to a limited number of data sets below $P_{d2} \simeq 2.7$ GPa. Therefore, the calculated parameters from the EoS fit were considered for the pressurized **LT**-$MgIrO_3$. On the one hand, the bulk modulus $B_{0,V}$ slightly decreases to $\approx 152(2)$ GPa. On the other hand, the bulk moduli $B_{0,V}$ of the **HT**- and **LT**-phases are merely the same within the error bar, however, the dimerized **LT**-phase was found to be stable up to $P_{d3} \sim 8.8$ GPa. The bulk modulus $B_{0,b}$ is lower among others for the cell parameters, thus **LT**-phase is more compressible along the b direction. Further compression leads to a transition into the **HP**-phase of β-$MgIrO_3$ accompanied by the drastic reduction of the b parameter; above $P_{d4} = 10.7$ GPa the bulk modulus increases to $B_{0,V} \approx 185(8)$ GPa, while $B_{0,b}$ and $B_{0,c}$ are almost the same.

Table 5.2: Lattice parameters and unit cell volume per formula unit of β-$MgIrO_3$ at $T = 300$ K. Lattice constants of the **HT**-phase (at 1.5 GPa) are given for the pristine sample, parameters of the **LT**-phase (at 8.4 GPa) and the **HP**-phase (at 18.4 GPa) are listed for the pressurized sample.

Phase	a (Å)	b (Å)	c (Å)	α (deg.)	β (deg.)	γ (deg.)	V (Å^3)
HT ($C2/c$)	8.6903(4)	5.9554(3)	9.8027(6)	90	115.94(1)	90	57.03(1)
LT ($C2/c$)	8.7825(4)	5.9626(3)	9.2992(4)	90	117.49(1)	90	54.00(1)
HP ($P\bar{1}$)	8.6928(6)	5.5044(4)	9.0316(5)	89.93(1)	116.44(1)	88.97(1)	48.36(1)

Table 5.3: Equilibrium volume V_0 per formula unit, bulk moduli $B_{0,V}$ and $B_{0,r}$, with $r = a, b, c$, in the **HT**-, **LT**- and **HP** phases of β-$MgIrO_3$, as obtained from fitting the volume V and lattice parameters r with the second-order Murnaghan equation of state (EoS), with B_0' set to 4. The fits were performed for the data collected at room temperature.

Phase	V_0 (Å^3)	$B_{0,V}$ (GPa)	$B_{0,a}$ (GPa)	$B_{0,b}$ (GPa)	$B_{0,c}$ (GPa)
HT (pristine)	57.56(1)	160(6)	130(3)	157(3)	170(11)
LT (pristine)	56.97(5)	133(6)	211(25)	111(10)	126(24)
LT (pressurized)	56.73(2)	152(2)	193(5)	127(6)	143(5)
HP (pressurized)	52.61(14)	185(8)	226(12)	172(11)	174(12)

Despite the pressure hysteresis between the measurements of the pristine and pressurized samples, no significant differences in the phase boundaries and volume changes in the pressure range from 2 to 12 GPa were found upon compression and decompression of the *pressurized* β-$MgIrO_3$ (Fig. 5.3a).

In addition, the offset of the second phase transition from the **LT** to **HP**-phase was observed at $T = 200$ K (Fig. 5.3c). While the boundaries of the phase mixture are shifted to the lower pressure values of 7.7 and 9.9 GPa, its width remains unaffected by pressure.

$P - T$ phase diagram. In addition to the isothermal experiments upon compression/decompression, the isobar measurements at $P \simeq 0.6$ GPa were performed on the pristine β-$MgIrO_3$ at PETRA III (DESY). The relevant information about the phase fractions is illustrated in Fig. 5.4a. In the compressed sample, the phase transition from the **HT**- to **LT**-phase upon cooling occurs at a higher temperature ($T_d^{cool} \sim 180$ K at ambient pressure vs $T_d^{cool} \sim 240$ K at 0.6 GPa), but still doesn't demonstrate a full transformation into the dimerized state at low temperatures. The width of the thermal hysteresis appears to remain unaffected by pressure and reaches around 100 K. Therefore, at

0.6 GPa the transformation of the **LT**-phase into the **HT**-phase is not complete even at 300 K, the highest temperature reached in our measurements, while at ambient pressure the **LT**-phase disappears above $T_d^{warm} \sim 280$ K (Fig. 5.4a-c).

Compression experiments along with temperature-dependent PXRD study revealed a remarkably complex *pressure-temperature* (P-T) phase diagram for β-$MgIrO_3$. Therefore, two independent cases in the view of $P-T$ diagram should be considered here. The first one is when the pristine β-$MgIrO_3$ is examined upon cooling and compression (Fig. 5.4b). A remarkable feature of this case is a broad region of phase coexistence: even at sufficiently low temperatures, there is still a small fraction of the magnetic **HT**-phase in a wide range of pressures. The pressure-dependent magnetization measurements (Fig. 5.5a) revealed a noticeable magnetic response due to the presence of the **HT**-phase, even at 1.6 GPa. Moreover, the spin-glassy behavior of β-$MgIrO_3$ seems to persist under pressure. In ZFC/FC measurements in small fields, a bifurcation of the susceptibility curves originates below 30 K at any pressure without a shift of the spin-glass temperature T_{SG} (Fig. 5.5b).

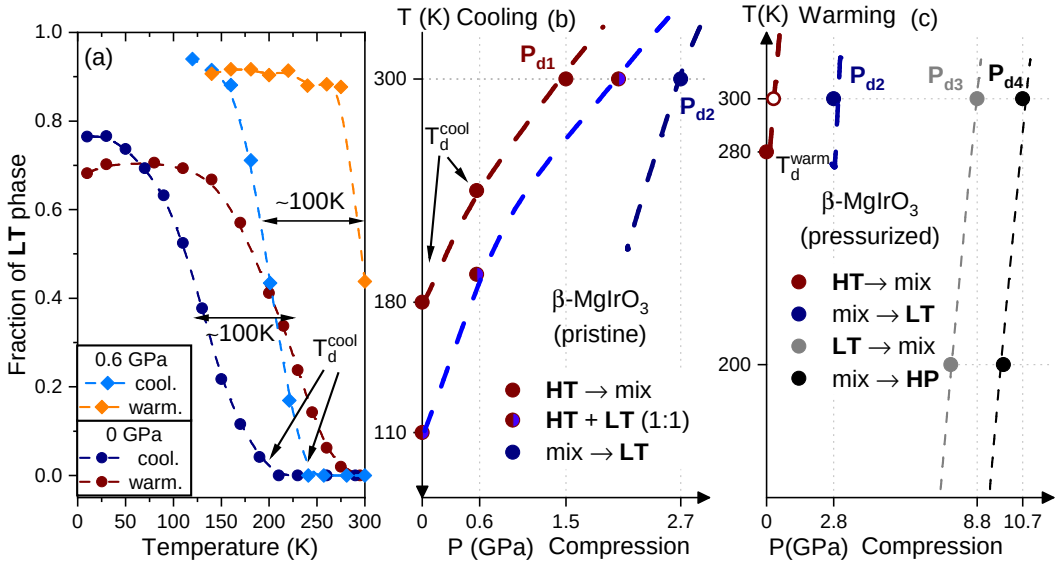

Figure 5.4: (a) Temperature dependence of the volume fraction of **LT**-$MgIrO_3$ upon cooling and warming at 0 and 0.6 GPa. The horizontal left right arrows mark the width of the thermal hysteresis at each pressure. (b) $P-T$ phase diagram of the pristine β-$MgIrO_3$ upon cooling and compression. The dashed lines represent possible boundaries of the phase transitions. The light-blue dashed line connects the spots where the ratio of the **LT** and **HT** volume fractions is equal (50% of each phase). In (a) and (b) the black arrows label the temperature of dimerization T_d^{cool} upon cooling. (c) $P-T$ phase diagram of the cooled/pressurized β-$MgIrO_3$ upon warming and compression. The data points represent the boundaries of the phase transformation from the pure phase to the mixed state and vice versa. The open symbol marks the point at 0.3 GPa in which the fraction of **HT**-phase is roughly 98%. Below this pressure, the pure nondimerized phase is suggested. The dashed lines are guides for the eye.

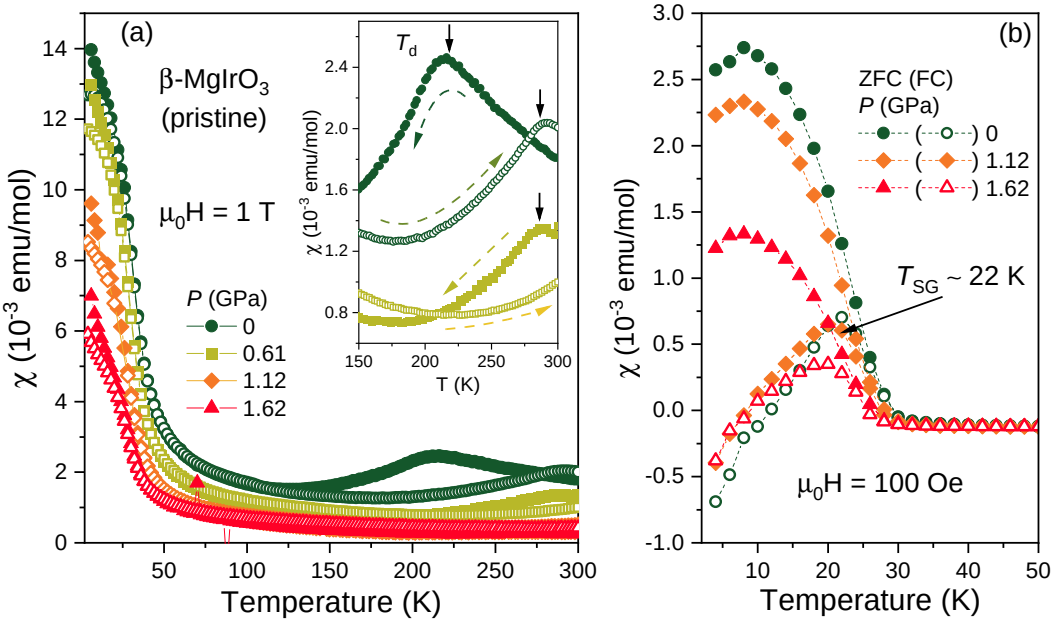

Figure 5.5: (a) Temperature-dependent magnetic susceptibility $\chi(T)$ of β-$MgIrO_3$ measured under several pressures from 4 to 300 K in the 1 T magnetic field. The closed and open symbols represent the data upon cooling and warming, respectively. The inset shows the magnifications of the steplike features due to the dimerization transition at T_d shown by the black arrows. The hysteresis loops are seen at 0 and 0.6 GPa upon cooling and warming. (b) Zero-filed-cooled (ZFC) and field-cooled (FC) DC susceptibility data measured under several pressures in the magnetic field of 100 Oe. The spin-glass transition temperature T_{SG} is indicated by the black arrow.

Now, the second case of the $P-T$ phase diagram for β-$MgIrO_3$ is considered when the sample was initially cooled/pressurized and then examined upon warming (at ambient pressure) and compression (at 100 and 300 K). Here, the region of stability of the pure **HT**-phase is drastically narrowed, and the dominant phase is the dimerized **LT**-$MgIrO_3$ which is stable between P_{d2} and P_{d3} at room temperature. At higher pressures above P_{d4}, the new **HP**-phase is formed corresponding, probably, to the subsequent dimerization of the Ir–Ir bonds. The areas of the phase mixture are also narrowed ($\sim$ 2 GPa), however, further investigation of β-$MgIrO_3$ can shed light on more precise phase boundaries at low temperatures.

5.3 Compression of β-(Li,Mg)IrO_3

In contrast to the previously described pressure-induced dimerization in the pure β-$MgIrO_3$, the study of the partially substituted β-(Li,Mg)IrO_3 under pressure was quite complicated due to the even stronger preferred orientation. This affected the accuracy of the crystal structure refinement, however, some conclusions about the dimerization transition can be made based on a qualitative analysis of the collected data.

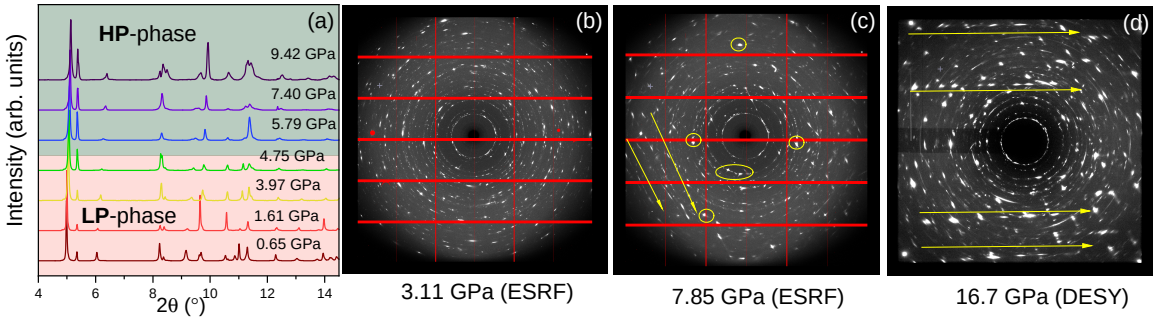

Figure 5.6: (a) Powder x-ray diffraction patterns of β-(Li,Mg)IrO_3 as a function of pressure at $T = 300$ K. 2D x-ray images of β-(Li,Mg)IrO_3 at 3.11 GPa (b) and 7.85 GPa (c) (ID15B, ESRF), and 16.7 GPa (PETRA III, DESY) (d). The effect of sample texturing and directions of single crystal diffraction are marked by yellow circles and arrows, respectively.

First of all, neither symmetry lowering nor phase coexistence were observed for β-(Li,Mg)IrO_3 upon compression up to 10 GPa. When applying pressure, the reflection position of the non-dimerized low-pressure (**LP**) phase only shifts to higher angles 2θ without new peaks appearing, indicating a gradual compression of the original unit cell to the high-pressure **HP** phase (Fig. 5.6a). However, at high pressure values, the sample appears to be strongly affected by texturing that is less pronounced at low pressure and can be seen from the comparison of two-dimensional x-ray images illustrated by Fig. 5.6b-c. The presence of a large number of individual high-intensity reflections due to the single crystal diffraction (Fig. 5.6d) doesn't allow to properly refine the crystal structure. Therefore, the collected data of β-(Li,Mg)IrO_3 were analyzed only by profile refinement, and both **LP**- and **HP**-phases were refined in the original monoclinic space group $C2/c$.

Nevertheless, the first-order phase transition from the **LP** into the **HP**-phase can be suggested by the anisotropic changes of the lattice parameters along with a small volume collapse of $\sim -1.02\%$ at the critical pressure $P_c \simeq 5.3$ GPa at $T = 300$ K (Fig. 5.7a-b). While the b and c parameters are less affected by pressure, the unit cell exhibits a noticeable contraction along the a direction around the same critical pressure value. Different behavior in the compression rates of the lattice parameters (Table 5.4) indicates the phase transformation around the same pressure of 5.3 GPa. Upon decompression, no deviation from the compression measurements in the phase boundaries and volume discontinuity were observed indicating the absence of pressure hysteresis in comparison with fully substituted β-$MgIrO_3$. Comparable values in the volume reduction of $\sim 1\%$ and anisotropic behavior of the lattice constants assume that in β-(Li,Mg)IrO_3, probably, one of the intrachain Ir–Ir bonds is dimerized above 5.3 GPa as a consequence of the structural phase transition.

Fits to the second-order Murnaghan EoS with Eq. 5.1 and Eq. 5.2 at room temperature resulted in the bulk modulus $B_{0,V}$ of 87(2) GPa for the **LP**-phase and 131(5) GPa for the **HP**-phase of β-(Li,Mg)IrO_3 (Table 5.5). A relatively

low bulk modulus of the low-pressure phase reveals a high compressibility of this structure associated also with a high value of the critical pressure $P_c \simeq 5.3$ GPa in comparison with the fully substituted β-$MgIrO_3$. Below P_c, the contribution of the a axis to the bulk modulus is the lowest, with $B_{0,a} = 35(2)$ GPa, as already indicated by the fast compression rate along this direction (Table 5.4). Thus, the material is most compressible along the a direction confirming that dimerization probably occurs along one of the intrachain Ir–Ir bonds. For the **HP**-phase, the bulk modulus $B_{0,V}$ is comparable with the dimerized **LT**-$MgIrO_3$ (152(2) GPa) and the layered α-Li_2IrO_3 (125(3) GPa) [113], however, the low bulk modulus $B_{0,b} = 81(5)$ GPa suggests the possibility of a further compression along the b direction accompanied with the second phase transition at higher pressures.

Table 5.4: Compression rates of the lattice parameters and volume for **LP**- and **HP**-phases of β-(Li,Mg)IrO_3 at $T = 300$ K (ID15B, ESRF). All values are in units of %/GPa.

Phase	$\frac{\Delta a/a_0}{\Delta P}$	$\frac{\Delta b/b_0}{\Delta P}$	$\frac{\Delta c/c_0}{\Delta P}$	$\frac{\Delta V/V_0}{\Delta P}$
LP-(Li,Mg)IrO_3	$-0.74(2)$	$-0.21(1)$	$-0.25(1)$	$-1.02(1)$
HP-(Li,Mg)IrO_3	$-0.23(2)$	$-0.32(1)$	$-0.16(1)$	$-0.64(2)$

Table 5.5: Bulk moduli $B_{0,V}$ and $B_{0,r}$, with $r = a, b, c$, in the **LP**- and **HP**-phases of β-(Li,Mg)IrO_3, as obtained from fitting the volume V and lattice parameters r with a second-order Murnaghan equation of state (EoS), with B_0' set to 4. The fits were obtained from the data collected at room temperature at ID15B (ESRF).

Phase	V_0 (Å^3/f.u.)	$B_{0,V}$ (GPa)	$B_{0,a}$ (GPa)	$B_{0,b}$ (GPa)	$B_{0,c}$ (GPa)
LP-(Li,Mg)IrO_3	57.05(4)	87(2)	35(2)	175(7)	123(4)
HP-(Li,Mg)IrO_3	55.79(10)	131(5)	111(9)	81(5)	199(25)

Additional high-pressure PXRD measurements of β-(Li,Mg)IrO_3 were performed at PETRA III (DESY) at $T = 100$ K and room temperature. The profile refinement of the collected data was still complicated due to the sample texturing/orientation (Fig. 5.6c), but the volume collapse appears at the same pressure P_c at room temperature and shifts to the low pressure of ~ 3.8 GPa at $T = 100$ K. It seems suspicious that at high pressures (above 10 GPa) there is no further volume drop like in β-$MgIrO_3$.

Magnetization measurements performed up to 2.1 GPa confirm that in this pressure range β-(Li,Mg)IrO_3 remains nondimerized, because no step-like feature is observed in the magnetic susceptibility (Fig. 5.7e).

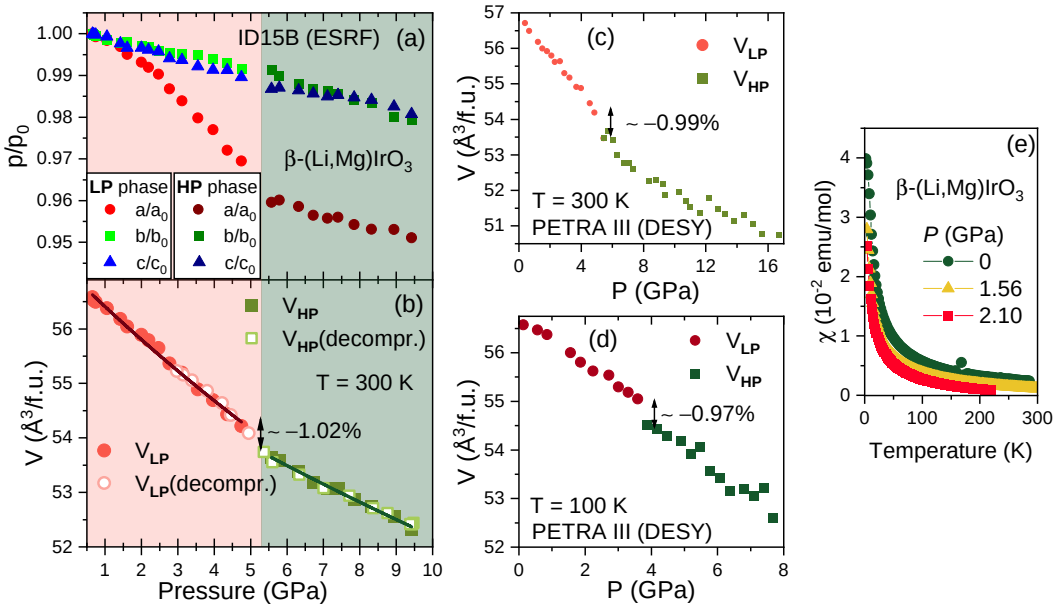

Figure 5.7: (a) Pressure dependence of the lattice parameters of β-(Li,Mg)IrO_3 at $T = 300$ K. All lattice constants are normalized to the parameters at the lowest pressure of 0.65 GPa. (b) Pressure-volume relationship of β-(Li,Mg)IrO_3 upon compression and decompression shown by closed and open symbols, respectively. The solid lines in (b) are fits with the second-order Murnaghan equation of state. Unit cell volume as function of pressure from the DESY data refinement at room temperature (c) and $T = 100$ K (d). (e) Temperature-dependent magnetic susceptibility $\chi(T)$ of β-(Li,Mg)IrO_3 measured under several pressures from 6 to 300 K in the magnetic field of 1 T. No steplike features due to the dimerization transition are observed in the presented data.

Chapter 6

Summary and Outlook

New Kitaev iridates – β-$ZnIrO_3$, β-$MgIrO_3$ and β-$Li_{2x}Mg_{1-x}IrO_3$ – have been successfully synthesized by a low-temperature topotactic ionic exchange reaction from the parent compound β-Li_2IrO_3. Structural characterization of β-$M IrO_3$ has been performed by high-resolution x-ray diffraction, neutron diffraction and electron microscopy measurements which unambiguously revealed the symmetry lowering from the orthorhombic $Fddd$ space group of β-Li_2IrO_3 to the monoclinic $P2_1/c$ and $C2/c$ groups in the case of Zn and Mg doping, respectively. The crystal structure refinement demonstrated that the hyperhoneycomb motif of edge sharing IrO_6 octahedra in the new iridates is not affected by the chemical substitution suggesting spin-$\frac{1}{2}$ behavior of Ir^{4+} ions. The symmetry lowering is caused by the presence of two distinguishable positions of the nonmagnetic elements: tetrahedral and octahedral sites of the dopant Zn^{2+} or Mg^{2+} ions. The degree of disorder in the positions of doping elements plays a significant role in magnetic properties of β-$M IrO_3$.

The long-range magnetic order observed in the parent β-Li_2IrO_3 is suppressed in the new iridates. The well-ordered β-$ZnIrO_3$ does not show any sharp anomalies in the magnetization and heat capacity data, while the AC susceptibility data exclude a conventional spin freezing below $T_a \sim 5$ K. The finite linear term of $\gamma = 10.1(3)$ mJ/mol K^2 in the specific heat suggests the presence of unconventional excitations in the ground state. The local magnetism examined by μSR study demonstrates the coexistence of static and dynamic contributions below 35 K. The ground state of β-$ZnIrO_3$ can be represented as a combination of slowly fluctuating random fields and dynamic spins up to 5.5 K. Above T_a the fraction of static spins is gradually suppressed with temperature until reaching the paramagnetic state at around 35 K.

In the fully substituted β-$MgIrO_3$, the cation disorder of Mg atoms between the tetrahedral and octahedral positions induces the structural first-order phase transition at ambient pressure at $T_d \sim 180$ K and $T_d \sim 280$ K upon cooling and warming, respectively. The transition is incomplete, characterized by a broad thermal hysteresis, and accompanied by a magnetic collapse in β-$MgIrO_3$ with the formation of the dimerized **LT**-phase and magnetic **HT**-phase. The crystal structure refinement of β-$MgIrO_3$ indicates a drastic shortening of $\frac{1}{3}$ of the Ir–Ir distances in the **LT**-phase and dimerization along the Z-bond.

The **HT**-phase exhibits a non-canonical spin-glass behavior below $T_{SG} = 22.5(1)$ K that was confirmed by DC and AC magnetization measurements.

The μSR study of β-$MgIrO_3$ revealed the absence of long-range magnetic order along with the presence of short-range correlations in the **HT**-phase. The dimerization transition was further investigated by the pressure-dependent x-ray diffraction and magnetization measurements. The full transformation from the magnetic to dimerized phase occurs at $P_{d2} \simeq 2.7$ GPa at room temperature that is the lowest pressure of dimerization transition among all known iridates [31]. The spin-glass-like behavior of the **HT**-phase was found to be robust against pressure. Upon further compression, the second phase transition into the high-pressure phase was observed at $P_{d3} \sim 8.8$ GPa. The crystal structure of the **HP**-phase was not determined, however, pressure evolution of the lattice parameters suggest the subsequent dimerization along one of the X- or Y-bonds.

The partially substituted β-$Li_{2x}Mg_{1-x}IrO_3$ exhibits the highest degree of cation disorder of nonmagnetic ions due to the mixing of Li and Mg atoms between the partially occupied tetrahedral and octahedral positions. Properties of the synthesized compounds with the different degree of Li substitution demonstrated a strong sample dependence without a clear connection to the initial composition of reactants. Only the composition with $x \simeq 0.3$ [β-(Li,Mg)IrO_3] has demonstrated reproducible results, and was used for further characterization in terms of magnetic properties. The controlled Li substitution as well as the possibility of the solid solution between β-Li_2IrO_3 and β-$MgIrO_3$ remain an open question. In contrast to the fully substituted β-$MgIrO_3$, the derivative β-(Li,Mg)IrO_3 does not undergo a phase transition as well as spontaneous dimerization upon cooling. The partially substituted magnesium iridate shows a canonical spin-glass behavior below the transition temperature $T_{SG} = 4.51(2)$ K. The analysis of AC magnetization measurements by using the critical dynamic scaling law and the Vogel-Flucher law revealed a cluster SG state in β-(Li,Mg)IrO_3. An additional investigation of the local magnetism by μSR in β-(Li,Mg)IrO_3 is planned to compare this material with other new Kitaev iridates. High-resolution x-ray diffraction under pressure revealed a volume collapse at $P_c \simeq 5.3$ GPa which is probably related to a phase transition into the dimerized state. Unfortunately, the strong sample texturing did not allow us to refine the crystal structure in detail.

This thesis work has demonstrated that chemical substitution into Ir-based materials with the hyperhoneycomb lattice can be considered as a powerful tool for finding new quantum spin-liquid candidates. Although the QSL state has not been achieved in the new Kitaev iridates β-$MIrO_3$, the magnetic order of the parent compound β-Li_2IrO_3 is suppressed, and magnetic properties of its derivatives are strongly affected by the nature of the doping elements and the degree of disorder of nonmagnetic dopants. Thus, search of new QSL materials can be performed in other perspective systems by their chemical modifications.

Bibliography

[1] L. Balents, "Spin liquids in frustrated magnets", Nature **464**, 199–208 (2010).

[2] P. Anderson, "Resonating valence bonds: A new kind of insulator?", Mater. Res. Bull. **8**, 153–160 (1973).

[3] A. Kitaev, "Anyons in an exactly solved model and beyond", Ann. Phys. **321**, 2–111 (2006).

[4] G. Khaliullin, "Orbital order and fluctuations in Mott insulators", Progress of Theoretical Physics Supplement **160**, 155–202 (2005).

[5] G. Jackeli and G. Khaliullin, "Mott Insulators in the Strong Spin-Orbit Coupling Limit: From Heisenberg to a Quantum Compass and Kitaev Models", Phys. Rev. Lett. **102**, 017205 (2009).

[6] J. Chaloupka, G. Jackeli, and G. Khaliullin, "Kitaev-Heisenberg model on a honeycomb lattice: Possible exotic phases in iridium oxides A_2IrO_3", Phys. Rev. Lett. **105**, 027204 (2010).

[7] S. Blundell, *Magnetism in condensed matter* (Oxford University Press New York, 2001).

[8] R. L. Carlin, *Magnetochemistry* (Springer Science & Business Media, 2012).

[9] N. W. Ashcroft and N. D. Mermin, *Introduction to solid state physics* (NY: Brooks Cole, 1976).

[10] G. A. Bain and J. F. Berry, "Diamagnetic corrections and Pascal's constants", J. Chem. Educ. **85**, 5919 (2008).

[11] A. Tsirlin, "Frustrated magnetism or everything you wanted to know about spin liquids but were afraid to ask", TRR80 Summer School, June, 2019.

[12] Y. Li, P. Gegenwart, and A. A. Tsirlin, "Spin liquids in geometrically perfect triangular antiferromagnets", J. Phys.: Condens. Matter **32**, 224004 (2020).

[13] S. Schmidt K. und Trebst, "Topologische Spinflüssigkeiten", Physik Journal **15** (2015).

[14] S. M. Winter, A. A. Tsirlin, M. Daghofer, J. van den Brink, Y. Singh, P. Gegenwart, and R. Valentí, "Models and materials for generalized Kitaev magnetism", Journal of Physics: Condensed Matter **29**, 493002 (2017).

[15] G. Jackeli and G. Khaliullin, "Mott insulators in the strong spin-orbit coupling limit: from Heisenberg to a Quantum compass and Kitaev models", Phys. Rev. Lett. **102**, 017205 (2009).

[16] J. G. Rau, E. K.-H. Lee, and H.-Y. Kee, "Generic spin model for the honeycomb iridates beyond the Kitaev limit", Phys. Rev. Lett. **112**, 077204 (2014).

[17]S. M. Winter, Y. Li, H. O. Jeschke, and R. Valentí, "Challenges in design of Kitaev materials: Magnetic interactions from competing energy scales", Phys. Rev. B **93**, 214431 (2016).

[18]V. M. Nishimoto Satoshi nad Katukuri, V. Yushankhai, H. Stoll, U. K. Rößler, L. Hozoi, I. Rousochatzakis, and J. van den Brink, "Strongly frustrated triangular spin lattice emerging from triplet dimer formation in honeycomb Li_2IrO_3", Nat. Commun. **7**, 10273 (2016).

[19]Y. Motome, R. Sano, S. Jang, Y. Sugita, and Y. Kato, "Materials design of Kitaev spin liquids beyond the Jackeli-Khaliullin mechanism", J. Phys.: Condens. Matter **32**, 404001 (2020).

[20]H. Liu, J. c. v. Chaloupka, and G. Khaliullin, "Kitaev spin liquid in 3d transition metal compounds", Phys. Rev. Lett. **125**, 047201 (2020).

[21]S.-H. Jang, R. Sano, Y. Kato, and Y. Motome, "Antiferromagnetic Kitaev interaction in f-electron based honeycomb magnets", Phys. Rev. B **99**, 241106 (2019).

[22]S.-H. Jang, R. Sano, Y. Kato, and Y. Motome, "Computational design of f-electron Kitaev magnets: Honeycomb and Hyperhoneycomb compounds A_2PrO_3 (A = alkali metals)", Phys. Rev. Materials **4**, 104420 (2020).

[23]L.-P. Regnault, C. Boullier, and J. Lorenzo, "Polarized-neutron investigation of magnetic ordering and spin dynamics in $BaCo_2(AsO_4)_2$ frustrated honeycomb-lattice magnet", Heliyon **4**, e00507 (2018).

[24]H. S. Nair, J. M. Brown, E. Coldren, G. Hester, M. P. Gelfand, A. Podlesnyak, Q. Huang, and K. A. Ross, "Short-range order in the quantum XXZ honeycomb lattice material $BaCo_2(PO_4)_2$", Phys. Rev. B **97**, 134409 (2018).

[25]E. M. Seibel, J. H. Roudebush, M. N. Ali, K. A. Ross, and R. J. Cava, "Structure and magnetic properties of the spin-1/2-based honeycomb $NaNi_2BiO_{6-\delta}$ and its hydrate $NaNi_2BiO_{6-\delta} \cdot 1.7\ H_2O$", Inorg. Chem. **53**, 10989–10995 (2014).

[26]R. Moessner and S. L. Sondhi, "Resonating valence bond phase in the triangular lattice quantum dimer model", Phys. Rev. Lett. **86**, 1881–1884 (2001).

[27]G. Baskaran and P. W. Anderson, "Gauge theory of high-temperature superconductors and strongly correlated Fermi systems", Phys. Rev. B **37**, 580–583 (1988).

[28]H. Takagi, T. Takayama, G. Jackeli, G. Khaliullin, and S. E. Nagler, "Concept and realization of Kitaev quantum spin liquids", Nat Rev Phys **1**, 264–280 (2019).

[29]J. R. Chamorro, T. M. McQueen, and T. T. Tran, "Chemistry of Quantum Spin Liquids", Chem. Rev. **121**, 2898–2934 (2021).

[30]L. Clark and A. H. Abdeldaim, "Quantum Spin Liquids from a Materials Perspective", Annual Review of Materials Research **51**, 495–519 (2021).

[31]A. A. Tsirlin and P. Gegenwart, "Kitaev magnetism through the prism of lithium iridate", Phys. Status Solidi B (2021).

[32]B. Schmidt, J. Sichelschmidt, K. M. Ranjith, T. Doert, and M. Baenitz, "Yb delafossites: Unique exchange frustration of $4f$ spin-1/2 moments on a perfect triangular lattice", Phys. Rev. B **103**, 214445 (2021).

[33]T. Itou, A. Oyamada, S. Maegawa, M. Tamura, and R. Kato, "Quantum spin liquid in the spin-1/2 triangular antiferromagnet $EtMe_3Sb[Pd(dmit)_2]_2$", Phys. Rev. B **77**, 104413 (2008).

[34]T. Itou, A. Oyamada, S. Maegawa, and R. Kato, "Instability of a quantum spin liquid in an organic triangular-lattice antiferromagnet", Nature Phys **6**, 673–676 (2010).

[35]P. Foury-Leylekian, V. Ilakovac, V. Balédent, P. Fertey, A. Arakcheeva, O. Milat, D. Petermann, G. Guillier, K. Miyagawa, K. Kanoda, P. Alemany, E. Canadell, S. Tomic, and J.-P. Pouget, "$(BEDT\text{-}TTF)_2Cu_2(CN)_3$ spin liquid: beyond the average structure", Crystals **8**, 158 (2018).

[36]B. Miksch, A. Pustogow, M. J. Rahim, A. A. Bardin, K. Kanoda, J. A. Schlueter, R. Hübner, M. Scheffler, and M. Dressel, "Gapped magnetic ground state in quantum spin liquid candidate κ-$(BEDT\text{-}TTF)_2Cu_2(CN)_3$", Science **372**, 276–279 (2021).

[37]H. Murayama, Y. Sato, T. Taniguchi, R. Kurihara, X. Z. Xing, W. Huang, S. Kasahara, Y. Kasahara, I. Kimchi, M. Yoshida, Y. Iwasa, Y. Mizukami, T. Shibauchi, M. Konczykowski, and Y. Matsuda, "Effect of quenched disorder on the quantum spin liquid state of the triangular-lattice antiferromagnet $1T\text{-}TaS_2$", Phys. Rev. Research **2**, 013099 (2020).

[38]R. Rawl, L. Ge, H. Agrawal, Y. Kamiya, C. R. Dela Cruz, N. P. Butch, X. F. Sun, M. Lee, E. S. Choi, J. Oitmaa, C. D. Batista, M. Mourigal, H. D. Zhou, and J. Ma, "$Ba_8CoNb_6O_{24}$: A spin-1/2 triangular-lattice Heisenberg antiferromagnet in the two-dimensional limit", Phys. Rev. B **95**, 060412 (2017).

[39]Y. Cui, J. Dai, P. Zhou, P. S. Wang, T. R. Li, W. H. Song, J. C. Wang, L. Ma, Z. Zhang, S. Y. Li, G. M. Luke, B. Normand, T. Xiang, and W. Yu, "Mermin-Wagner physics, (H, T) phase diagram, and candidate quantum spin-liquid phase in the spin-1/2 triangular-lattice antiferromagnet $Ba_8CoNb_6O_{24}$", Phys. Rev. Materials **2**, 044403 (2018).

[40]R. Zhong, S. Guo, G. Xu, Z. Xu, and R. J. Cava, "Strong quantum fluctuations in a quantum spin liquid candidate with a Co-based triangular lattice", Proc. Natl. Acad. Sci. **116**, 14505–14510 (2019).

[41]N. Li, Q. Huang, X. Y. Yue, W. J. Chu, Q. Chen, E. S. Choi, X. Zhao, H. D. Zhou, and X. Sun, "Possible itinerant excitations and quantum spin state transitions in the effective spin-1/2 triangular-lattice antiferromagnet $Na_2BaCo(PO_4)_2$", Nat. Commun. **11**, 4216 (2020).

[42]S. Lee, C. H. Lee, A. Berlie, A. D. Hillier, D. T. Adroja, R. Zhong, R. J. Cava, Z. H. Jang, and K.-Y. Choi, "Temporal and field evolution of spin excitations in the disorder-free triangular antiferromagnet $Na_2BaCo(PO_4)_2$", Phys. Rev. B **103**, 024413 (2021).

[43]Y. Li, D. Adroja, P. K. Biswas, P. J. Baker, Q. Zhang, J. Liu, A. A. Tsirlin, P. Gegenwart, and Q. Zhang, "Muon spin relaxation evidence for the U(1) quantum spin-liquid ground state in the triangular antiferromagnet $YbMgGaO_4$", Phys. Rev. Lett. **117**, 097201 (2016).

[44]Y. Shen, Y.-D. Li, H. Wo, Y. Li, S. Shen, B. Pan, Q. Wang, H. C. Walker, P. Steffens, M. Boehm, Y. Hao, D. L. Quintero-Castro, L. W. Harriger, M. D. Frontzek, L. Hao, S. Meng, Q. Zhang, G. Chen, and J. Zhao, "Evidence for a spinon fermi surface in a triangular-lattice quantum-spin-liquid candidate", Nature **540**, 559–562 (2016).

[45]Y. Li, D. Adroja, D. Voneshen, R. I. Bewley, Q. Zhang, A. A. Tsirlin, and P. Gegenwart, "Nearest-neighbour resonating valence bonds in $YbMgGaO_4$", Nat. Commun. **8**, 15814 (2017).

[46]K. M. Ranjith, D. Dmytriieva, S. Khim, J. Sichelschmidt, S. Luther, D. Ehlers, H. Yasuoka, J. Wosnitza, A. A. Tsirlin, H. Kühne, and M. Baenitz, "Field-induced instability of the quantum spin liquid ground state in the j_{eff}=1/2 triangular-lattice compound $NaYbO_2$", Phys. Rev. B **99**, 180401 (2019).

[47]K. M. Ranjith, S. Luther, T. Reimann, B. Schmidt, P. Schlender, J. Sichelschmidt, H. Yasuoka, A. M. Strydom, Y. Skourski, J. Wosnitza, H. Kühne, T. Doert, and M. Baenitz, "Anisotropic field-induced ordering in the triangular-lattice quantum spin liquid $NaYbSe_2$", Phys. Rev. B **100**, 224417 (2019).

[48]P. Mendels, F. Bert, M. A. de Vries, A. Olariu, A. Harrison, F. Duc, J. C. Trombe, J. S. Lord, A. Amato, and C. Baines, "Quantum magnetism in the paratacamite family: towards an ideal kagomé lattice", Phys. Rev. Lett. **98**, 077204 (2007).

[49]M. A. de Vries, K. V. Kamenev, W. A. Kockelmann, J. Sanchez-Benitez, and A. Harrison, "Magnetic ground state of an experimental $S = 1/2$ Kagomé antiferromagnet", Phys. Rev. Lett. **100**, 157205 (2008).

[50]T.-H. Han, J. S. Helton, S. Chu, D. G. Nocera, J. A. Rodriguez-Rivera, C. Broholm, and Y. S. Lee, "Fractionalized excitations in the spin-liquid state of a kagome-lattice antiferromagnet", Nature **492**, 406–410 (2012).

[51]J. P. Sheckelton, F. R. Foronda, L. Pan, C. Moir, R. D. McDonald, T. Lancaster, P. J. Baker, N. P. Armitage, T. Imai, S. J. Blundell, and T. M. McQueen, "Local magnetism and spin correlations in the geometrically frustrated cluster magnet $LiZn_2Mo_3O_8$", Phys. Rev. B **89**, 064407 (2014).

[52]C. Balz, B. Lake, J. Reuther, H. Luetkens, R. Schönemann, T. Herrmannsdörfer, Y. Singh, A. T. M. Nazmul Islam, E. M. Wheeler, J. Rodriguez-Rivera, T. Guidi, G. Simeoni, C. Baines, and H. Ryll, "Physical realization of a quantum spin liquid based on a complex frustration mechanism", Nature Phys. **12**, 942–949 (2016).

[53]J. Sonnenschein, C. Balz, U. Tutsch, M. Lang, H. Ryll, J. A. Rodriguez-Rivera, A. T. M. N. Islam, B. Lake, and J. Reuther, "Signatures for spinons in the quantum spin liquid candidate $Ca_{10}Cr_7O_{28}$", Phys. Rev. B **100**, 174428 (2019).

[54]Y. Singh, Y. Tokiwa, J. Dong, and P. Gegenwart, "Spin liquid close to a quantum critical point in $Na_4Ir_3O_8$", Phys. Rev. B **88**, 220413 (2013).

[55]R. Dally, T. Hogan, A. Amato, H. Luetkens, C. Baines, J. Rodriguez-Rivera, M. J. Graf, and S. D. Wilson, "Short-range correlations in the magnetic ground state of $Na_4Ir_3O_8$", Phys. Rev. Lett. **113**, 247601 (2014).

[56]A. C. Shockley, F. Bert, J.-C. Orain, Y. Okamoto, and P. Mendels, "Frozen state and spin liquid physics in $Na_4Ir_3O_8$: an NMR study", Phys. Rev. Lett. **115**, 047201 (2015).

[57]B. Koteswararao, R. Kumar, P. Khuntia, S. Bhowal, S. K. Panda, M. R. Rahman, A. V. Mahajan, I. Dasgupta, M. Baenitz, K. H. Kim, and F. C. Chou, "Magnetic properties and heat capacity of the three-dimensional frustrated $S = 1/2$ antiferromagnet $PbCuTe_2O_6$", Phys. Rev. B **90**, 035141 (2014).

[58]P. Khuntia, F. Bert, P. Mendels, B. Koteswararao, A. V. Mahajan, M. Baenitz, F. C. Chou, C. Baines, A. Amato, and Y. Furukawa, "Spin liquid state in the 3D frustrated antiferromagnet $PbCuTe_2O_6$: NMR and muon spin relaxation studies", Phys. Rev. Lett. **116**, 107203 (2016).

[59]A. Krimmel, M. Mücksch, V. Tsurkan, M. M. Koza, H. Mutka, and A. Loidl, "Vibronic and magnetic excitations in the spin-orbital liquid state of $FeSc_2S_4$", Phys. Rev. Lett. **94**, 237402 (2005).

[60]K. W. Plumb, J. R. Morey, J. A. Rodriguez-Rivera, H. Wu, A. A. Podlesnyak, T. M. McQueen, and C. L. Broholm, "Antiferromagnetic and orbital ordering on a diamond lattice near quantum criticality", Phys. Rev. X **6**, 041055 (2016).

[61]S. T. Bramwell and M. J. P. Gingras, "Spin ice state in frustrated magnetic pyrochlore materials", Science **294**, 1495–1501 (2001).

[62]L. Pauling, "The structure and entropy of ice and of other crystals with some randomness of atomic arrangement", J. Am. Chem. Soc. **57**, 2680–2684 (1935).

[63]M. Subramanian, G. Aravamudan, and G. Subba Rao, "Oxide pyrochlores – A review", Prog. Solid State Chem. **15**, 55–143 (1983).

[64]M. J. Harris, S. T. Bramwell, D. F. McMorrow, T. Zeiske, and K. W. Godfrey, "Geometrical frustration in the ferromagnetic pyrochlore $Ho_2Ti_2O_7$", Phys. Rev. Lett. **79**, 2554–2557 (1997).

[65]R. Sibille, N. Gauthier, H. Yan, M. Ciomaga Hatnean, J. Ollivier, B. Winn, U. Filges, G. Balakrishnan, M. Kenzelmann, N. Shannon, and T. Fennell, "Experimental signatures of emergent quantum electrodynamics in $Pr_2Hf_2O_7$", Nature Phys. **14**, 711–715 (2018).

[66]J. A. Mydosh, *Spin glasses: an experimental introduction* (CRC Press, 1993).

[67]J. A. Mydosh, "Spin glasses: redux: an updated experimental/materials survey", Rep. Prog. Phys. **78**, 052501 (2015).

[68]L. J. Vera Stimpson, J. M. Powell, G. B. G. Stenning, M. Jura, and D. C. Arnold, "Spin-glass behavior in $K_xRu_{4-y}Ni_yO_8$ hollandite materials", Phys. Rev. B **98**, 174429 (2018).

[69]G. A. Petrakovskii, K. S. Aleksandrov, L. N. Bezmaternikh, S. S. Aplesnin, B. Roessli, F. Semadeni, A. Amato, C. Baines, J. Bartolomé, and M. Evangelisti, "Spin-glass state in $CuGa_2O_4$", Phys. Rev. B **63**, 184425 (2001).

[70]M. A. V. Heringer, D. L. Mariano, D. C. Freitas, E. Baggio-Saitovitch, M. A. Continentino, and D. R. Sanchez, "Spin-glass behavior in $Co_3Mn_3(O_2BO_3)_2$ ludwigite with weak disorder", Phys. Rev. Materials **4**, 064412 (2020).

[71]T. Aharen, J. E. Greedan, C. A. Bridges, A. A. Aczel, J. Rodriguez, G. MacDougall, G. M. Luke, V. K. Michaelis, S. Kroeker, C. R. Wiebe, H. Zhou, and L. M. D. Cranswick, "Structure and magnetic properties of the $S = 1$ geometrically frustrated double perovskites La_2LiReO_6 and Ba_2YReO_6", Phys. Rev. B **81**, 064436 (2010).

[72]K. W. Plumb, J. P. Clancy, L. J. Sandilands, V. V. Shankar, Y. F. Hu, K. S. Burch, H.-Y. Kee, and Y.-J. Kim, "α-$RuCl_3$: a spin-orbit assisted Mott insulator on a honeycomb lattice", Phys. Rev. B **90**, 041112 (2014).

[73]J. A. Sears, M. Songvilay, K. W. Plumb, J. P. Clancy, Y. Qiu, Y. Zhao, D. Parshall, and Y.-J. Kim, "Magnetic order in α-$RuCl_3$: a honeycomb-lattice quantum magnet with strong spin-orbit coupling", Phys. Rev. B **91**, 144420 (2015).

[74]L. J. Sandilands, Y. Tian, K. W. Plumb, Y.-J. Kim, and K. S. Burch, "Scattering continuum and possible fractionalized excitations in α-$RuCl_3$", Phys. Rev. Lett. **114**, 147201 (2015).

[75]A. Banerjee, J. Yan, J. Knolle, C. A. Bridges, M. B. Stone, M. D. Lumsden, D. G. Mandrus, D. A. Tennant, R. Moessner, and S. E. Nagler, "Neutron scattering in the proximate quantum spin liquid α-$RuCl_3$", Science **356**, 1055–1059 (2017).

[76]S.-H. Do, S.-Y. Park, J. Yoshitake, J. Nasu, Y. Motome, Y. Kwon, D. T. Adroja, D. J. Voneshen, K. Kim, T.-H. Jang, J.-H. Park, K.-Y. Choi, and S. Ji, "Majorana fermions in the Kitaev quantum spin system α-$RuCl_3$", Nature Phys. **13**, 1079–1084 (2017).

[77]P. Banerjee Arnab an Lampen-Kelley, J. Knolle, C. Balz, A. A. Aczel, B. Winn, Y. Liu, D. Pajerowski, J. Yan, C. A. Bridges, A. T. Savici, B. C. Chakoumakos, M. D. Lumsden, D. A. Tennant, R. Moessner, D. G. Mandrus, and S. E. Nagler, "Excitations in the field-induced quantum spin liquid state of α-$RuCl_3$", npj Quantum Materials **3**, 8 (2018).

[78]Y. Kasahara, T. Ohnishi, Y. Mizukami, O. Tanaka, K. Ma Sixiao Sugii, N. Kurita, H. Tanaka, J. Nasu, Y. Motome, T. Shibauchi, and Y. Matsuda, "Majorana quantization and half-integer thermal quantum Hall effect in a Kitaev spin liquid", Nature **559**, 227–231 (2018).

[79]J. A. Sears, Y. Zhao, Z. Xu, J. W. Lynn, and Y.-J. Kim, "Phase diagram of α-$RuCl_3$ in an in-plane magnetic field", Phys. Rev. B **95**, 180411 (2017).

[80]R. Yadav, N. A. Bogdanov, V. M. Katukuri, S. Nishimoto, J. van den Brink, and L. Hozoi, "Kitaev exchange and field-induced quantum spin-liquid states in honeycomb α-$RuCl_3$", Sci. Rep. **6**, 37925 (2016).

[81]S.-H. Baek, S.-H. Do, K.-Y. Choi, Y. S. Kwon, A. U. B. Wolter, S. Nishimoto, J. van den Brink, and B. Büchner, "Evidence for a field-induced quantum spin liquid in α-$RuCl_3$", Phys. Rev. Lett. **119**, 037201 (2017).

[82]S. Gass, P. M. Cônsoli, V. Kocsis, L. T. Corredor, P. Lampen-Kelley, D. G. Mandrus, S. E. Nagler, L. Janssen, M. Vojta, B. Büchner, and A. U. B. Wolter, "Field-induced transitions in the Kitaev material α-$RuCl_3$ probed by thermal expansion and magnetostriction", Phys. Rev. B **101**, 245158 (2020).

[83]S. Bachus, D. A. S. Kaib, Y. Tokiwa, A. Jesche, V. Tsurkan, A. Loidl, S. M. Winter, A. A. Tsirlin, R. Valentí, and P. Gegenwart, "Thermodynamic perspective on field-induced behavior of α-$RuCl_3$", Phys. Rev. Lett. **125**, 097203 (2020).

[84]S. Bachus, D. A. S. Kaib, A. Jesche, V. Tsurkan, A. Loidl, S. M. Winter, A. A. Tsirlin, R. Valentí, and P. Gegenwart, "Angle-dependent thermodynamics of α-$RuCl_3$", Phys. Rev. B **103**, 054440 (2021).

[85]Y. Singh and P. Gegenwart, "Antiferromagnetic mott insulating state in single crystals of the honeycomb lattice material Na_2IrO_3", Phys. Rev. B **82**, 064412 (2010).

[86]F. Freund, S. C. Williams, R. D. Johnson, R. Coldea, P. Gegenwart, and A. Jesche, "Single crystal growth from separated educts and its application to lithium transition-metal oxides", Sci. Rep. **6**, 35362 (2016).

[87]S. K. Choi, R. Coldea, A. N. Kolmogorov, T. Lancaster, I. I. Mazin, S. J. Blundell, P. G. Radaelli, Y. Singh, P. Gegenwart, K. R. Choi, S.-W. Cheong, P. J. Baker, C. Stock, and J. Taylor, "Spin waves and revised crystal structure of honeycomb iridate Na_2IrO_3", Phys. Rev. Lett. **108**, 127204 (2012).

[88]F. Freund, "Synthese und physikalische Untersuchungen von Kitaev-Honigwabeniridaten", Ph.D. thesis (Universität Augsburg, 2019).

[89]S. Manni, "Synthesis and investigation of frustrated Honeycomb lattice iridates and rhodates", Ph.D. thesis (University of Göttingen, 2014).

[90]X. Liu, T. Berlijn, W.-G. Yin, W. Ku, A. Tsvelik, Y.-J. Kim, H. Gretarsson, Y. Singh, P. Gegenwart, and J. P. Hill, "Long-range magnetic ordering in Na_2IrO_3", Phys. Rev. B **83**, 220403 (2011).

[91]S. K. Choi, R. Coldea, A. N. Kolmogorov, T. Lancaster, I. I. Mazin, S. J. Blundell, P. G. Radaelli, Y. Singh, P. Gegenwart, K. R. Choi, S.-W. Cheong, P. J. Baker, C. Stock, and J. Taylor, "Spin waves and revised crystal structure of honeycomb iridate Na_2IrO_3", Phys. Rev. Lett. **108**, 127204 (2012).

[92]S. C. Williams, R. D. Johnson, F. Freund, S. Choi, A. Jesche, I. Kimchi, S. Manni, A. Bombardi, P. Manuel, P. Gegenwart, and R. Coldea, "Incommensurate counterrotating magnetic order stabilized by Kitaev interactions in the layered honeycomb α-Li_2IrO_3", Phys. Rev. B **93**, 195158 (2016).

[93]S. Choi, S. Manni, J. Singleton, C. V. Topping, T. Lancaster, S. J. Blundell, D. T. Adroja, V. Zapf, P. Gegenwart, and R. Coldea, "Spin dynamics and field-induced magnetic phase transition in the honeycomb Kitaev magnet α-Li_2IrO_3", Phys. Rev. B **99**, 054426 (2019).

[94]G. Li, L.-L. Huang, X. Chen, C. Liu, S. Pei, X. Wang, S. Wang, Y. Zhao, D. Yu, L. Wang, F. Ye, J.-W. Mei, and M. Huang, "Probing the continuum scattering and magnetic collapse in single-crystalline α-Li_2IrO_3 by Raman spectroscopy", Phys. Rev. B **101**, 174436 (2020).

[95]K. A. Modic, T. E. Smidt, I. Kimchi, N. P. Breznay, A. Biffin, S. Choi, R. D. Johnson, R. Coldea, P. Watkins-Curry, G. T. McCandless, J. Y. Chan, F. Gandara, Z. Islam, A. Vishwanath, A. Shekhter, R. D. McDonald, and J. G. Analytis, "Realization of a three-dimensional spin–anisotropic harmonic honeycomb iridate", Nat. Commun. **5**, 4203 (2014).

[96]A. Biffin, R. D. Johnson, S. Choi, F. Freund, S. Manni, A. Bombardi, P. Manuel, P. Gegenwart, and R. Coldea, "Unconventional magnetic order on the hyperhoneycomb Kitaev lattice in β-Li_2IrO_3: Full solution via magnetic resonant x-ray diffraction", Phys. Rev. B **90**, 205116 (2014).

[97]T. Takayama, A. Kato, R. Dinnebier, J. Nuss, H. Kono, L. S. I. Veiga, G. Fabbris, D. Haskel, and H. Takagi, "Hyperhoneycomb iridate β-Li_2IrO_3 as a platform for kitaev magnetism", Phys. Rev. Lett. **114**, 077202 (2015).

[98]M. Majumder, F. Freund, T. Dey, M. Prinz-Zwick, N. Büttgen, Y. Skourski, A. Jesche, A. A. Tsirlin, and P. Gegenwart, "Anisotropic temperature-field phase diagram of single crystalline β-Li_2IrO_3: Magnetization, specific heat, and ^{7}Li nmr study", Phys. Rev. Materials **3**, 074408 (2019).

[99]I. Kimchi, J. G. Analytis, and A. Vishwanath, "Three-dimensional quantum spin liquids in models of harmonic-honeycomb iridates and phase diagram in an infinite-D approximation", Phys. Rev. B **90**, 205126 (2014).

[100]A. Biffin, R. D. Johnson, I. Kimchi, R. Morris, A. Bombardi, J. G. Analytis, A. Vishwanath, and R. Coldea, "Noncoplanar and counterrotating incommensurate magnetic order stabilized by Kitaev interactions in γ-Li_2IrO_3", Phys. Rev. Lett. **113**, 197201 (2014).

[101]A. Ruiz, A. Frano, N. P. Breznay, I. Kimchi, T. Helm, I. Oswald, J. Y. Chan, R. J. Birgeneau, Z. Islam, and J. G. Analytis, "Correlated states in β-Li_2IrO_3 driven by applied magnetic fields", Nat. Commun. **8**, 961 (2017).

[102]K. A. Modic, B. J. Ramshaw, J. B. Betts, N. P. Breznay, J. G. Analytis, R. D. McDonald, and A. Shekhter, "Robust spin correlations at high magnetic fields in the harmonic honeycomb iridates", Nat. Commun. **8**, 180 (2017).

[103]A. Ruiz, V. Nagarajan, M. Vranas, G. Lopez, G. T. McCandless, I. Kimchi, J. Y. Chan, N. P. Breznay, A. Frañó, B. A. Frandsen, and J. G. Analytis, "High-temperature magnetic anomaly in the Kitaev hyperhoneycomb compound β-Li_2IrO_3", Phys. Rev. B **101**, 075112 (2020).

[104]E. K.-H. Lee, J. G. Rau, and Y. B. Kim, "Two iridates, two models, and two approaches: a comparative study on magnetism in three-dimensional honeycomb materials", Phys. Rev. B **93**, 184420 (2016).

[105]V. M. Katukuri, R. Yadav, L. Hozoi, S. Nishimoto, and J. van den Brink, "The vicinity of hyper-honeycomb β-Li_2IrO_3 to a three-dimensional Kitaev spin liquid state", Sci. Rep. **6**, 29585 (2016).

[106]M. Majumder, R. S. Manna, G. Simutis, J. C. Orain, T. Dey, F. Freund, A. Jesche, R. Khasanov, P. K. Biswas, E. Bykova, N. Dubrovinskaia, L. S. Dubrovinsky, R. Yadav, L. Hozoi, S. Nishimoto, A. A. Tsirlin, and P. Gegenwart, "Breakdown of magnetic order in the pressurized kitaev iridate β-Li_2IrO_3", Phys. Rev. Lett. **120**, 237202 (2018).

[107]M. Majumder, F. Freund, T. Dey, M. Prinz-Zwick, N. Büttgen, Y. Skourski, A. Jesche, A. A. Tsirlin, and P. Gegenwart, "Anisotropic temperature-field phase diagram of single crystalline β-Li_2IrO_3: Magnetization, specific heat, and ^7Li NMR study", Phys. Rev. Materials **3**, 074408 (2019).

[108]M. Majumder, M. Prinz-Zwick, S. Reschke, A. Zubtsovskii, T. Dey, F. Freund, N. Büttgen, A. Jesche, I. Kézsmárki, A. A. Tsirlin, and P. Gegenwart, "Field evolution of low-energy excitations in the hyperhoneycomb magnet β-Li_2IrO_3", Phys. Rev. B **101**, 214417 (2020).

[109]K. Hu, Z. Zhou, Y.-W. Wei, C.-K. Li, and J. Feng, "Bond ordering and phase transitions in Na_2IrO_3 under high pressure", Phys. Rev. B **98**, 100103 (2018).

[110]V. Hermann, J. Ebad-Allah, F. Freund, I. M. Pietsch, A. Jesche, A. A. Tsirlin, J. Deisenhofer, M. Hanfland, P. Gegenwart, and C. A. Kuntscher, "High-pressure versus isoelectronic doping effect on the honeycomb iridate Na_2IrO_3", Phys. Rev. B **96**, 195137 (2017).

[111]S. Layek, K. Mehlawat, D. Levy, E. Greenberg, M. P. Pasternak, J.-P. Itié, Y. Singh, and G. K. Rozenberg, "Electronic and structural properties of the honeycomb iridates A_2IrO_3 (A = Na, Li) at elevated pressures", Phys. Rev. B **102**, 085156 (2020).

[112]X. Xi, X. Bo, X. S. Xu, P. P. Kong, Z. Liu, X. G. Hong, C. Q. Jin, G. Cao, X. Wan, and G. L. Carr, "Honeycomb lattice Na_2IrO_3 at high pressures: A robust spin-orbit Mott insulator", Phys. Rev. B **98**, 125117 (2018).

[113]V. Hermann, M. Altmeyer, J. Ebad-Allah, F. Freund, A. Jesche, A. A. Tsirlin, M. Hanfland, P. Gegenwart, I. I. Mazin, D. I. Khomskii, R. Valentí, and C. A. Kuntscher, "Competition between spin-orbit coupling, magnetism, and dimerization in the honeycomb iridates: α-Li_2IrO_3 under pressure", Phys. Rev. B **97**, 020104 (2018).

[114]J. P. Clancy, H. Gretarsson, J. A. Sears, Y. Singh, S. Desgreniers, K. Mehlawat, S. Layek, G. K. Rozenberg, M. H. Ding Yang nad Upton, D. Casa, N. Chen, J. Im, Y. Lee, R. Yadav, L. Hozoi, D. Efremov, J. van den Brink, and Y.-J. Kim, "Pressure-driven collapse of the relativistic electronic ground state in a honeycomb iridate", npj Quantum Materials **3**, 35 (2018).

[115]V. Hermann, J. Ebad-Allah, F. Freund, A. Jesche, A. A. Tsirlin, P. Gegenwart, and C. A. Kuntscher, "Optical signature of the pressure-induced dimerization in the honeycomb iridate α-Li_2IrO_3", Phys. Rev. B **99**, 235116 (2019).

[116]T. Takayama, A. Krajewska, A. S. Gibbs, A. N. Yaresko, H. Ishii, H. Yamaoka, K. Ishii, N. Hiraoka, N. P. Funnell, C. L. Bull, and H. Takagi, "Pressure-induced collapse of the spin-orbital Mott state in the hyperhoneycomb iridate β-Li_2IrO_3", Phys. Rev. B **99**, 125127 (2019).

[117]L. S. I. Veiga, K. Glazyrin, G. Fabbris, C. D. Dashwood, J. G. Vale, H. Park, M. Etter, T. Irifune, S. Pascarelli, D. F. McMorrow, T. Takayama, H. Takagi, and D. Haskel, "Pressure-induced structural dimerization in the hyperhoneycomb iridate β-Li_2IrO_3 at low temperatures", Phys. Rev. B **100**, 064104 (2019).

[118]B. Shen, A. Jesche, M. L. Seidler, F. Freund, P. Gegenwart, and A. A. Tsirlin, "Interplay of magnetism and dimerization in the pressurized Kitaev material β-Li_2IrO_3", Phys. Rev. B **104**, 134426 (2021).

[119]A. Clearfield, "Role of ion exchange in solid-state chemistry", Chem. Rev. **88**, 125–148 (1988).

[120]A. J. Jacobson and L. F. Nazar, "Intercalation Chemistry", in *Encyclopedia of inorganic and bioinorganic chemistry* (John Wiley and Sons, Ltd, 2011).

[121]S. Manni, Y. Tokiwa, and P. Gegenwart, "Effect of nonmagnetic dilution in the honeycomb-lattice iridates Na_2IrO_3 and Li_2IrO_3", Phys. Rev. B **89**, 241102 (2014).

[122]L. Sandhya Kumari, M. Wallace, J. Barnes, B. Tong, A. Ramirez, and M. Subramanian, "Charge transfer instability in a mixed Ir/Rh honeycomb lattice in $Li_2Ir_{1-x}Rh_xO_3$ solid solution", Solid State Sciences **61**, 232–238 (2016).

[123]P. E. Pearce, C. Yang, A. Iadecola, J. Rodriguez-Carvajal, G. Rousse, R. Dedryvère, A. M. Abakumov, D. Giaume, M. Deschamps, J.-M. Tarascon, and A. Grimaud, "Revealing the reactivity of the iridium trioxide intermediate for the oxygen evolution reaction in acidic media", Chem. Mater. **31**, 5845–5855 (2019).

[124]S. Manni, S. Choi, I. I. Mazin, R. Coldea, M. Altmeyer, H. O. Jeschke, R. Valentí, and P. Gegenwart, "Effect of isoelectronic doping on the honeycomb-lattice iridate A_2IrO_3", Phys. Rev. B **89**, 245113 (2014).

[125]K. Rolfs, S. Toth, E. Pomjakushina, D. Sheptyakov, J. Taylor, and K. Conder, "Spiral magnetic phase in Li-doped Na_2IrO_3", Phys. Rev. B **91**, 180406 (2015).

[126]G. Simutis, N. Barbero, K. Rolfs, P. Leroy-Calatayud, K. Mehlawat, R. Khasanov, H. Luetkens, E. Pomjakushina, Y. Singh, H.-R. Ott, J. Mesot, A. Amato, and T. Shiroka, "Chemical and hydrostatic-pressure effects on the Kitaev honeycomb material Na_2IrO_3", Phys. Rev. B **98**, 104421 (2018).

[127]J. H. Roudebush, K. A. Ross, and R. J. Cava, "Iridium containing honeycomb delafossites by topotactic cation exchange", Dalton Trans. **45**, 8783–8789 (2016).

[128]V. Todorova, A. Leineweber, L. Kienle, V. Duppel, and M. Jansen, "On $AgRhO_2$, and the new quaternary delafossites $AgLi_{1/3}M_{2/3}O_2$, syntheses and analyses of real structures", J. Solid State Chem. **184**, 1112–1119 (2011).

[129]F. Bahrami, W. Lafargue-Dit-Hauret, O. I. Lebedev, R. Movshovich, H.-Y. Yang, D. Broido, X. Rocquefelte, and F. Tafti, "Thermodynamic evidence of proximity to a Kitaev spin liquid in $Ag_3LiIr_2O_6$", Phys. Rev. Lett. **123**, 237203 (2019).

[130]F. Bahrami, E. M. Kenney, C. Wang, A. Berlie, O. I. Lebedev, M. J. Graf, and F. Tafti, "Effect of structural disorder on the Kitaev magnet $Ag_3LiIr_2O_6$", Phys. Rev. B **103**, 094427 (2021).

[131]M. Abramchuk, C. Ozsoy-Keskinbora, J. W. Krizan, K. R. Metz, D. C. Bell, and F. Tafti, "Cu_2IrO_3: a New magnetically frustrated honeycomb iridate", J. Am. Chem. Soc. **139**, 15371–15376 (2017).

[132]E. M. Kenney, C. U. Segre, W. Lafargue-Dit-Hauret, O. I. Lebedev, M. Abramchuk, A. Berlie, S. P. Cottrell, G. Simutis, F. Bahrami, N. E. Mordvinova, G. Fabbris, J. L. McChesney, D. Haskel, X. Rocquefelte, M. J. Graf, and F. Tafti, "Coexistence of static and dynamic magnetism in the Kitaev spin liquid material Cu_2IrO_3", Phys. Rev. B **100**, 094418 (2019).

[133]Y. S. Choi, C. H. Lee, S. Lee, S. Yoon, W.-J. Lee, J. Park, A. Ali, Y. Singh, J.-C. Orain, G. Kim, J.-S. Rhyee, W.-T. Chen, F. Chou, and K.-Y. Choi, "Exotic low-energy excitations emergent in the random Kitaev magnet Cu_2IrO_3", Phys. Rev. Lett. **122**, 167202 (2019).

[134]S. Bette, T. Takayama, K. Kitagawa, R. Takano, H. Takagi, and R. E. Dinnebier, "Solution of the heavily stacking faulted crystal structure of the honeycomb iridate $H_3LiIr_2O_6$", Dalton Trans. **46**, 15216–15227 (2017).

[135]K. Kitagawa, T. Takayama, Y. Matsumoto, A. Kato, R. Takano, Y. Kishimoto, S. Bette, R. Dinnebier, G. Jackeli, and H. Takagi, "A spin–orbital-entangled quantum liquid on a honeycomb lattice", Nature **554**, 341–345 (2018).

[136]S. Pei, L.-L. Huang, G. Li, X. Chen, B. Xi, X. Wang, Y. Shi, D. Yu, C. Liu, L. Wang, F. Ye, M. Huang, and J.-W. Mei, "Magnetic Raman continuum in single-crystalline $H_3LiIr_2O_6$", Phys. Rev. B **101**, 201101 (2020).

[137]Y. Li, S. M. Winter, and R. Valentí, "Role of hydrogen in the spin-orbital-entangled quantum liquid candidate $H_3LiIr_2O_6$", Phys. Rev. Lett. **121**, 247202 (2018).

[138]Y. Haraguchi, C. Michioka, A. Matsuo, K. Kindo, H. Ueda, and K. Yoshimura, "Magnetic ordering with an XY-like anisotropy in the honeycomb lattice iridates $ZnIrO_3$ and $MgIrO_3$ synthesized via a metathesis reaction", Phys. Rev. Materials **2**, 054411 (2018).

[139]Y. Haraguchi and H. A. Katori, "Strong antiferromagnetic interaction owing to a large trigonal distortion in the spin-orbit-coupled honeycomb lattice iridate $CdIrO_3$", Phys. Rev. Materials **4**, 044401 (2020).

[140]R. D. Shannon, "Revised effective ionic radii and systematic studies of interatomic distances in halides and chalcogenides", Acta Cryst. A **32**, 751–767 (1976).

[141]W. Urland and R. Hoppe, "Zur Kenntnis der Oxoplatinate Na_2PtO_2, Na_2PtO_3, "K_2PtO_3" und "Rb_2PtO_3"", Z. anorg. allg. Chem. **392**, 23–36 (1972).

[142]K. Ohgushi, J.-i. Yamaura, H. Ohsumi, K. Sugimoto, S. Takeshita, A. Tokuda, H. Takagi, M. Takata, and T.-h. Arima, "Resonant X-ray diffraction study of the strongly spin-orbit-coupled Mott insulator $CaIrO_3$", Phys. Rev. Lett. **110**, 217212 (2013).

[143]F. Paulik, J. Paulik, M. Arnold, and R. Naumann, "Investigation on the thermal behaviour of $Mg(NO_3)_2 \cdot 6H_2O$ I. the decomposition behaviour", Journal of Thermal Analysis **34**, 627–635 (1988).

[144]V. Petříček, M. Dušek, and L. Palatinus, "Crystallographic Computing System JANA2006: General features", Zeitschrift für Kristallographie - Crystalline Materials **229**, 345–352 (2014).

[145]L Palatinus, "Pets-program for analysis of electron diffraction data", Prague, Czechia: Institute of Physics of the AS CR (2011).

[146]E. V. Akhmatskaya, R. H. Nobes, V. Milman, and B. Winkler, "Structural properties of garnets under pressure: An *ab initio* study", Zeitschrift für Kristallographie - Crystalline Materials **214**, 808–819 (1999).

[147]Y. Miura, Y. Yasui, M. Sato, N. Igawa, and K. Kakurai, "New-type phase transition of Li_2RuO_3 with honeycomb structure", J. Phys. Soc. Jpn. **76**, 033705 (2007).

[148]S. A. J. Kimber, I. I. Mazin, J. Shen, H. O. Jeschke, S. V. Streltsov, D. N. Argyriou, R. Valentí, and D. I. Khomskii, "Valence bond liquid phase in the honeycomb lattice material Li_2RuO_3", Phys. Rev. B **89**, 081408 (2014).

[149]M.-P. Jimenez-Segura, A. Ikeda, S. Yonezawa, and Y. Maeno, "Effect of disorder on the dimer transition of the honeycomb-lattice compound Li_2RuO_3", Phys. Rev. B **93**, 075133 (2016).

[150]K. Mehlawat and Y. Singh, "First-order magnetostructural transition in single crystals of the honeycomb lattice ruthenate Li_2RuO_3", Phys. Rev. B **95**, 075105 (2017).

[151]M. A. McGuire, J. Yan, P. Lampen-Kelley, A. F. May, V. R. Cooper, L. Lindsay, A. Puretzky, L. Liang, S. KC, E. Cakmak, S. Calder, and B. C. Sales, "High-temperature magnetostructural transition in van der Waals-layered α-$MoCl_3$", Phys. Rev. Materials **1**, 064001 (2017).

[152]G. Bastien, G. Garbarino, R. Yadav, F. J. Martinez-Casado, R. Beltrán Rodríguez, Q. Stahl, M. Kusch, S. P. Limandri, R. Ray, P. Lampen-Kelley, D. G. Mandrus, S. E. Nagler, M. Roslova, A. Isaeva, T. Doert, L. Hozoi, A. U. B. Wolter, B. Büchner, J. Geck, and J. van den Brink, "Pressure-induced dimerization and valence bond crystal formation in the Kitaev-Heisenberg magnet α-$RuCl_3$", Phys. Rev. B **97**, 241108 (2018).

[153]J. Hong, W. E. Gent, P. Xiao, K. Lim, D.-H. Seo, J. Wu, P. M. Csernica, C. J. Takacs, D. Nordlund, C.-J. Sun, K. H. Stone, D. Passarello, W. Yang, D. Prendergast, G. Ceder, M. F. Toney, and W. C. Chueh, "Metal–oxygen decoordination stabilizes anion redox in Li-rich oxides", Nature Mater. **18**, 256–265 (2019).

[154]A. Suter and B. Wojek, "Musrfit: a free platform-independent framework for μSR data analysis", Physics Procedia **30**, 12th International Conference on Muon Spin Rotation, Relaxation and Resonance (muSR2011), 69–73 (2012).

[155]F. Pratt, "WIMDA: a muon data analysis program for the Windows PC", Physica B: Condensed Matter **289-290**, 710–714 (2000).

[156]M. E. Fisher, "Relation between the specific heat and susceptibility of an antiferromagnet", The Philosophical Magazine: A Journal of Theoretical Experimental and Applied Physics **7**, 1731–1743 (1962).

[157]A. Yaouanc and P. D. De Reotier, *Muon spin rotation, relaxation, and resonance: applications to condensed matter*, Vol. 147 (Oxford University Press, 2011).

[158]S. J. Blundell, "Spin-polarized muons in condensed matter physics", Contemporary Physics **40**, 175–192 (1999).

[159]Y. J. Uemura, T. Yamazaki, D. R. Harshman, M. Senba, and E. J. Ansaldo, "Muon-spin relaxation in AuFe and CuMn spin glasses", Phys. Rev. B **31**, 546–563 (1985).

[160]Y. Haraguchi, A. Matsuo, K. Kindo, and H. A. Katori, "Quantum paramagnetism in the hyperhoneycomb Kitaev magnet β-$ZnIrO_3$", Phys. Rev. Materials **6**, L021401 (2022).

[161]G. Bastien, G. Garbarino, R. Yadav, F. J. Martinez-Casado, R. Beltrán Rodríguez, Q. Stahl, M. Kusch, S. P. Limandri, R. Ray, P. Lampen-Kelley, D. G. Mandrus, S. E. Nagler, M. Roslova, A. Isaeva, T. Doert, L. Hozoi, A. U. B. Wolter, B. Büchner, J. Geck, and J. van den Brink, "Pressure-induced dimerization and valence bond crystal formation in the Kitaev-Heisenberg magnet α-$RuCl_3$", Phys. Rev. B **97**, 241108 (2018).

[162]B. J. Kim, H. Ohsumi, T. Komesu, S. Sakai, T. Morita, H. Takagi, and T. Arima, "Phase-sensitive observation of a spin-orbital Mott state in Sr_2IrO_4", Science **323**, 1329–1332 (2009).

[163]R. Mathieu, A. Asamitsu, Y. Kaneko, J. P. He, and Y. Tokura, "$Eu_{0.5}Sr_{1.5}MnO_4$: A three-dimensional XY spin glass", Phys. Rev. B **72**, 014436 (2005).

[164]J. Souletie and J. L. Tholence, "Critical slowing down in spin glasses and other glasses: Fulcher versus power law", Phys. Rev. B **32**, 516–519 (1985).

[165]H Vogel, "Flűssigkeiten das temperaturabhängigkeitsgesetz der viskosität von", Phys. Zeitschr **22**, 645–646 (1921).

[166]G. S. Fulcher, "Analysis of recent measurements of the viscosity of glasses", Journal of the American Ceramic Society **8**, 339–355 (1925).

[167]C. Prescher and V. B. Prakapenka, "DIOPTAS: a program for reduction of two-dimensional X-ray diffraction data and data exploration", High Press. Res. **35**, 223–230 (2015).

[168] L. S. I. Veiga, M. Etter, K. Glazyrin, F. Sun, C. A. Escanhoela, G. Fabbris, J. R. L. Mardegan, P. S. Malavi, Y. Deng, P. P. Stavropoulos, H.-Y. Kee, W. G. Yang, M. van Veenendaal, J. S. Schilling, T. Takayama, H. Takagi, and D. Haskel, "Pressure tuning of bond-directional exchange interactions and magnetic frustration in the hyperhoneycomb iridate β-Li_2IrO_3", Phys. Rev. B **96**, 140402 (2017).

[169] F. D. Murnaghan, "The Compressibility of Media under Extreme Pressures", Proc. Natl. Acad. Sci. USA **30**, 244–247 (1944).

Appendix A

Details of crystal structure refinement

Powder neutron diffraction patterns of β-MIrO$_3$ are presented in Fig. A.1.

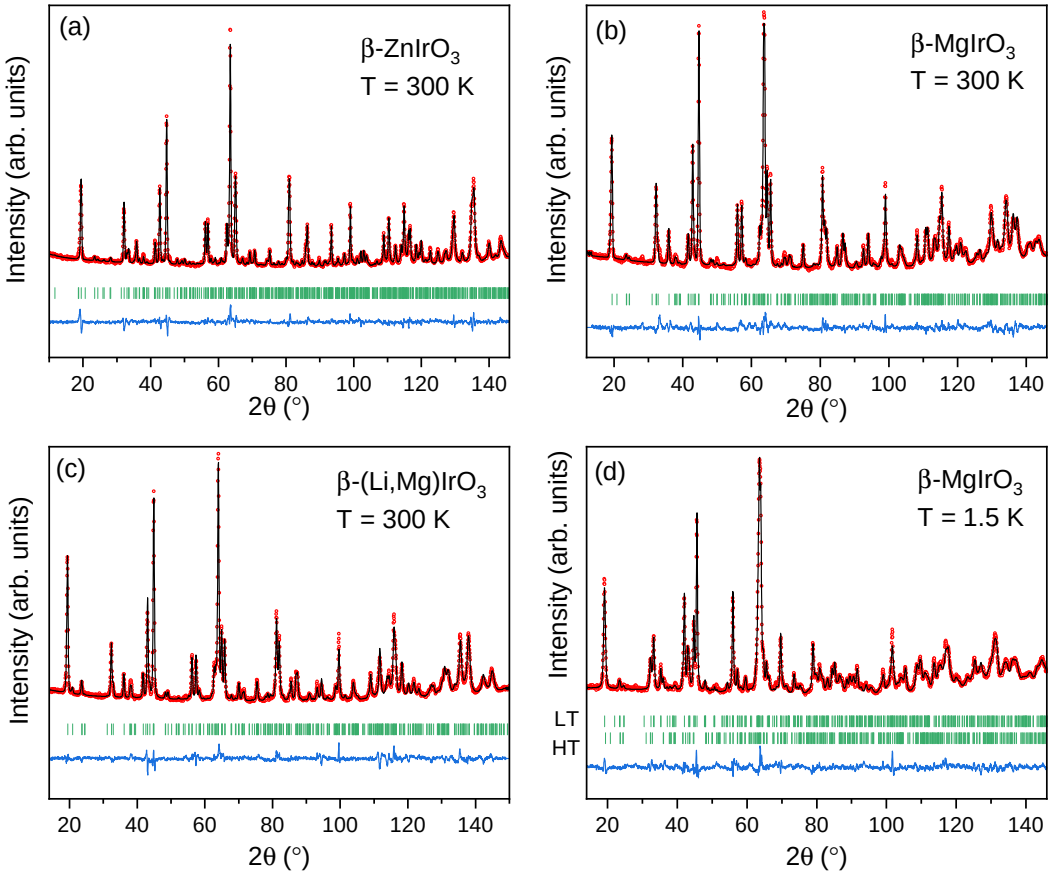

Figure A.1: Rietveld refinements versus neutron diffraction data of β-ZnIrO$_3$ (a), β-MgIrO$_3$ (b), β-(Li,Mg)IrO$_3$ (c) at room temperature as well as β-MgIrO$_3$ (d) at $T = 1.5$ K. Experimental data are shown by red points, calculated patterns – by black lines. Positions of peaks and the difference plot are shown in the bottom part by green ticks and the blue line, respectively.

Data collection and refinement details are shown in Tables A.1 and A.2. The refined parameters of atomic positions are presented in Tables A.3, A.4 and A.5 obtained from the Rietveld refinement of the neutron diffraction data

at $T = 1.5$ K. g denotes site occupancy. In the case of β-$ZnIrO_3$, the g values are 1 for all atoms. The isotropic displacement parameter U_{iso} was fixed during the refinement for all atoms at 0.001 Å^2.

Table A.1: Data collection and refinement details for the β-MIrO$_3$ compounds against the neutron diffraction data ($\lambda = 1.594$ Å) collected at room temperature.

Parameters	β-$ZnIrO_3$	β-$MgIrO_3$	β-(Li,Mg)IrO_3
space group	$P2_1/c$	$C2/c$	$C2/c$
a (Å)	8.76368(17)	8.7238(2)	8.6880(3)
b	5.92098(11)	5.97367(13)	5.94142(16)
c	9.9227(3)	9.8320(2)	9.8104(4)
β (deg)	116.125(3)	115.993(2)	116.20(1)
V (Å^3)	462.28(2)	460.55(2)	454.38(3)
Z	8	8	8
ρ (g cm^{-3})	8.78	7.63	7.00
μ (mm^{-1})	0.654	0.655	0.774
2θ range (deg)	10.05-146.8	13.5-155.7	13.9-148-9
No. of ref. param.	51	38	38
R_p	0.0367	0.0343	0.0356
R_{wp}	0.0486	0.0456	0.0472
goodness-of-fit	2.09	2.25	2.10
residual density (e Å^{-3})	0.97/-0.96	0.91/-0.95	0.98/-0.82

Table A.2: Data collection and refinement details for the β-MIrO$_3$ compounds against the neutron diffraction data ($\lambda = 1.594$ Å) collected at $T = 1.5$ K.

Parameters	β-ZnIrO$_3$	**HT**-MgIrO$_3$	**LT**-MgIrO$_3$
space group	$P2_1/c$	$C2/c$	$C2/c$
a (Å)	8.7492(2)	8.7104(9)	8.8955(5)
b	5.91635(12)	5.9627(5)	6.0790(3)
c	9.9190(3)	9.8322(10)	9.4563(6)
β (deg)	116.083(2)	115.985(7)	117.597(4)
V (Å^3)	461.15(2)	459.03(8)	453.18(5)
Z	8	8	8
ρ (g cm^{-3})	8.80	7.66	7.75
μ (mm^{-1})	0.655	0.657	0.665
2θ range (deg)	10.05-146.8	14.3-146.6	14.3-146.6
No. of ref. param.	50	54	54
R_p	0.0401	0.0348	0.0348
R_{wp}	0.0520	0.0446	0.0446
goodness-of-fit	2.20	2.25	2.25
residual density (e Å^{-3})	0.97/-0.96	0.84/-0.66	0.50/-0.48

Table A.3: Atomic coordinates for the crystal structure of β-ZnIrO$_3$.

Atom	Site	x	y	z
Ir1	4e	0.3277(13)	0.123(3)	0.4182(8)
Ir2	4e	0.1586(13)	0.126(3)	0.0820(8)
Zn1	4e	0.5108(17)	0.380(4)	0.2774(9)
Zn2	4e	0.1235(12)	0.623(4)	0.2506(16)
O1	4e	0.0738(18)	0.614(4)	0.4238(15)
O2	4e	0.1038(19)	0.129(4)	0.4285(14)
O3	4e	0.3991(19)	0.151(3)	0.0925(12)
O4	4e	0.5587(19)	0.114(4)	0.4194(15)
O5	4e	0.7452(16)	0.393(5)	0.2558(15)
O6	4e	0.2546(16)	0.354(5)	0.2533(14)

Table A.4: Atomic coordinates and displacement parameters for the crystal structure of the **HT**-phase of β-$MgIrO_3$

Atom	Site	x	y	z	g
Ir	$8f$	0.9086(18)	0.868(3)	0.0772(12)	1
Mg1	$8f$	0.754(6)	0.136(14)	0.239(4)	0.407(19)
Mg2	$8f$	0.632(3)	0.852(4)	0.242(3)	0.593(19)
O1	$4e$	0	0.637(6)	0.25	1
O2	$4e$	0.5	0.582(6)	0.25	
O3	$8f$	0.691(3)	0.886(4)	0.081(2)	
O4	$8f$	0.657(2)	0.387(3)	0.091(2)	

Table A.5: Atomic coordinates and displacement parameters for the crystal structure of the **LT**-phase of β-$MgIrO_3$

Atom	Site	x	y	z	g
Ir	$8f$	0.9203(7)	0.8701(11)	0.0903(4)	1
Mg1	$8f$	0.739(2)	0.129(4)	0.2206(12)	0.516(8)
Mg2	$8f$	0.624(2)	0.867(4)	0.251(3)	0.484(8)
O1	$4e$	0	0.616(2)	0.25	1
O2	$4e$	0.5	0.612(2)	0.25	
O3	$8f$	0.6878(11)	0.8446(15)	0.0824(7)	
O4	$8f$	0.6418(11)	0.3953(16)	0.0768(9)	